Data-Driven Model Identification for hyperelasticity : mapping the strain energy throughout multiaxial experiments

Léna Costecalde

COLLEGE DOCTORAL PAYS DE LA LOIRE — SCIENCES DE L'INGENIERIE ET DES SYSTEMES

CENTRALE NANTES

MEMOIRE DE DOCTORAT DE

L'ECOLE CENTRALE DE NANTES

ECOLE DOCTORALE N° 602
Sciences de l'Ingénierie et des Systèmes
Spécialité : *Mécanique des Solides, des Matériaux, des Structures et des Surfaces*

Par
Léna COSTECALDE

Data-Driven Model Identification for hyperelasticity: mapping the strain energy throughout multiaxial experiments.

Projet de recherche doctoral présenté et soutenu à l'École Centrale de Nantes, le 21 décembre 2023
Unité de recherche : UMR 6183, Institut de Recherche en Génie Civil et Mécanique (GeM)

Rapporteurs avant soutenance :

Jean-Benoit LE CAM	Professeur des universités, Université de Rennes
Benoit BLAYSAT	Professeur des universités, Université Clermont Auvergne

Composition du Jury :

Présidente :	Carole NADOT-MARTIN	Professeure des universités, ISAE-ENSMA Poitiers
Examinateurs :	Jean-Benoit LE CAM	Professeur des universités, Université de Rennes
	Benoit BLAYSAT	Professeur des universités, Université Clermont Auvergne
	Auriane PLATZER	Maîtresse de conférences, INSA Lyon
Directeur de recherches doctorales :	Erwan VERRON	Professeur des Universités, Ecole Centrale de Nantes
Co-dir. de recherches doctorales :	Michel CORET	Professeur des Universités, Ecole Centrale de Nantes
Co-enc.de recherches doctorales :	Adrien LEYGUE	Chargé de recherche, CNRS, Ecole Centrale de Nantes

Invité
Antoine PERRIOT — Dr, Ingénieur de recherche, MICHELIN Cébazat

Remerciements

Tout d'abord, je tenais à remercier tout particulièrement les deux rapporteurs de cette thèse, Jean-Benoît Le Cam et Benoît Blaysat. Merci infiniment pour votre temps, mais aussi vos remarques et questions qui ont apporté un éclairage nouveau sur mes travaux. Je remercie également Carole Nadot-Martin d'avoir accepté de présider mon jury de thèse et également Antoine Perriot et Auriane Platzer d'avoir accepté d'en faire partie. Un grand merci à tous les membres du jury pour votre expertise, vos commentaires, vos questions et votre bienveillance, qui m'ont permis de prendre toujours un peu plus de recul sur mes travaux, leur richesse, leur complexité et leurs perspectives. Je garderai d'excellents souvenirs de nos échanges et de leur richesse, et je vous en remercie. J'adresse un merci particulier à Antoine Perriot, qui a oeuvré chez Michelin pour nous fournir un matériau sur lequel travailler, et qui a suivi avec intérêt et curiosité mes travaux tout au long de ces années.

Cette thèse n'aurait pas pu être ce qu'elle est sans l'implication, la curiosité et la pédagogie de mes trois encadrants de thèse, que je remercie grandement. Adrien Leygue, tout d'abord, est une source d'idées intarissable, qui permet qu'un problème n'en reste pas un bien longtemps, si tant est que la solution soit codable d'une manière ou d'un autre. J'ai apprécié nos discussions sur des coins de tableau, et ton soutien tout au long de cette thèse, qui malheureusement n'était pas assez longue pour voir aboutir toutes tes belles idées. Michel Coret, ensuite, est l'élément indispensable d'une campagne expérimentale réussie. Sa patience, sa curiosité et sa pédagogie transforment presque les sessions expérimentales en jeux d'enfants. Il est également celui qui sait remettre les pieds sur terre à toute l'équipe, en faisant un lien adéquat avec le pendant expérimental des travaux. J'ai adoré nos sessions hexapode au CRED, mais aussi nos discussions vélo autour d'un café. Erwan Verron, enfin, est celui qui a le don, sinon l'expérience, de la gestion du timing. Sa grande connaissance et son infinie pédagogie font que n'importe quelle question théorique ne reste sans réponse, ou au moins sans biblio. Ses qualités d'encadrant (et d'enseignant) restent encore à dénombrer tant il y en a. Je te remercie particulièrement pour tout mon parcours, de l'intérêt suscité pour les matériaux en école d'ingénieurs, jusqu'à mon potentiel futur. Merci encore pour toutes ces discussions riches, autour de la science et du reste, ça a été un immense plaisir de travailler avec vous.

Au sein du laboratoire et au cours de le thèse, j'ai eu la chance de travailler avec de nombreux enseignant · es-chercheureuses, que je tiens à remercier. La lecture de vos travaux et le récit de vos parcours ont participé grandement à mon envie de poursuivre dans l'académique. Dans un premier temps, je remercie particulièrement Bertrand Huneau et Jean-Charles Passieux, pour leur constribution aux CSI, leurs remarques pertinentes et leurs conseils éclairés pour la poursuite de la thèse. Je remercie également tous les membres du groupe de travail Outlaw, pour les discussions scientifiques riches et les moments partagés. L'UTR Melani a été pour moi un lieu d'émulation scientifique et d'échanges, dont je remercie tous les membres et en particulier Julien Réthoré et Mathilde Chevreuil pour l'animation de l'équipe et leur bienveillance et considération pour les thésards, qui

contribuent à notre épanouissement dans ce projet de recherche.

J'adresse des remerciements chaleureux aux collègues avec qui j'ai pu faire équipe au sein du département d'enseignement Mécanique des Matériaux et Génie Civil, notamment Sébastien Comas, Guillaume Racineux, Thomas Corre, et toutes celles et ceux avec qui j'ai pu encadrer des TP. Je remercie également les élu · es du Conseil des Etudes, pour nos combats et nos échanges qui rythmaient les conseils tout au long de l'année. J'adresse une pensée particulière à Benjamin, Amélie et les élu · es étudiant · es.

Ensuite, j'adresse mes plus profonds remerciements à mes 3 merveilleux colocataires, qui m'ont supportée et soutenue tout au long de la thèse. Awen tout d'abord, avec de judicieuses pauses sportives pendant les confinements et couvre-feux, Louise ensuite, avec des ateliers créatifs et un retour à cheval, et enfin Léo, celui des trois qui me supporte le plus : merci pour tout. Merci à toutes les personnes avec qui j'ai eu la chance de partager un bureau, au bâtiment T ou O, mais aussi de nombreuses pauses café, car la science ne serait pas ce qu'elle est sans ce partage et ces discussions informelles. Un merci tout particulier à Héloïse, ma soeur de thèse, avec qui j'ai partagé deux bureaux, des conférences et une école d'été. Merci enfin à la team footing, la team badminton, la team vélo et la team squash pour toutes ces heures de sport qui me faisaient relativiser n'importe quel obstacle rencontré en recherche.

Enfin, je remercie mes parents de m'avoir soutenue dans cette aventure, depuis ma première journée d'école jusqu'à ma soutenance de thèse. Je leur dois le goût pour les études, mais aussi la curiosité scientifique et le sport ! Merci à ma famille, mes amis et toutes celles et ceux qui ont participé à ce que cette soutenance soit une merveilleuse journée.

Note: While this manuscript is written in english language, I decided to write the acknoledgements using my mother tongue, to make them accessible to my non-english speaker friends and family.

Contents

List of Figures

List of Tables

Introduction

Introduction

Materials are surrounding us and mankind needed no time to understand that materials had different properties and different responses under loading. Yet, as we delve deeper into the world of materials, we encounter several intriguing puzzles-among them, the mechanical behaviour of large strain elastic materials, such as rubber. Understanding and predicting how these materials respond to external forces, and how they deform, is a cornerstone of mechanical engineering. It underpins the development of products ranging from shock-absorbing tires to medical devices. However, this is precisely where modern material science faces intricate and compelling challenges. Mechanical engineering proposes tools to model and describe those different material behaviours. Numerous constitutive laws, relating at least a strain measure to a stress measure, were developed for each type of material. We can refer particular formulation of a constitutive law as a model, which also relates strain and stress to different parameters. Models are built to smooth out experimental noise, shorten experimental campaigns by reducing the number of needed experiments and offer prediction abilities to anticipate material behaviour in service.

In this context, identification, the procedure of adapting a model to a material behaviour emerged. Three steps are classically mandatory to identify material behaviour.

- First, a series of experiments is run. The experiments are chosen and carefully run to generate homogeneous strain and stress fields. This property ensures that the stress field is computable through displacements and net force measures.
- Second, the strain field, stress field, and additional features are calculated.
- Third, a model is chosen and a minimisation procedure is run to find the model parameters which will minimise the error between the model-calculated stress field and the experimentally-measured one. A least-squares minimisation procedure is often considered, with a gradient descent procedure.

Models can be built using microscopic observations, such as macromolecular models for elastomers, or be based on macroscopic observations, such as phenomenological models. They can also combine these two characteristics, and have different forms. New models are developed yearly to precisely describe the mechanical behaviour of new materials or encompass additional phenomena. This research endeavour plunges headfirst into the depths of modern material science, aiming to unravel the enigma of identifying the mechanical response of hyperelastic materials, with rubber as a prominent example. Part 1 of the present thesis is dedicated to the definition of identification and the presentation of different existing methods within the first chapter, as well as the presentation of the tools and materials which are used in this manuscript. The objectives of the thesis are presented in the second chapter. This first part focuses on the study of hyperelastic materials, which will be used throughout the manuscript.

Identification is a term that can be used in different manners. Instead of meaning "the adaptation of model parameters to an experimental dataset", identification can be used to describe "a method that identifies the mechanical response of a material through the estimation of its stress response". The mechanical response of a material consists of related features, including at least a strain field and a corresponding stress field, to which can be added temporal, energetic or thermal features which characterise the material behaviour. Identifying the mechanical response of a given material is then finding related features which describe this response. That is the goal of the Data-Driven Identification method [57]. This method falls within the Data-Driven paradigm introduced by Kirchdoerfer and Ortiz in 2016 [50]. It consists in representing the material response with a discrete point cloud instead of a continuous manifold. This paradigm was first introduced to propose a model-independent method for computational mechanics: Data-Driven Computational Mechanics (DDCM). DDI is an extension of DDCM built to estimate the stress response of a material using the corresponding strain field and net forces for complex experiments but without any use of a model. The method provides a balanced stress field suitable for further applications. The DDI method is applied to hyperelastic materials in this work.

Considering the existing diversity of methods to identify, model and predict material behaviour, the present work addresses the following questions:

- How can we explore the diversity and benefits of non-homogeneous experimental tests for identification?
- And, in this context, can Data-Driven methods collaborate with traditional modelling to gather benefits from both approaches?

To address these questions, we propose to explore the mechanical response of hyperelastic planar membranes, from the design of multiaxial tests and corresponding samples, to the computation of the full mechanical response of a material, and through the development of a new identification method.

First of all, we propose to develop multiaxial tests using an innovative experimental setup with a hexapod device. The six degrees of freedom of the device allow one to explore a whole new range of loading conditions, with prescribed displacements and rotations. A planar SBR sample pierced with six holes is used for experimental purposes. The experiments and datasets are presented in Chapter 3. The resulting datasets are available on a public repository. Then, the exploration of the kinematic response of materials during multiaxial tests led to the construction of a "kinematic map". The goal of this map is to compare multiaxial tests and observe their quality in terms of deformation diversity, considering both mode and magnitude. It is presented in Chapter 4. This map is then enriched to explore the materials' full mechanical response, including kinematics and stress response, in Chapter 5. The final "mechanical response map" is presented at the end of the chapter. It encompasses the kinematic map and the stress response of the material. These results are presented in Part 2.

Finally, the third and last part of the manuscript presents the direct application of previously developed methods and tools. Chapter 6 proposes an innovative identification method centred on a multiaxial test using both Data-Driven and modelling approaches. This method presents the benefits of both full-field measurement-based methods and the fitting ease of the classical method. It is investigated thanks to both synthetic and experimental data. The "mechanical response map" is used to compare the fitted models with experimental data. Finally, Chapter 7 proposes answers to the question of a good

identification test by comparing sample designs. The "kinematic map" is used to compare the designs and choose the better identification-suited one. Both applications are developed in Part 3.

We invite you to embark on this intellectual journey through the intricacies of the mechanics of materials, with a particular focus on deciphering the mechanical response of large-strain elastic materials. Together, we aim to bring a better understanding of identification methods applied to hyperelastic materials and the development of enriched multiaxial tests designed for identification.

Part I

General context and study framework

Chapter 1

Overview of identification techniques

With mechanical engineering emerged the need to model the mechanical response of materials. This modelling allows engineers to design industrial parts, understand, reproduce and predict their behaviour. Models, or constitutive equations or laws, are the key tool to model the mechanical response of the material. They are equations relating at least one strain measure to a stress measure, and they involve one or several parameters. Plenty of constitutive laws exist, they are adapted to a material type or property, for a given strain range.

Some good practices for the use of constitutive laws are highlighted in this chapter. Identification or "the art" of adapting a constitutive model to the experimental response of a given material is explored hereafter. The standard method, based on simple deformation states experiments, allows to adapt model parameters on the stress field. A simple deformation state experiment allows to calculate the complete corresponding stress tensors. Full-field measurement-based identification methods have recently emerged, thanks to Digital Image Correlation, allowing identification on a single multiaxial experiment. Finite Element Model Updating (FEMU) method is detailed as an example of a full-field measurement-based identification method.

The fitting of models to material response, called "identification" can be done with different methods. Full-field measurement-based methods provide identification on a large range of deformation modes, whereas the classical identification method allow for the model choice to take place at the very end of the procedure. These major advantages could be coupled into a new identification method.

Contents

Each material is unique in its constitution and behaviour, and those two characteristics largely influence the type of industrial applications it can serve. Differences between materials can be witnessed by simple observation, but tools and models had to be developed to characterise each unique behaviour precisely. For industrial applications and everyday use, we need to anticipate and predict material response under loading, for the sake of safety or simply the design of industrial parts. From empirical observations of material behaviour to its representation in mechanical problems, the present section investigates material modelling in mechanical problems.

1.1 Modelling mechanical response of materials

There is evidence of observations of material behaviour since humans began to use tools. During the Paleolithic period, shaped rocks were observed as possessing properties that human hands had not [77]. Comparisons between materials were conducted too, as seen with the development of rocky arrow ends instead of wooden ones. New use and tools have been developed after discovering new material exhibiting specific properties. For example, it was witnessed after the Europeans set foot in America in the fifteenth century and saw indigenous people playing with latex balls, which was completely unknown in Europe [67].

Contemporary researchers have carried on this observational work, and material properties have been conceptualised since. Sticking with the general range of elastomers, we can cite the Payne effect [75] and Mullins effect [70], two material properties of carbon black-filled rubbers conceptualised in 1962 and 1969 respectively.

1.1.1 Why modelling the mechanical response of materials ?

The use of materials along with physics and mathematics development led to a more systematic need to characterise, quantify and analyze material behaviour. The industrial revolution in the nineteenth century is characterised by an acceleration of production and uniform products. Thus, before launching a new manufacturing line, engineers need to conceive products and accurately predict their behaviour on the manufacturing line as well as during their use in service. Objects and industrial parts are subjected to various loading conditions, either prescribed displacements or applied forces or moments, that will constitute boundary conditions of the corresponding mechanical problem, which solution is necessary to predict the behaviour of the part.

Mechanics aims at describing and understanding the relations between matter, forces, and motions in solid bodies or fluids. It can be divided into three fields: classical mechanics, quantum mechanics and relativistic mechanics. The size of an object of study and its speed range delimiter the domain of validity of each mechanics field. This work's major object of study is solid bodies larger than 10^{-9} m at a speed far less than light celerity, entering the spectrum of classical mechanics. Those bodies are considered as a continuum of matter, at a mesoscopic level, meaning that they can be divided into infinitesimal elements exhibiting no difference in mechanical properties with the whole body. Continuum Mechanics relies on the Representative Elementary Volume, which is the smallest volume over which a measurement can be made that will yield a value representative of the whole. Continuum Mechanics is a tool to explain and understand various physical phenomena without detailing these phenomena at a microscopic scale [63]. Kinematics is a field of classical mechanics attached to the description of the motion of points, bodies or systems. Continuum mechanics uses a large range of mathematical tools, including tensors, which

are noted in bold characters in this manuscript, and vectors, noted with an arrow on top.

Kinematical features in Continuum mechanics

In Continuum Mechanics, the kinematics of a transformation is described using various features. Two descriptions can be considered:

- the Lagrangian description, also called "material description" which consists in observing the material particles and their motion in space, with regards to the reference configuration of the object,
- and the Eulerian description, also called "spatial description", which consists in observing the evolution of physical quantities, from a fixed point of view.

Figure 1.1 summarises the principal kinematical features for Continuum mechanics.

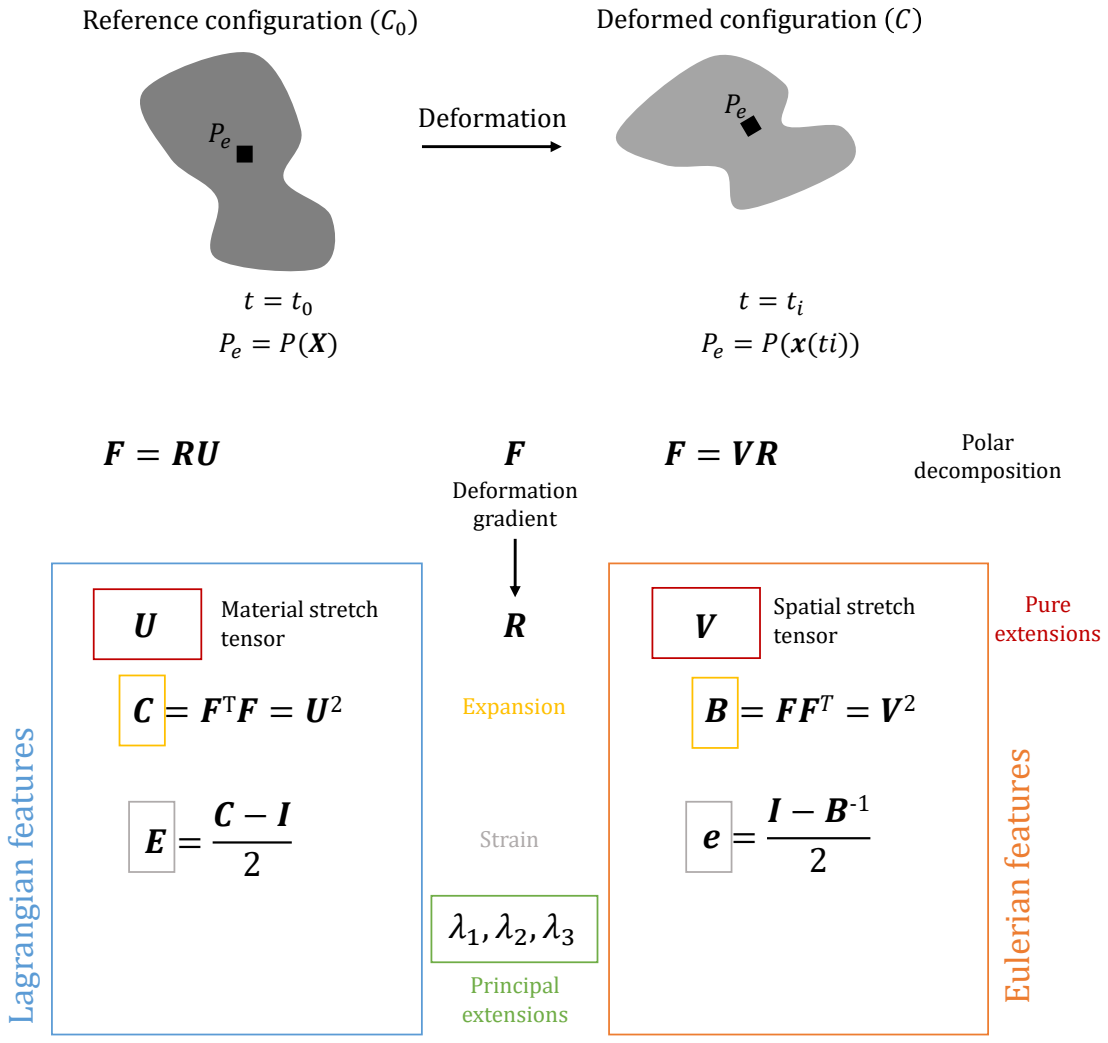

Figure 1.1: Principal kinematical features in Continuum Mechanics. The features are presented from displacements to strain, for both Lagrangian (left) and Eulerian (right) descriptions.

On the top part of the figure, two configurations of an object are represented: the reference configuration ($\mathcal{C}_0$) on the left, corresponding to the start of the observation

($t = t_0$), and the current or deformed configuration ($\mathcal{C}$) at time $t = t_i$, with $t_i > t_0$. A transformation takes place, and the object transforms from reference configuration to current configuration. During the transformation, the material point P_e, represented by the black square on the body in Figure 1.1, changes of position: it was first described by its reference location, using the material vector $\boldsymbol{X}$, and is now represented by the current spatial vector $\boldsymbol{x}(t_i)$.

The displacement $\boldsymbol{u}$ of the point is described using the reference configuration and current configuration position, with $\boldsymbol{u}(\boldsymbol{X}, t_i) = \boldsymbol{x}(\boldsymbol{X}, t_i) - \boldsymbol{X}$. The deformation gradient $\boldsymbol{F}$ can be calculated from the transformation mapping such as:

$$\boldsymbol{F} = \frac{\partial \boldsymbol{x}}{\partial \boldsymbol{X}}, \tag{1.1}$$

then pure extension tensors $\boldsymbol{U}$ and $\boldsymbol{V}$, and rotation tensor $\boldsymbol{R}$ are calculated using the polar decomposition of $\boldsymbol{F}$. Their relation and expressions are displayed in Figure 1.1.

Left and right Cauchy-Green deformation tensors $\boldsymbol{B}$ and $\boldsymbol{C}$ are calculated using the deformation gradient $\boldsymbol{F}$ and its transpose. They express the change in shape and size of the material particle. Green-Lagrange and Euler-Almansi strain tensors $\boldsymbol{E}$ and $\boldsymbol{e}$ are then expressed, $\boldsymbol{I}$ being the identity tensor. The eigenvalues of $\boldsymbol{B}$ and $\boldsymbol{C}$ are the principal stretches $\lambda_1, \lambda_2, \lambda_3$. Additional explanations on kinematics can be found in [45].

Definition of a mechanical problem
Solving a mechanical problem consists in finding the tuple $(\boldsymbol{u}, \boldsymbol{\epsilon}, \boldsymbol{\sigma})$ such as:

- the stress field $\boldsymbol{\sigma}$ is statically admissible, that is to say, it is balanced at each point of the continuous body and respects the imposed stress or force conditions on the boundary,
- the displacement field $\boldsymbol{u}$ is kinematically admissible, that is to say, it is continuous and differentiable at each point of the domain and respects the imposed displacements boundary conditions,
- the strain field $\boldsymbol{\epsilon}$ cen be derived from the transformation mapping,
- the strain and stress fields are compatible in the sense of a certain relationship, referred to as a constitutive law.

The geometry and boundary conditions of the studied body are the basic inputs of the problem. Once the kinematics and the equilibrium of the structure have been considered, the resolution relies on a missing link yet to define and study: the constitutive law.

1.1.2 Models and constitutive laws

A **constitutive law** is an explicit relation between at least the deformation measure and stress measure. Constitutive laws express the physical characteristics of a material: incompressibility, linearity, isotropy, *etc.* For example, linear elastic materials are materials that exhibit an instantaneous and reversible response to an applied strain, and for which the applied strain is proportional to the stress. Those materials can be represented by a simple linear spring in unidimensional representations. For isotropic linear elastic materials, Hooke's law relates infinitesimal deformations $\boldsymbol{\epsilon}$ and stress $\boldsymbol{\sigma}$ as follows :

$$\boldsymbol{\sigma} = \mathbb{C} : \boldsymbol{\epsilon}, \tag{1.2}$$

with $\boldsymbol{\sigma}$ the stress tensor (Pa), $\boldsymbol{\epsilon}$ the strain tensor and $\mathbb{C}$ the fourth order stiffness tensor (Pa). Constitutive laws respect some conditions such as physical principle (particularly thermodynamic ones), objectivity, determinism, which means that current quantities and variables at time t depend on variables and quantities at previous times, and locality, which means that the constitutive variables at material point $\mathbf{M}$ depend on variables and quantities defined or measured in its close neighbourhood. Once ensuring those requirements, the constitutive law is characterised by:

- its name, in our example Hooke's law,
- its equation, in our example Eq. (1.2),
- its parameters, in our example the components of $\mathbb{C}$,
- and its validity domain, that is to say, the range of deformation the constitutive law is valid on, in our example the strain range in which the material is elastic.

Isotropic linear elastic materials are fully constrained by their physical properties, and follow a unique constitutive law. Other types of material are not fully constrained by their physical properties. Their constitutive law itself is insufficient to completely describe their behaviour.

Constitutive law for isotropic hyperelastic materials is given by Eq. (1.3).

$$\boldsymbol{\sigma} = 2I_3^{-1/2}\left[\left(I_2\frac{\partial W}{\partial I_2} + I_3\frac{\partial W}{\partial I_3}\right)\boldsymbol{I} + \frac{\partial W}{\partial I_1}\mathbf{B}^{-1} - I_3\frac{\partial W}{\partial I_2}\boldsymbol{B}\right], \tag{1.3}$$

with $\boldsymbol{\sigma}$ being Cauchy stress tensor, W the strain energy density, $\boldsymbol{B}$ the left Cauchy-Green tensor, $\boldsymbol{I}$ the identity tensor, and I_1, I_2, I_3 being the principal deformation invariants defined by Eq. (1.4):

$$\begin{cases} I_1 = \mathrm{tr}(\mathbf{B}) \\ I_2 = \frac{1}{2}\left[\mathrm{tr}(\mathbf{B})^2 - \mathrm{tr}(\mathbf{B}^2)\right] \\ I_3 = \det(\mathbf{B}), \end{cases} \tag{1.4}$$

This constitutive equation is not fully constrained by the physical properties. The form of the partial derivatives of the strain energy density along the principal strain invariants can be chosen by the user: this choice defines a **model**. The models used in this manuscript correspond to the general definition of hyperelasticity, as stated by Bonet and Wood [11]: *"In the special case when the work done by the stresses during a deformation process is dependent only on the initial state at time t_0 and the final configuration at time t, the behaviour of the material is said to be path-independent and the material is termed hyperelastic"*. Isotropic hyperelastic models rely on the expression of the strain energy density W as a function of strain invariants I_1, I_2, I_3, as stated in Eq.(1.3) or principal stretches $\lambda_1, \lambda_2, \lambda_3$. They can be phenomenological, such as Ogden model [71] or based on micromechanics, such as Arruda-Boyce model [4]. There is a large variety of existing hyperelastic models, either physically based [99], phenomenological [8], and specialised for isotropic materials [65]. Models are fitted to experimental data through the adjustment of different parameters.

For hyperelasticity, there is a large number of models, and choosing the right one to fit a material's behaviour can be a challenge. 85 of them were recently reviewed by He

et al. [43]. Figure 1.2 is generated using Connected Papers app [88], and represents the article network surrounding the review of He *et al.* [43].

The related articles are sorted by similarity: the closer to the centre they are, the more

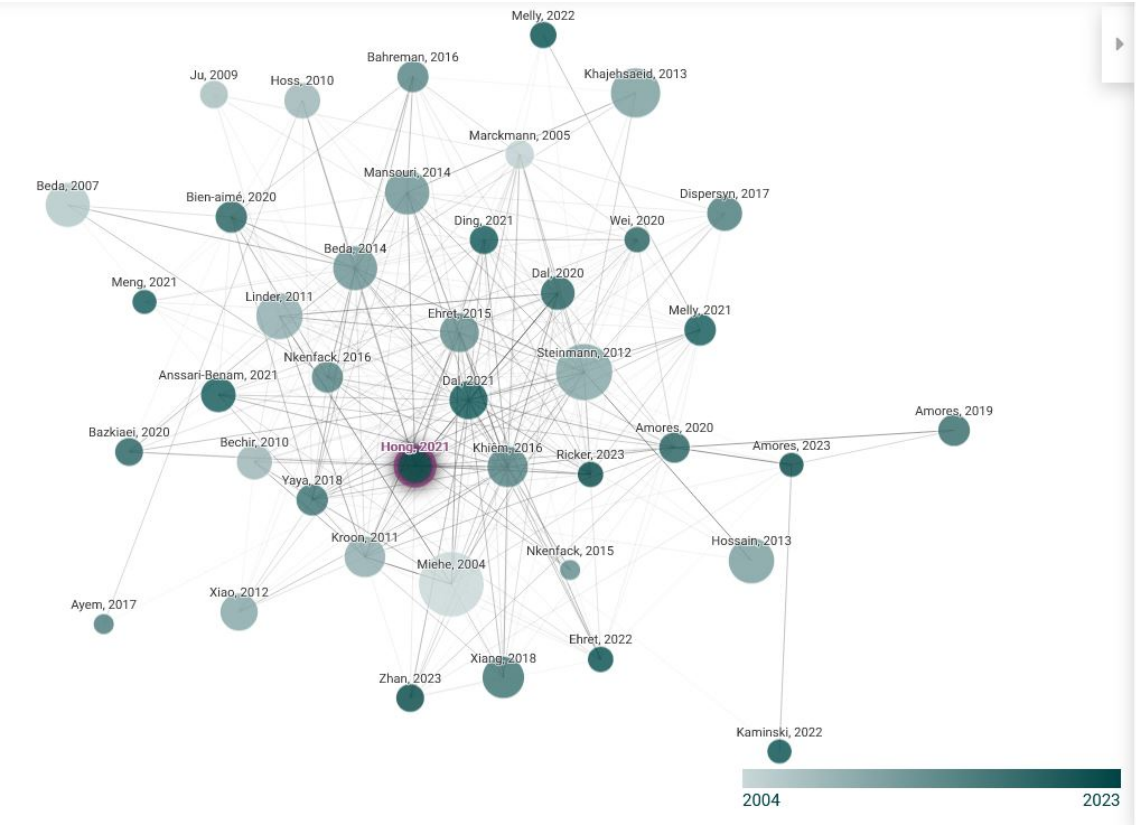

Figure 1.2: Connected Papers [88] chart for He's review on 85 hyperelastic models [43], generated the 15th of June 2023.

similar subjects are covered. The colour of the associated bullet recalls the publication year of the paper, and the darker circles correspond to more recent papers. The area of the circle recalls the number of citations of the related paper. This graph shows that numerous reviews on hyperelastic models have been written through the years. The first one displayed here has been published in 2004 and the last one in 2023. The amount of hyperelastic model reviews published through just twenty years shows that new models are created and tested each year and their number is still increasing, justifying the need for regular reviews. Their number and diversity allows a great adaptation to experimental data, but complexifies the choice of a relevant model.

To conclude this section, and illustrate the diversity of hyperelastic models, three of them are presented. The first is the Edwards-Vilgis model [33], which is a Gaussian chain network model based on micro-mechanics. It involves four different parameters:

$$W = \frac{G_c}{2}\left[\frac{(1-\alpha^2)\,I_1}{1-\alpha^2 I_1} + \ln\left(1-\alpha^2 I_1\right)\right] + \frac{1}{2}G_e\sum_{i=1}^{3}\left(\frac{(1+\eta)\,(1-\alpha^2)\,\lambda_i^2}{(1+\eta\lambda_i^2)\left(1-\alpha^2\sum_{i=1}^{3}\lambda_i^2\right)} + \ln\left(1+\eta\sum_{i=1}^{3}\lambda_i^2\right)\right), \quad (1.5)$$

G_c, G_e, α and η being the parameters of the model. This model is constructed using

both principal stretches and strain invariants. This model has a complex formulation and is very different from the two following polynomial models which are used later in this manuscript. The second one is Ogden's model [71], which is a phenomenological model based on stretch ratios:

$$W = \sum_{n=1}^{N} \frac{2\mu_n}{\alpha_n^2} \left(\lambda_1^{\alpha_n} + \lambda_2^{\alpha_n} + \lambda_3^{\alpha_n} - 3\right), \tag{1.6}$$

N being the order of the model, α_n and μ_n being the parameters of the model. This model is power-law based. It can be used with different orders: choosing the order of the model modifies the number of parameters used as well as the number of mathematical terms in the expression. In this manuscript, second and third-order Ogden's model are considered. The last one is the Yeoh's model [102], a three-parameter phenomenological model in the form of a series expressed in terms of invariants:

$$W = \sum_{i=1}^{3} C_{i0} \left(I_1 - 3\right)^i, \tag{1.7}$$

C_{i0} being the parameters of the model.

1.1.3 Good practices for the use of constitutive laws

Constitutive laws and models are one of the tools engineers use to solve mechanical problems, design industrial part and predict their behaviour. However, every tool comes with safety instructions, and models do not escape the rule. This subsection is dedicated to explaining good practices and safety rules for model users. It focuses on hyperelastic constitutive laws.

Hyperelastic models have to be polyconvex functions of $\boldsymbol{F}$, to satisfy the above-mentionned principles and guarantee the solubility of mechanical problems [6][42]. This property also ensures a smooth fitting procedure when identifying material parameters. This can constrain the validity domain of constitutive law parameters. The associated strain energy density must be positive when the deformation gradient differs from the identity tensor, and equal to zero when the deformation gradient is equal to the identity tensor.

Some of the material properties can constrain constitutive law's formulations. The three principal material properties hypotheses made in this document are hyperelasticity, isotropy and incompressibility. When these three hypotheses meet, the strain energy density can be expressed as a function of two scalar deformation invariants I_1 and I_2 [94], defined by Eq. (1.4). The third invariant, I_3, is fully determined by incompressibility, which forces its value to one. The incompressibility hypothesis implies that the model gives the stress tensor defined without the hydrostatic pressure. The mechanical problem has to be solved to calculate the nine terms of the stress tensor, reduced to six with the balance of angular momentum.

One of the good practices that have to be highlighted is to try to minimise the number of parameters of a constitutive law or material model at the most [98]. It is tempting to develop a material model that will describe perfectly an experimental curve, using as many functions as needed. The danger behind this is to build a model that will be overfitted on the available data but will not be able to describe the material behaviour for different deformation states or ranges. The over-parametrisation can also lead to unstable models or non-unique solutions for identification [61]. There are also compromises to make between the accuracy of the representation and the number of

parameters to adapt. Generally, the more parameters a model offers, the more precisely it can fit the material's behaviour with adequate parameters. However, adapting parameters to experimental data is a costly distance minimisation operation, and its complexity relies mostly on the number of parameters. That is why the following sections will be dedicated to model-fitting approaches.

1.2 Identification: the classical method

The standard identification process relies on simple deformation states experiments, generating homogeneous stress fields in the sample's gauge. Classically, to characterise a material several different deformation states are required. Figure 1.3 presents the method divided into three steps: tests, feature choice and parameters fitting. These steps will be described in the two following sections, then their costs will be qualitatively discussed.

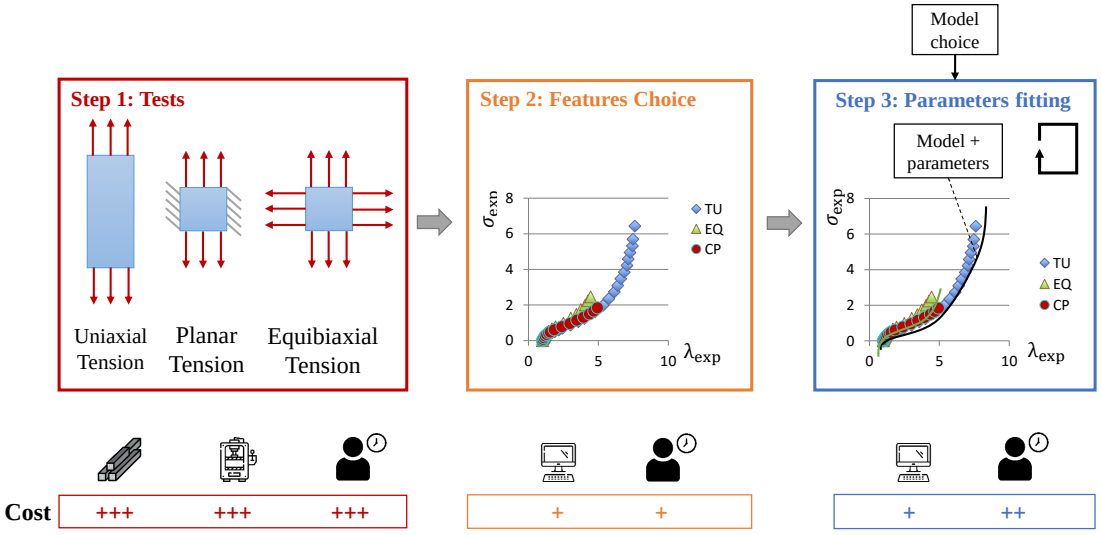

Figure 1.3: Standard identification method process. The identification is based on uniaxial, planar and equibiaxial tension. Data mining and parameter fitting steps are exemplified by Treloar's data [90]. The costs, expressed for each identification step, are human time, testing machine, samples, and computation time. The optimisation procedure is symbolised by the squared looping arrow referring to Equation (1.14) in the third step.

1.2.1 Simple deformation states experiments

Step 1 consists of setting up and running one to several simple deformation state experiments, each of them requiring a specific sample shape and machine setup. Classically, for soft materials, three of them are used for identification purposes:

- Uniaxial Tension, with a dogbone sample mounted on a tensile machine,
- Planar Tension, using large rectangular membrane samples mounted on a tensile machine,
- and Equibiaxial Tension, a deformation state that can be obtained by inflating circular membranes or using cruciform samples in a dedicated bi-actuator machine.

Those tests are designed to guarantee homogeneous stress and strain fields. To ensure this property, the experiments have to be run with carefulness: any misalignment of the experimental set-up could modify the imposed kinematics of the sample, and compromise features choice and fitting.

Step 2 of the identification method consists in calculating features of interest from experimental data. For elastomers, those features of interest can be the measured stretches λ_{exp} and stress $\boldsymbol{\sigma}_{\text{exp}}$ as displayed in Figure 1.3 (here, nominal stresses). The main benefit of these mechanical tests is that they have been developed to ensure that the gauge zone of the specimen undergoes homogeneous strain and stress, in a controlled way. Most of the time, these tests are displacement-controlled, and the machine's cross-bar displacement measurement is the only information needed to capture the kinematics during the experiment. From this displacement and for incompressible materials, the stretch λ can be calculated and the transformation gradient $\mathbf{F}$ is expressed as follows:

$$\mathbf{F}_{\text{UT}} = \begin{bmatrix} \lambda & 0 & 0 \\ 0 & \lambda^{-\frac{1}{2}} & 0 \\ 0 & 0 & \lambda^{-\frac{1}{2}} \end{bmatrix} \tag{1.8}$$

for Uniaxial Tension (UT),

$$\mathbf{F}_{\text{PT}} = \begin{bmatrix} \lambda & 0 & 0 \\ 0 & 1 & 0 \\ 0 & 0 & \lambda^{-1} \end{bmatrix} \tag{1.9}$$

for Planar Tension (PT), and

$$\mathbf{F}_{\text{EQB}} = \begin{bmatrix} \lambda & 0 & 0 \\ 0 & \lambda & 0 \\ 0 & 0 & \lambda^{-2} \end{bmatrix} \tag{1.10}$$

for Equibiaxial Tension (EQB). These particular homogeneous deformation states experiments allow the direct calculation of the associated stress fields. These stress fields can be calculated using a net force measurement and the components of transformation gradient $\mathbf{F}$, as explained by Dal *et al.* [27]. The corresponding Cauchy stress tensors are of the following form:

$$\boldsymbol{\sigma}_{\text{UT}} = \begin{bmatrix} \sigma_{\text{UT}} & 0 & 0 \\ 0 & 0 & 0 \\ 0 & 0 & 0 \end{bmatrix} \tag{1.11}$$

for Uniaxial Tension,

$$\boldsymbol{\sigma}_{\text{PT}} = \begin{bmatrix} \sigma_1 & 0 & 0 \\ 0 & \sigma_2 & 0 \\ 0 & 0 & 0 \end{bmatrix} \tag{1.12}$$

for Planar Tension, σ_1 being measured and σ_2 being unknown, and

$$\boldsymbol{\sigma}_{\text{EQB}} = \begin{bmatrix} \sigma_{\text{EQB}} & 0 & 0 \\ 0 & \sigma_{\text{EQB}} & 0 \\ 0 & 0 & 0 \end{bmatrix} \tag{1.13}$$

for Equibiaxial Tension.

From these strain and stress fields, curves representing the mechanical response of the material for simple deformation state experiments can be plotted. Treloar's experimental data are presented in Figure 1.3 to illustrate the second step of the identification method: the choice of features [91]. Those curves represent the stress response of the material as a function of the imposed stretch. They describe the mechanical response of the tested material for those specific testing conditions. A similar use of simple deformation state experiments for hyperelastic material identification purposes can be found in the literature, for example in Kawabata *et al.* [49] or more recently in Meunier *et al.* [68].

1.2.2 Minimisation problem

Once the experiments run, the experimental features measured and features of interest calculated, the constitutive model has to be chosen. This choice constitutes the beginning of the third step, in Figure 1.3, which consists in fitting the model's parameters through a minimisation procedure, to find the best match with experimental data. It consists of an optimisation procedure:

$$\text{solution} = \arg\min_{\mathbf{y}} \sum_{j=1}^{N} \parallel \hat{\boldsymbol{\sigma}}(\lambda^j_{\text{exp}}, \mathbf{y}) - \boldsymbol{\sigma}^j_{\text{exp}} \parallel_2^2, \tag{1.14}$$

$\mathbf{y}$ being the parameters of the model, $\hat{\boldsymbol{\sigma}}(\lambda^j_{\text{exp}}, \mathbf{y})$ the stress evaluated using the model with parameters set $\mathbf{y}$ and $\boldsymbol{\sigma}^j_{\text{exp}}$ being the N calculated experimental stresses, and where $\parallel \bullet \parallel_2$ defines the quadratic norm, defining a *least square minimisation problem.* In this manuscript, optimisation procedures will be represented by a squared arrow looping around the corresponding optimisation equation reference (see Step 3 in Figure 1.3).

1.2.3 Qualitative costs, benefits and drawbacks

In this section, the term "cost" expresses a qualitative evaluation of the resources needed to complete a set of tasks during an identification process. Those resources are:

- samples,
- testing machine,
- human time for samples preparation, test design and processing, coding,
- and computation time.

These costs are expressed for each identified step of the process: tests, feature choice and parameters fitting. The costs are evaluated qualitatively, highlighting the most costly step of the identification method, and based on the expertise of our research group.

Here, Step 1 consists of setting up and running one to several simple deformation state experiments, each of them requiring a specific sample shape and machine setup. The numerous tests also require time to be run. The three costs identified for this step are material samples, testing machines, and human time. The number of tests required and their specificity, as well as the need for experimental carefulness to guarantee homogeneous fields, increases the qualitative cost of this step. Step 2 consists of choosing features of interest and calculating stress fields from experimental features. The resources for this

step are human time and computational time, and their cost is considered low because of the homogeneity of the fields generated by the tests. Finally, Step 3 consists in the optimisation procedure that requires computational time, evaluated at a low cost because of the simplicity of the procedure, and human time, evaluated at an intermediate cost because the model must be chosen and its validity domain determined.

Two main advantages can be highlighted regarding this identification method. First, the homogeneous tests guarantee the availability of the complete mechanical response of the material for homogeneous tests. Second, the fitting procedure is performed "off-line", that is to say, it is done after the costly steps of the method (Step 1 here), meaning that if a new material model is chosen, the identification process can be done by running the last step only (Step 3). The major drawback of this method is that the characterisation is made on a small number of deformation states. The mechanical response of the material in the general case of non-homogeneous deformation and more complex deformation states are extrapolated from these tests but are not confirmed by experimental means.

The following section describes and explains full-field measurement-based identification methods, highlighting their differences from the present classical identification method and their costs, benefits and drawbacks.

1.3 Identification: full-field measurement-based methods

The major advances made in full-field measurement techniques such as Digital Image Correlation (DIC) [86] led researchers to employ new techniques for identification purposes. This section will first focus on the experimental tests associated with full-field measurement methods, then the numerical identification strategy will be exemplified with the Finite Element Model Updating (FEMU) method, and finally, the benefits and drawbacks of such methods will be pictured using FEMU's costs qualitative analysis.

1.3.1 Experimental test and full-field measurement

Experimental tests Contrary to the classical identification method, methods based on full field measurements have been developed using a unique complex experiment [5]. In his review, Avril states that different types of experiments can be the basis of full-field measurement-based identification methods, among others:

- a tensile test,
- the Brazilian test,
- a shear-flexural test,
- a biaxial test.

The tensile test exhibits homogeneous strain and stress fields if run perfectly. Using it with a full-field measurement method allows us to capture some of the uncertainties regarding the experimental setup [41]. The three other tests display non-uniform strain fields in the region of interest: Digital Image Correlation is used to measure these fields. The Brazilian tests consist of a diametrical compression of a cylindrical sample. It is mostly used to characterise brittle materials. The application of a vertical diametrical load on a cylindrical sample induces tensile stresses in the perpendicular direction that leads to failure in the central part of the sample. The shear-flexural test has been developed by Pierron and Grédiac to characterise concrete with a unique test [78]. The concrete

specimen is undergoing shear stresses and bending at the same time, making it behave like a straight rectangular beam in which all the plane stress components are present. During this test, the sample exhibits tension along one axis, compression along the second and shear. It allows measuring the corresponding stiffness. Other types of experiments can be designed and used for full-field measurement-based identification methods, as long as the experimental kinematic fields can be measured satisfactorily, as shown in the work of Pierron and Grédiac [79].

Full-Field measurement The development of Digital Image Correlation [86] allowed scientists to capture and save features using optical tools. Digital Image Correlation (DIC) is an optical method that uses imaging techniques to measure changes from one picture to another. DIC tracks position changes of a point, a surface or even an object (using stereo-DIC). In the following, the focus is laid on 2D-DIC, performed with a single camera. This method is based on digital images in black and white, capturing an object at a fixed rate. Those numerical images are large tables containing integer values between 0 and 255, describing the grey level of the corresponding pixel. A representation of those grey-level variations can be found in Peters and Ranson's work [76]. When the object is deformed, the grey level table is altered as the image changes. A local optimisation process calculates each pixel's displacement by minimising the residual between the deformed image and the reference image. The objective function is defined as follows:

$$\boldsymbol{\Phi}(\boldsymbol{u}) = \int_{\Omega} \left[f(\boldsymbol{x}) - (g(\boldsymbol{x} + \boldsymbol{u}(\boldsymbol{x}))\right]^2 \mathrm{d}\boldsymbol{x}, \tag{1.15}$$

with $\boldsymbol{x}$ the coordinates of the pixel, f the signal of the reference picture, *i.e.* the initial gray level table, g the signal of the deformed picture, *i.e.* the altered grey level table, and $\boldsymbol{u}$ the displacement field, calculated on Ω, the region of interest defined on the reference picture. This type of objective function necessitates a non-linear least-square solver. This method has rapidly been adapted to experimental mechanics [17].

The problem is ill posed because it is based on the minimisation of a scalar equation whereas the displacement field is vectorial. A regularisation method has to be applied for the resolution. Usually, the regularisation method assumes the general form of the displacement field. Two principal types of resolution strategies are considered: global resolution and local resolution. The local resolution method usually assumes compact support displacement fields, and searches for the displacement of sub figures one by one. In this work, the focus is laid on the global resolution method, in particular Finite Element DIC as proposed by Besnard *et al.* [9]. The method splits the region of interest into mesh elements and discretises the resolution process using form functions. The displacements of every mesh node is searched. Considering Equation (1.15), and assuming that g is differentiable, and using a displacement increment $\mathrm{d}\boldsymbol{u}$, we can write:

$$f(\boldsymbol{x}) \approx g(\boldsymbol{x} + \boldsymbol{u}(\boldsymbol{x})) + \nabla g(\boldsymbol{x} + \boldsymbol{u}(\boldsymbol{x}))\mathrm{d}\boldsymbol{u}. \tag{1.16}$$

Once the differential expression of the deformed image is written, the displacement $\boldsymbol{u}$ can be written using form functions inspired by Finite Elements as:

$$\boldsymbol{u}(\boldsymbol{x}) = \sum_{\alpha,n} a_{\alpha,n}\psi_n(\boldsymbol{x})\boldsymbol{e}_\alpha, \tag{1.17}$$

with $\boldsymbol{e}_\alpha$ being a unit vector, $a_{\alpha,n}$ the magnitude of $\boldsymbol{u}$ along direction α according to scalar form function ψ_n. $\mathrm{d}\boldsymbol{u}$ naturally satisfies the same functional definition. This expression of $\boldsymbol{u}$ allows us to write a second objective function including the form functions:

$$\mathbf{\Phi}(\mathrm{d}\boldsymbol{u}) = \int_\Omega \left[-\sum_{\alpha,n} \mathrm{d}a_{\alpha,n}\psi_n(\boldsymbol{x})\nabla g(\boldsymbol{x})\cdot\boldsymbol{e}_\alpha + f(\boldsymbol{x}) - g(\boldsymbol{x}+\boldsymbol{u}(\boldsymbol{x})) \right]^2 \mathrm{d}\boldsymbol{x}. \tag{1.18}$$

From this objective function, a linear system of equations can be defined and then solved to calculate the displacement field:

$$\sum_{\beta,m} \mathrm{d}a_{\beta,m} \int_\Omega \left[\psi_m(\boldsymbol{x})\psi_n(\boldsymbol{x})(\nabla f\cdot\boldsymbol{e}_\alpha)(\boldsymbol{x})(\nabla f\cdot\boldsymbol{e}_\beta)(\boldsymbol{x})\right]\mathrm{d}\boldsymbol{x} = \int_\Omega \left[g(\boldsymbol{x}+\boldsymbol{u}(\boldsymbol{x})) - f(\boldsymbol{x})\right]\psi_n(\boldsymbol{x})(\nabla f\cdot\boldsymbol{e}_\alpha)(\boldsymbol{x})\mathrm{d}\boldsymbol{x}. \tag{1.19}$$

The system is solved by finding the appropriate displacements magnitudes $\alpha_{\beta,m}$ and corresponding unit vectors $\boldsymbol{e}_\alpha$. Smoothing methods and filters can be applied if the noise is considered too high. Details on processes and advice can be found in Lubineau's work [59]. Several softwares are now running DIC and a comparison based on a DIC challenge has been proposed in 2018 [83]. One of the major parameters for a good FE-DIC result is the match between the speckle pattern size and the mesh element size, as discussed by Pan *et al.* [74]. Other recommendations regarding lighting, speckle pattern size and distribution can be easily found in the literature, for example in the book of Schreier *et al.* chapter 10 [85]. Pan *et al.* discusses the choice of correlation criteria for DIC [73]. Roux and Hild detail the optimal procedure for setting DIC for identification purposes [84][44]. Archbold *et al.*proposes a framework for in-plane surface displacement measurements with double-exposure speckle photography [3]. Regularisation is a central procedure in DIC, and diverse methods have been developed; for example, Cofaru *et al.* proposes to include an adaptative spatial regularisation in the minimisation process to improve displacement measurements [20]. Some adaptations can be made to study crack propagation with the help of DIC [64]. The Good Practices Guide developped by International Digital Image Correlation Society provides further advice on DIC implementation [47]. The DIC method and parameters chosen and used in this work are described in Section 3.2.3.

Full-field measurement-based identification methods Several field measurement and fitting methods have been proposed: the Constitutive Equation Gap Method (CEGM) [72], the Virtual Fields Method (VFM) [40], the Equilibrium Gap Method [19], the Reciprocity Gap Method [2], or EUCLID (Unsupervised discovery of interpretable hyperelastic constitutive laws) [37], which uses Neural Networks to find the best combination of constitutive laws to build a tailored model for given experimental data. Another approach based on FE-like strain energy density computation uses least-square minimisation to fit a combination of constitutive laws or material models on experimental data [97]. The efficiency of these methods is based on the quality of experimental measurements, especially on measurement noise as stated by Roux: *"identification appears as a compromise between a constitutive law describing a material and noise corrupting the measurements"* [84].

The following section will focus on the Finite Element Model Updating method as an example of a full-field measurement-based identification method.

1.3.2 Numerical identification strategies: the example of Finite Element Model Updating (FEMU)

Contrary to simple deformation state experiments, complex experiments do not allow the direct calculation of stress fields: numerical strategies are necessary to fit model

parameters by making numerical features match experimental features. It is the case of the Finite Element Model Updating method (FEMU) [46], which is based on successive finite element simulations based on an *a priori* choice of the model. Thus, this process leads to the best set of parameters for a given model. The groundwork of this method can be found in Kavanagh and Clough, questioning the use of Finite Elements for material characterisation purposes [48].

The finite Element Model Updating method can be divided into two successive steps, as shown in Figure 1.4:

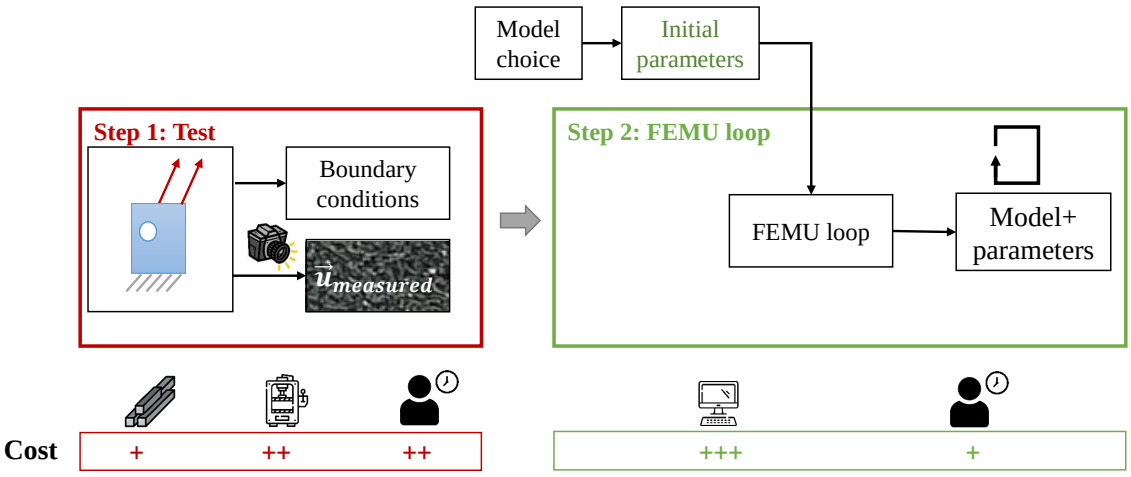

Figure 1.4: FEMU identification process. The costs, expressed for each identification step, can be human time, testing machine, material or samples, and computation time. The optimisation procedure is symbolised by the squared looping arrow referring to Equation (1.20) in the second step.

Step 1 is experimental and consists of setting up and running a single experiment, that can be referred to as "complex" as opposed to simple deformation state experiments, and Step 2 is numerical. The complexity of the experimental test steps from sample geometry, for example including holes, and/or from prescribed kinematics with complex loading conditions. This "complex" test generates a heterogenous stress field. This unique test requires an appropriate sample and testing machine and a full field measurement setup. In FEMU, displacement fields are often measured using Digital Image Correlation, as seen in the previous section. The sample is then discretised with Finite Elements, and this mesh is retained for the FEMU loop. Once the displacement field is measured, a model has to be chosen with arbitrary initial parameters to begin the numerical step (Step 2). The model and the initial set of parameters are considered inputs for the FEMU method, as well as the measured displacement field and net forces. The Finite Element model is built using the geometry and boundary conditions of the complex experiment. After the finite element simulation is run, the resulting displacement field is compared with the displacement field measured during the experiment. If their agreement is not considered satisfactory, the parameters are updated, giving the name to the method and building a new Finite Element model, and a new finite element simulation is run.

Parameter updates can be made using several methods. The classical one relies on

gradient-based methods such as gradient or steepest descent. Other methods such as the Newton-Raphson method or quasi-Newton method can be applied for the parameters update. The method iterates until reaching the minimal distance between discretised experimental displacement field $\{U\}$ and discretised numerical displacement field $\{V(y)\}$ with respect to the current set of parameters $\mathbf{y}$:

$$\text{solution} = \arg\min_{\mathbf{y}}(\{U\} - \{V(\mathbf{y})\})^T(\{U\} - \{V(\mathbf{y})\}), \tag{1.20}$$

Throughout the FEMU optimisation loop, experimental net forces are used as constraints to ensure the reliability of the resulting parameters set. The output of FEMU is the optimal parameters set for the chosen model, and the predictive quality of the resulting model highly depends on the choice of model made *a priori*. When the optimisation procedure aims to minimise the distance between measured and simulated displacements, the method is called U-FEMU. In fact, the classical U-FEMU has been presented in this section: the measured displacement field is considered as the reference feature with which the computed displacement field will be compared in the objective function formulation.

Other features can be used as reference features to build the objective function. In the literature, strain, net forces or stresses are part of the FEMU objective function, as discussed in Ienny *et al.* review [46]. FEMU can be written differently and rely on a different objective function. F-FEMU is a FEMU procedure which minimises the distance between measured net forces and calculated FE resulting forces. The objective function is:

$$\text{solution} = \arg\min_{y} \frac{1}{M-p} \sum_{m=1}^{M} \left(\frac{F^{\text{exp}}(t_m) - F^{\text{FE}}(t_m)}{|F^{\text{exp}}|_{\max} - |F^{\text{exp,mean}}|} \right)^2, \tag{1.21}$$

where p is the number of material parameters, t_m the time instant and M is the number of time steps.

FEMU is well suited for identification of complex behaviours, such as hyper-viscoelastic behaviours as shown by Tayeb *et al.* [89] who used FEMU to fit a Yeoh model with Prony series to characterise the hyper-viscoelastic behaviour of an elastomer. The heterogenous test of their study is a relaxation test on a cruciform sample.

1.3.3 Qualitative costs, benefits and drawbacks

For full-field measurement-based identification methods, the qualitative costs can be expressed for each step of the process: the experimental step (Step 1) and the numerical step (Step 2). For the experimental part, the cost is evaluated low, because only one test is needed to perform the identification method. This places the full-field measurement-based identification methods above the classical identification method for the material sample costs. At the same time, machine and time are evaluated to be at an intermediate cost for the experimental set up including Digital Image Correlation. Step 2 is purely numerical, and the two identified costs are computation time and human time. The human time is evaluated short, and the major cost comes from the computation time of the FEMU loop. This computation time depends on the complexity of the finite element model to run, including the complexity of the mesh, the number of loading steps and the complexity of the model considered and the necessary number of iterations, i.e. the number of FE computations to convergence.

Another major issue is that the identification problem is often ill-posed. The objective function often presents numerous local minima and no global minimum. The minimisation procedure can be really costly and a FE computation remains necessary at each algorithm iteration.

1.4 Conclusion

Finally, constitutive laws can be seen as key tools for material science. These tools are necessary for most computational mechanics methods. A large diversity of constitutive laws exist, and each one of them gathers its particularities. This variety of models induces a need for extreme carefulness when selecting a model to model the response of a given material. Their domain of validity and a number of parameters have to be chosen carefully.

Adapting a material model to experimental data to describe a material's behaviour is called identification. Figure 1.5 proposes an overview of the qualitative costs detailed previously for the historical identification method and the FEMU method. The historical identification method allows a direct calculation of stress and an easy fitting procedure but needs several experimental tests, as illustrated with the qualitative costs presented in Figure 1.5. Moreover, the extrapolation from simple deformation states to multiaxial deformation can generate some errors. Full-field measurement-based identification methods work with a single multiaxial experiment. However, in this case, the stress fields are not directly available, and costly numerical strategies have to be run to carry on the identification process, as illustrated in Figure 1.5.

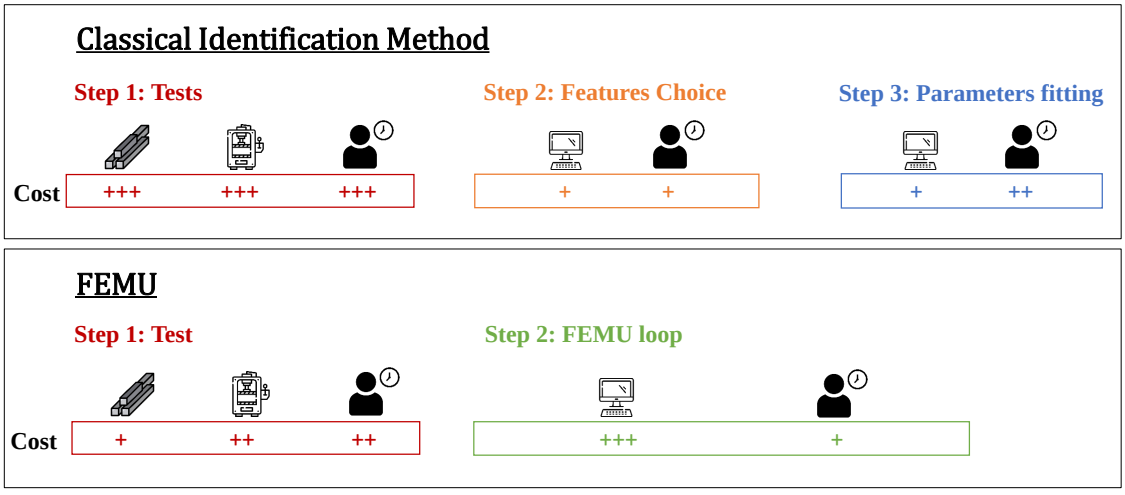

Figure 1.5: Qualitative costs evaluation comparison for Classical Identification method and FEMU. The description of the different steps can be found in Figures 1.3 and 1.4.

Considering the complexity and challenges induced by constitutive laws and identification, the present work explores data-driven identification methods for incompressible isotropic hyperelasticity. The objectives of the study are presented in the following.

Chapter 2

Objectives and tools

This chapter focuses on setting and describing the objectives of the study:

- setting up and running multiaxial tests,
- develop a visualisation tool to describe the kinematics of the experiments,
- enhance the visualisation tool to encompass the stress response of the material,
- develop an identification method based on multiaxial tests and relying on an "off-line" choice of the model,
- and use the kinematic visualisation tool to improve the test's deformation modes diversity.

The carbon-black-filled SBR that is used for experimental purposes is studied through uniaxial tension tests, relaxation tests, cyclic uniaxial tension tests and Dynamical Mechanical Analysis (DMA). It exhibits some viscous properties and is subjected to the Mullins effect. The upcoming experimental tests are run with progressive loading to avoid triggering the Mullins effect and fixed slow strain rates to minimise viscous effects.

The software used in this study is presented at the end of the chapter.

Contents

Identifying the mechanical response of a material remains challenging. Choices have been made to carry out this PhD work and provide insights into hyperelastic material behaviour. The goal of this project is to build and describe tools to characterise the complete mechanical response of an hyperelastic isotropic incompressible material, using a single multiaxial test run with a planar sample. The first section of this chapter details the objectives of the study while the second section presents the material, samples and software used in the following.

2.1 Objectives of the thesis

This study focuses on the response of soft materials, especially elastomers. Classically, they are assumed isotropic and incompressible and we consider hyperelastic models to reproduce their mechanical response under large strain.

2.1.1 Material behaviour and multiaxial tests

The mechanical response of a material, which is often summarised by a model associated with chosen parameters, is constituted of a kinematic part and a stress part. This work will focus on both aspects successively.

These studies are conducted both on synthetic and experimental data. The focus is laid on multiaxial tests conducted on planar elastomeric membranes with punched holes. Data has to be generated and gathered to conduct these studies. **Chapter 3 details the methods used to generate synthetic data and collect experimental data from multiaxial tests on elastomeric planar membranes.**

2.1.2 Towards an exploration of kinematics

Within the broader framework of continuum mechanics, the study of kinematics involves measuring and characterising the deformation of a body (in fact a sample) during a test. When utilising multiaxial tests for identification purposes, there arises a necessity to thoroughly examine, describe, and characterise such tests. The wide range of deformation modes and intensities observed during these tests significantly impacts the quality of identification.

In the context of kinematics and material deformation, strain tensors play a crucial role in capturing the relationship between applied forces and observed strain. However, accurately representing and interpreting these tensors can be a daunting endeavour. As the dimensionality of tensors increases, so does the complexity of understanding their meaning. Moreover, visualising tensors with more than three dimensions becomes especially challenging. This can be an issue when working in the experimental world, with three-dimensional objects and strain tensors with nine components, as illustrated in Figure 2.1.

To address this question of visualisation, **Chapter 4 aims to develop a graphical tool that effectively describes the kinematics of a comprehensive and intricate mechanical test.**

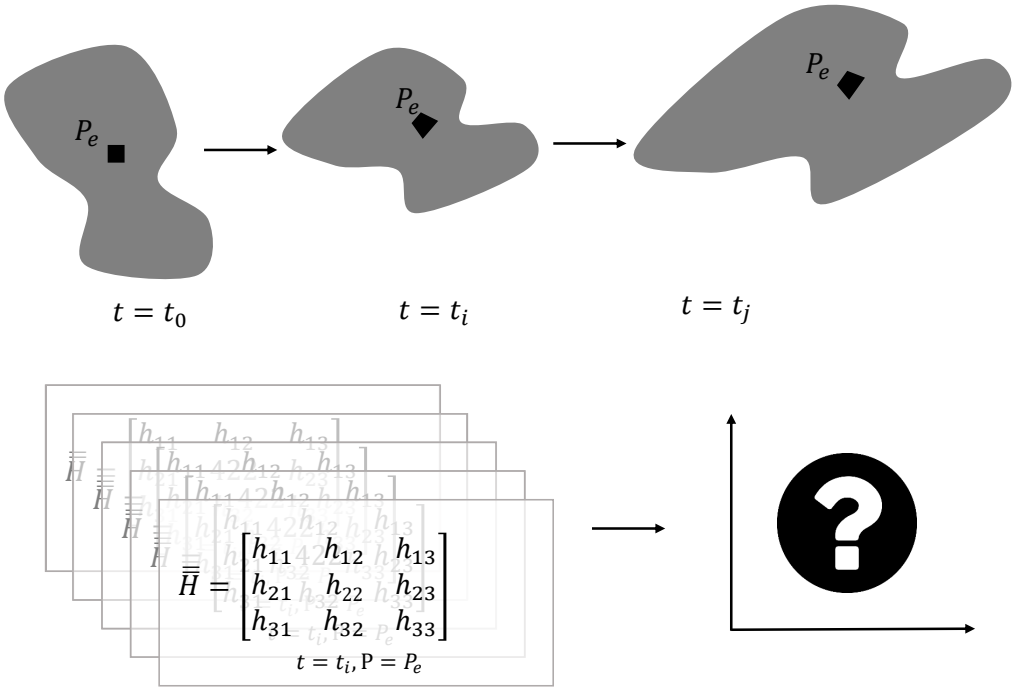

Figure 2.1: Illustration of the difficulty of representation for solid body kinematics. The concept is illustrated with a series of Hencky's logarithmic strain tensors corresponding to material points at given time steps.

2.1.3 Towards an exploration of stresses without a constitutive law

Once we can accurately describe the diversity and quality of kinematic data obtained from an experiment, there arises a subsequent aspect of the material response: stresses. Traditionally, stresses are calculated using constitutive laws, models and associated parameters. However, in recent years, non-parametric methods have emerged as an alternative approach to construct new forms of material modelling, as exemplified by Montans [69]. This paradigm shift, where material data is represented by extensive databases instead of relying on a continuous manifold derived from a constitutive law, has been investigated by Kirchdoerfer and Ortiz in the Data-Driven Computational Mechanics (DDCM) paradigm [50]. Inspired by this novel approach, Leygue *et al.* developed Data-Driven Identification [57], a method that enables the calculation of multiaxial stress fields without any reliance on constitutive laws, as illustrated in Figure 2.2.

In line with this innovative approach, **the objective of Chapter 5 is to derive stress fields from multiaxial experiments without the need for constitutive laws or modelling assumptions. Once these stress fields are accurately calculated and described, the aim is to enhance the previous kinematic graphical tool to encompass a comprehensive representation of the material's complete mechanical response.**

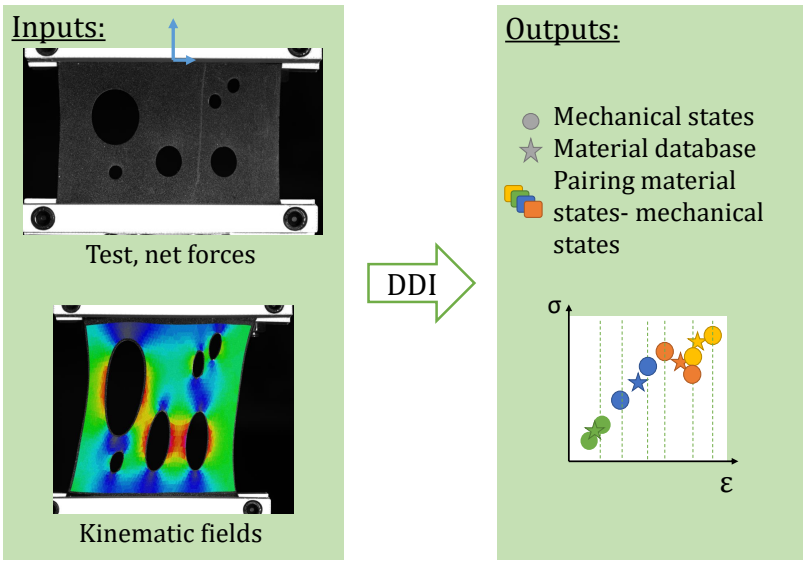

Figure 2.2: Illustration of Data-Driven Identification (DDI) principle: the inputs are experimental net forces, geometry and kinematic fields and the outputs are stress-strain couples; the mechanical states are the solution of the mechanical problem and the material states sample the mechanical response of the material.

2.1.4 Experimental applications

The availability of graphical tools to describe and characterise multiaxial tests generates numerous applications. Some experimental applications have been developed during this PhD project.

The first application described in **Chapter 6** is a **new identification method, bringing together Data-Driven methods and constitutive modelling**. This method will gather the benefits of an offline parameter fitting and the use of a multiaxial test as identification data.

The second application developed in **Chapter 7** consists in **using the kinematics graphical tool to enhance the diversity of the kinematical states observed during one multiaxial test.**

2.2 Tools for data acquisition

Some tools are necessary to achieve the objectives presented above. The next subsection is dedicated to the presentation and characterisation of the materials and samples used in the experimental studies. The second subsection references the software and numerical tools used for computation.

2.2.1 Test bench

The tests were conducted on a Symetrie Breva hexapod device shown in Figure 2.3.

This kind of device was first designed for driving simulators or precisely positioning mirrors of telescopes. Six electrical actuators link the fixed base to a moveable upper

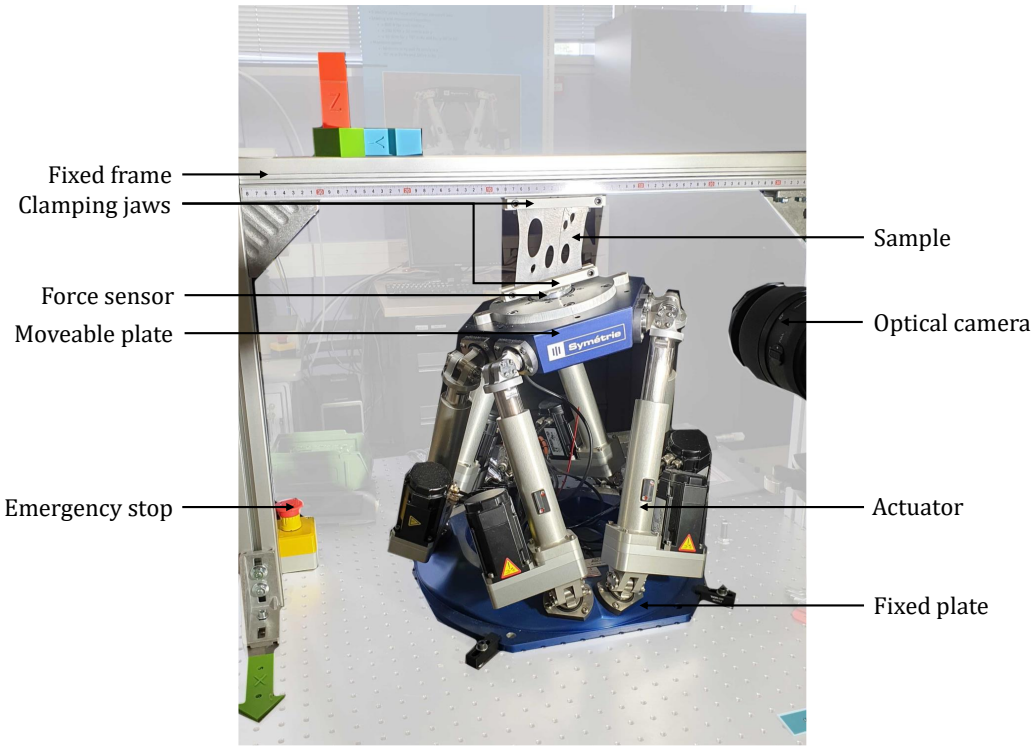

Figure 2.3: Experimental setup for planar membranes testing.

platform. The system can be moved along the six degrees of freedom, component by component or follow a given positioning trajectory. The Breva device used here has an amplitude of 80 mm along the vertical (z) axis, and 100 mm along the horizontal (x and y) axis, as well as 40° amplitude for each rotation. Those amplitudes depend on the position of the platform because the six jacks have physical limits and cannot reach every position. Free software called Hexasym is available on Symetrie website [87] to prepare and validate trajectories to be followed by the upper platform. The clamping jaws were 3D printed to be fully adapted to sample dimensions and hexapod setup, which is shown in Figure 2.3. A six-axis sensor located in the moveable platform acquires forces and momentum in the three directions during the test. The sensor is made by Interface©, model 6A40A-00N. Its characteristics are given in Table 2.1.

F_x (N)	F_y (N)	F_z (N)	M_x (Nm)	M_y (Nm)	M_z (Nm)
200	200	500	5	5	10

Table 2.1: Force sensor characteristics. The z-axis is the fixed plate orthogonal axis.

The force acquisition can be synchronised with the test start and the camera acquisition using a connected trigger device. The camera is made by Vieworks, model *Vieworks VC-50MX-M30E0* and a lens from Tokina, model *atx-i 100*mm *F2.8 FF Macro* is used for capturing the sample's deformations. This test bench is located in a controlled temperature room, with a fixed 24°C temperature. Some machine limitations must be checked when building complex tests on hexapod devices. Those are summarised in Table 2.2, and must be considered when imposing displacements on the device. Those limitations induced some experimental choices, such as limiting any slope break when setting imposed displacements. Most of the time, inserting a quarter sine period at the beginning or the end of the imposed displacement guarantees a sufficiently smooth acceleration.

Feature	Limit	Unit
Maximal actuator length	337.0	mm
Minimal actuator length	258.0	mm
Actuator speed	50	$mm.s^{-1}$
Actuator acceleration	110	$mm.s^{-2}$
Actuator load	340	N
Actuator power	0.04	kW
Fixed platform angle (cardan)	55.0	°
Mobile platform angle (cardan)	55.0	°
Screw speed	14 323.9	tr/min
Screw acceleration	345.6	$rad.s^{-1}$
Motor power	0.10	kW
Motor torque	0.5	N.m
Motor speed	2500.0	tr/min
Motor acceleration	500	$rad.s^{-2}$
Motor intensity	3.00	A
Motor tension	60.00	V
Machine power	1.12	kW
Actuator displacement	0.06	m

Table 2.2: Hexapod device limits.

Although the force acquisition is synchronised with the hexapod command software, some trigger issues did occur during our experimental campaings. Investigations have been conducted to identify the causes of those trigger issues, that are surprisingly reproducible as the repetition of some experiments displays the same trigger issues. Another surprising result is that the slower tests do not show the same trigger issues, that is to say, the issues do not appear when the crossbar displacement is "too slow to detect" as we first thought. Finally, a change of format in the input files was able to resolve this trigger issue.

2.2.2 Material and samples

Despite the strong will to take some distance from traditional mechanical characterisation, simple experiments were essential to grasp our material's properties. This work is conducted in partnership with Michelin which provides material samples of carbon-black-filled Styrene-Butadiene Rubber (SBR). The provided samples are seven planar membranes of 250×65 mm^2 area, with cylindrical bulges, as seen in Figure 2.4.

The thickness of the plate varies along the plate, with an average of 1.6 mm. The local thickness variations are around 10^{-2} mm. The glass temperature of the material is estimated at around -65 °C. Three types of samples were extracted from the original plates: 10×65 mm^2 samples for uniaxial tension tests, relaxation tests and cycling tension tests; 100×65 mm^2 samples for multiaxial tests; and 10 mm height cylindrical samples for Dynamical Mechanical Analysis (DMA).

Figure 2.4: Samples extracted from the large plate: two large 100×65 mm^2 samples and five 10×65 mm^2 samples for traction tests. The plate displayed is ANR1. The dimensions of the white squares in the background are 1 cm^2.

2.2.2.1 Uniaxial tension tests

Methods Uniaxial traction tests were conducted with constant Hencky strain rate ($\dot{\epsilon}$), on a hexapod machine shown in Figure 2.3, with maximal hexapod vertical amplitude of 80 mm, corresponding to a stretch of $\lambda = l/l_0 = 2.23$. This series of experiments aimed to assess the viscoelastic behaviour of the material in the displacement velocity range accessible by the device. Nine samples were tested, each with a fixed $\dot{\epsilon}$ value. In our case, as long as the testing machine is driven by displacement, it can be expressed as:

$$\dot{\epsilon} = \text{cst.} \tag{2.1}$$

And as long as

$$\epsilon = \ln(\lambda), \tag{2.2}$$

we have:

$$\dot{\epsilon} = \frac{\dot{\lambda}}{\lambda} \tag{2.3}$$

$$\Rightarrow \dot{\lambda} = \dot{\epsilon}\lambda. \tag{2.4}$$

So it occurs that

$$\lambda = \alpha e^{\dot{\epsilon}t}, \tag{2.5}$$

with l_0 the rest length of the sample, of 65 mm, t the time if the experiment in seconds, and a constant. The chosen values of strain rates $a = \dot{\epsilon}$, the associated maximal stretch rate $\dot{\lambda}_{\max}$, and the duration of the test are given in Table 2.3. The force sensor values are updated every hundredth of a second. The starting condition $\lambda = 1$ at the start of the experiment, for $t = 0$ imposes $a = 1$. This notation will not be conserved in the rest of the development. Finally, according to the relation between $\boldsymbol{u}$ and λ

$$\lambda = 1 + \frac{\|\boldsymbol{u}\|}{l_0} \tag{2.6}$$

$$\Rightarrow \boldsymbol{u}(t) = l_0(e^{\dot{\epsilon}t} - 1)\boldsymbol{z}, \tag{2.7}$$

$\boldsymbol{z}$ being the vertical unit vector.

Specimen identification	$\dot{\epsilon}$ (s^{-1})	$\dot{\lambda}_{max}$ (s^{-1})	Duration of the test (s)
2021-03-10-ANR1-65x10mm-1	0.16	0.357	5.01
2021-03-10-ANR1-65x10mm-3	0.1	0.223	8.02
2021-03-10-ANR1-65x10mm-4	10^{-2}	2.23×10^{-2}	80.23
2021-05-03-ANR1.1-65x10mm-1	10^{-2}	2.23×10^{-2}	80.23
2021-05-03-ANR1.1-65x10mm-2	10^{-2}	2.23×10^{-2}	80.23
2021-03-10-ANR1-65x10mm-2	10^{-3}	2.23×10^{-3}	802.34
2021-03-10-ANR1-65x10mm-5	10^{-4}	2.23×10^{-4}	8023.46
2021-04-14-ANR3-65x10mm-5	10^{-4}	2.23×10^{-4}	8023.46
2021-03-10-ANR2-65x10mm-5	5×10^{-5}	4.46×10^{-5}	40117.30

Table 2.3: Strain rate, maximal stretch rate and duration of the test for each experiment.

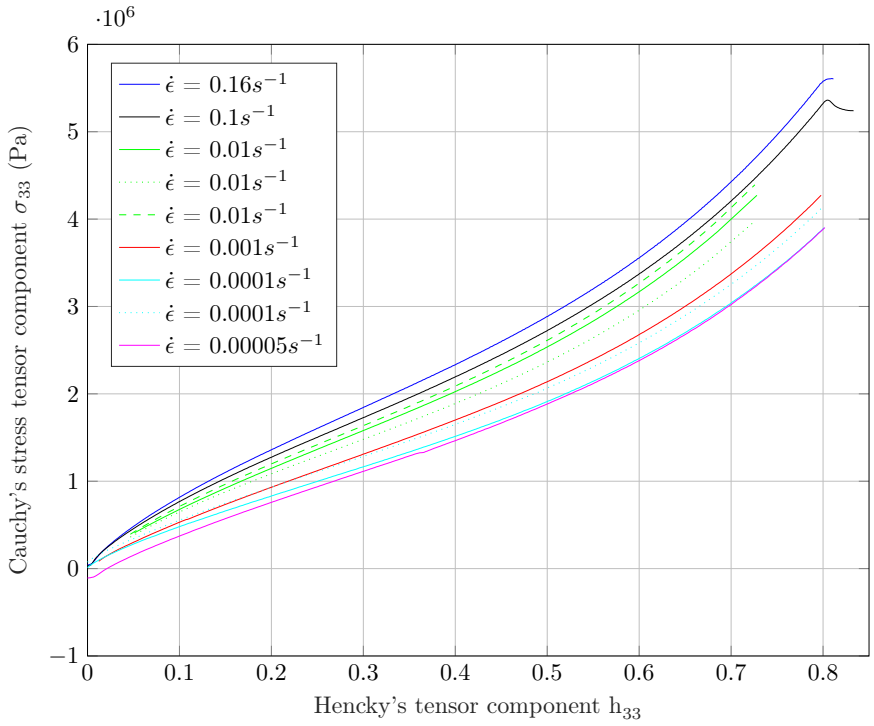

Figure 2.5: Experimental uniaxial tension curves on filled rubber for six different strain rates at 24°C.

Results The results of this series of experiments are displayed in this section. Figure 2.5 shows the uniaxial Cauchy stress as a function of Hencky strain in the loading direction.

It displays a difference between the nine tests conducted. Classically, the slower the loading, the lower the stress is. This confirms the viscous nature of the material tested. Otherwise, the general shape of the curves is pretty similar. The duplication of tests with similar strain rate exhibits a good reproducibility. The small differences between the three slower tests, corresponding to $\alpha = 10^{-4}$ s^{-1} and $\alpha = 5 \times 10^{-5}$ s^{-1} suggests that there is no demonstrative viscous behaviour for these strain rates. Dynamical Mechanical Analysis tests have been run to ensure that the multiaxial tests will trigger mainly hyperelastic effects and negligible viscoelastic behaviour.

Remarks Some remarks can be made about the results obtained during this characterisation campaign. In the experimental setup, the Hexapod command is synchronised with the acquisition and triggers the start and the end of the writing of the output file. The curves of Figure 2.5 corresponding to $\dot{\epsilon} = 0.16$ s^{-1} and $\dot{\epsilon} = 0.1$ s^{-1} seem to have had a bad end trigger timing and continued measuring features after reaching the imposed strain. About some other curves, a start trigger issue seems to have happened for the ones corresponding to $\dot{\epsilon} = 0.01$ s^{-1}, which also displays an end trigger issue. The first force values written in the file were one or two orders of magnitude higher than the values accepted when setting the zero. The values have been artificially shifted.

Another source of difference between the curves could be a manifestation of the Mullins effect since we tested all the samples on the first tension. Some tension tests should be conducted after a five-cycle "demullinisation" process on a filled SBR sample to characterise this effect, as well as a tension-relaxation cyclic test.

2.2.2.2 Relaxation tests

Methods Some elastomers exhibit viscous behaviours [38], and one way to characterise it is to conduct relaxation tests. Relaxation tests were conducted on Symetrie Breva hexapod device, which is displacement-driven during the tests. The goal of this series of tests was to go a bit further on assessing the viscoelastic behaviour of the material and stating if the viscous effects observed during traction tests will manifest themselves during multi-axial tests, or in the range of stretches and times available on the hexapod device. Those tests consist of two different phases, as shown in Figure 2.6: a loading phase, from $t = 0$ to $t = t_{\text{load}}$ and a holding phase, for a duration of t_{stat} from $t = t_{\text{load}}$ to the end of the experiment, $t = t_{\text{load}} + t_{\text{stat}}$.

The device accepts high displacement speeds of up to 25 mm.s^{-1}, but cannot undergo slope breaks when rejoining a command plateau. It was then decided to follow a half-period sinusoidal curve during the loading phase to avoid issues linked to slope breaks:

$$u(t) = \frac{u_{\max}}{2}\left(\cos\left(\frac{\pi v_{\text{moy}}}{u_{\max}}t\right) - 1\right), \tag{2.8}$$

with $u(t)$ the vertical displacement of the machine plate as a function of time t, $u_{\max}$ the maximal vertical displacement of the machine and v_{moy} the chosen average displacement speed. The average displacement speed for the loading phase is set to $v_{\text{moy}} = 16$ mm.s^{-1}. The static phase was set to a duration of 300 s for two samples and 1000 s for the others. Table 2.4 summarises each experiment's imposed strain and average displacement speed.

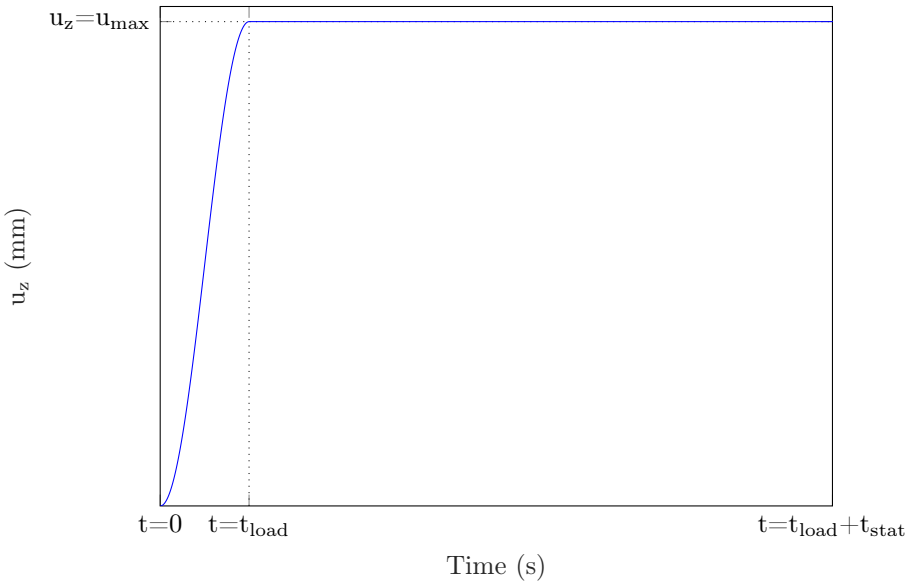

Figure 2.6: Displacement command shape for relaxation tests with sinusoidal loading.

Test Number	λ_{max}	Average speed in loading phase ($mm.s^{-1}$)	Holding phase duration (s)
2021-03-10-ANR2-65x10mm-2	2.2308	16	300
2021-04-14-ANR3-65x10mm-2	2.2308	16	10000
2021-03-10-ANR1-65x10mm-3	2	16	300
2021-04-14-ANR3-65x10mm-3	2	16	10000
2021-03-10-ANR2-65x10mm-4	1.8	16	10000
2021-04-14-ANR3-65x10mm-1	1.5	16	10000
2021-04-14-ANR3-65x10mm-4	1.1	16	10000

Table 2.4: Fixed strain and average displacement speed in the loading phase for each experiment.

Results The results of relaxation experiments are displayed in Figure 2.7, which shows vertical force amplitude as a function of time.

Classically, the slower the sollicitation, the lower the vertical component of the force is. A change of slope can be observed around $t = 0.2$ s and $t = 1$ s for $\lambda = 2.2308$ and $\lambda = 2$ experiments respectively. It can be observed on normalised vertical force values in Figure 2.8 that there are multiple slope breaks and different behaviours.

Those multiple slope breaks occur at three characteristic times: $t = 2 \times 10^{-1}$ s, $t = 2$ s

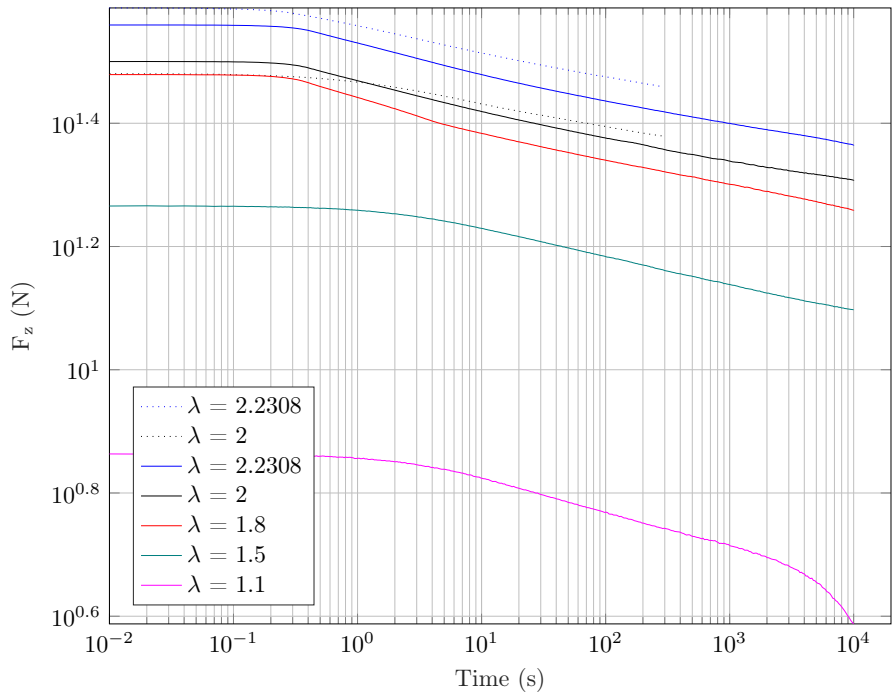

Figure 2.7: Experimental relaxation curves on filled rubber for five different imposed strain levels at 24°C.

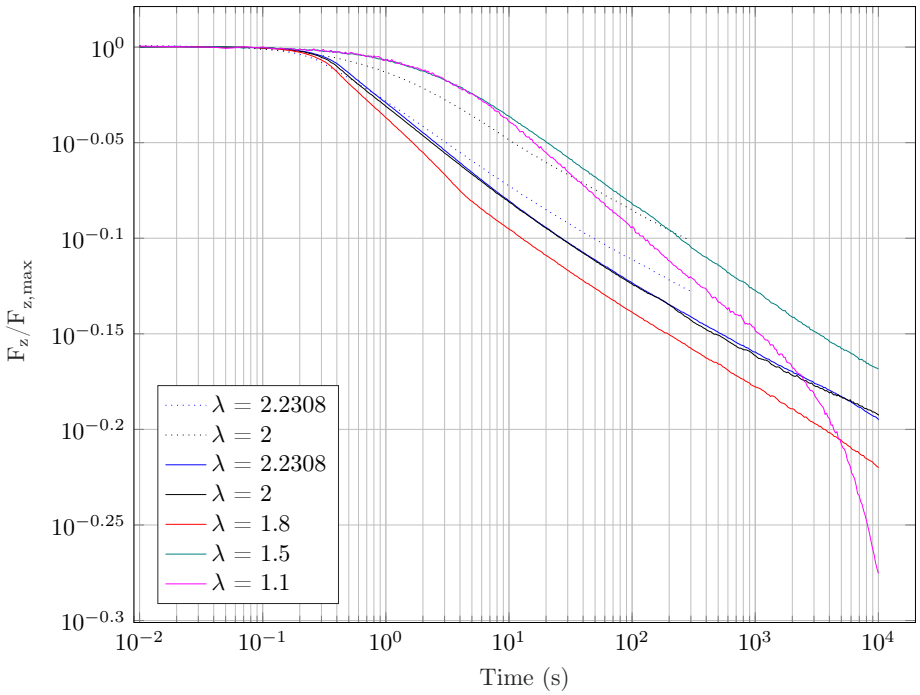

Figure 2.8: Normalised values for vertical force for relaxation tests on filled rubber for five different imposed strains at 24°C.

and $t = 2 \times 10^3$ s and suggest that we cannot precisely model this material with a simple Maxwell model. Three different behaviours can be extracted from this figure, and have been summarised in Table 2.5. The three higher stretch curves exhibit the same behaviour

whereas the lower stretch displays two distinct behaviours with a slower relaxation at first, which tends to increase around 10^3 s for the lower stretch at $\lambda = 1.1$.

λ_{max}	Slope break at		
	$t = 2 \times 10^{-1}$ s	$t = 2$ s	$t = 2 \times 10^3$ s
2.2308	Yes	Yes	No
2	Yes	Yes	No
1.8	Yes	Yes	No
1.5	No	Yes	No
1.1	No	Yes	Yes

Table 2.5: Relaxation curves properties summary.

2.2.2.3 Dynamic Mechanical Analysis

Methods Dynamic Mechanical Analysis (DMA) is an experimental technique used to characterise the extent of viscous and elastic responses of materials, by applying a strain or stress at controlled frequencies and analysing the strain or stress response to obtain the storage and loss moduli [66]. Cylindrical samples of 6 mm diameter and 10 mm height were tested on a MetraviB DMA+150 machine, as shown in Figure 2.9.

A compressive static strain of 10% was imposed with a 3% dynamic strain: the sample is enduring 7% to 13% compression strain while testing. During the test, the machine is displacement-controlled. The tests were run with a frequency sweep from 10^{-2} Hz to 10 Hz. The tests were conducted in a temperature-controlled environment, with a temperature set to 23.5°C.

Results DMA results are displayed in Figure 2.10.

The left plot shows the storage and loss moduli in the tested frequency range. There is one decade difference between storage and loss modulus for each frequency tested: the hyperelastic behaviour of the material is of higher importance than the viscoelastic behaviour of the material. In Figure 2.10, the right-hand side plot expresses the damping for the tested frequencies. The damping is not evolving much in this frequency range, and the observed values are consistent with classical observations in SBR material.

2.2.2.4 Cyclic uniaxial tension tests

Methods Six cyclic uniaxial tension tests were conducted at different strain rates.

Elastomers can exhibit additional dynamic phenomena when loaded periodically. Two main phenomena can be exhibited: Mullins effect [70] and Payne effect [75]. The Payne effect occurs at small strains and will not be considered here. Mullins effect consists of mechanical softening recorded upon the first stretch. This phenomenon occurs in carbon-black filled elastomers, as the first stretch damages the rubber matrix and the filler structure [32]. Cyclic tests were then conducted to assess the presence of Mullins effect. Two tests were conducted on 10×65 mm^{2}s SBR samples, with the same loading path of 10 cycles of loadings and unloadings with increasing strain at each cycle. The loading phases were conducted at a fixed strain rate of 0.01 s^{-1}.

Figure 2.9: DMA testing setup. On the left stands the MetraViB DMA+150 machine, a dynamic testing machine with 150 N stiffness.

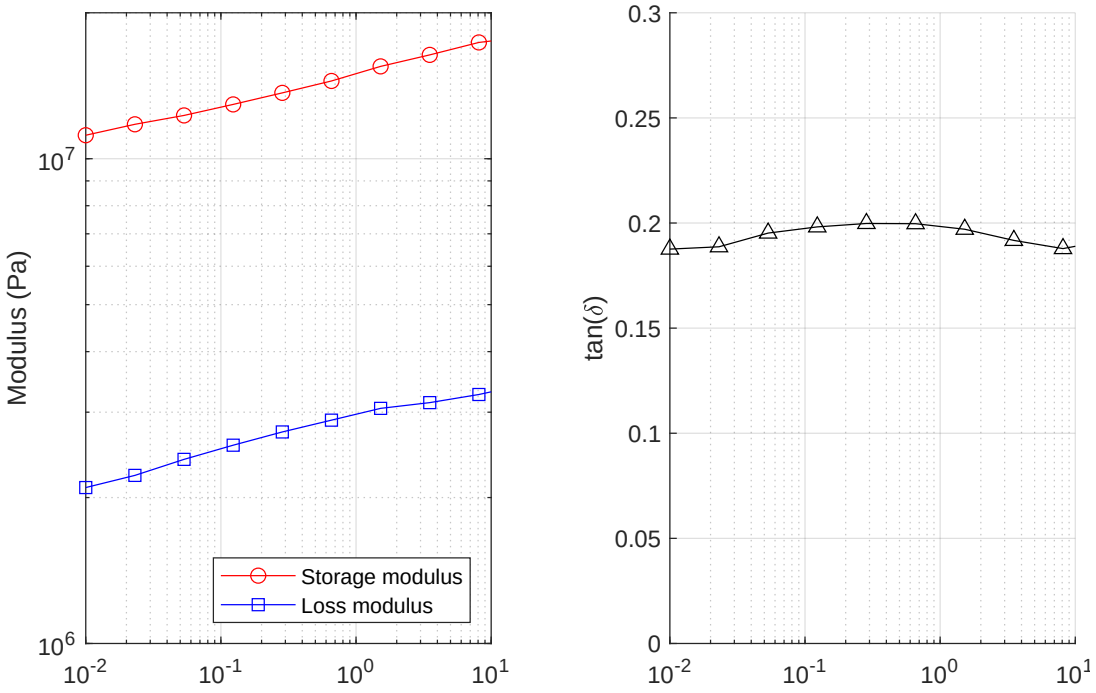

Figure 2.10: DMA results. The left plot expresses the storage and loss moduli for the tested frequencies and the right plot displays the damping for the tested frequencies.

Results The results are displayed in Figure 2.11.

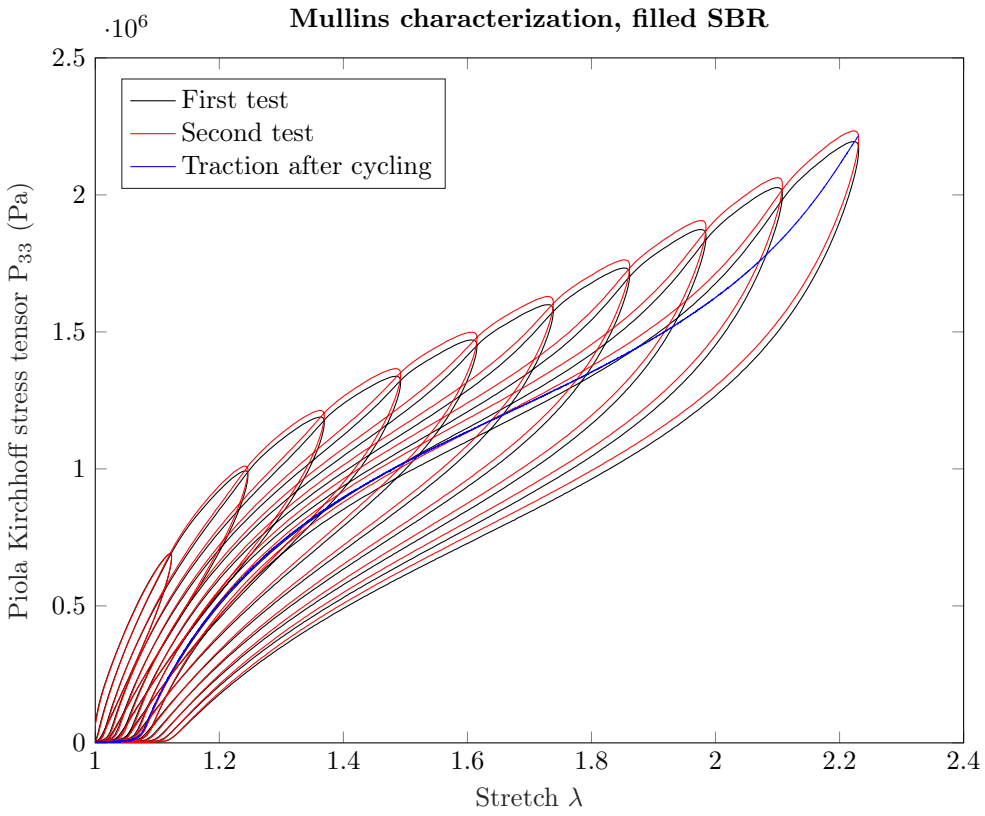

Figure 2.11: Cyclic tests on SBR sample.

The material exhibits clear signs of Mullins effect, characterised by the difference between stress responses induced by the same loading path, at strains already reached by the sample during previous cycles. This additional non-linear effect must be considered to develop our experimental tests. For example, multiaxial tests will tend to follow a loading path that ensures that the material is progressively loaded without unloading, to avoid the influence of Mullins effect.

Despite the availability of models to describe Mullins effect [16], as reviewed by Diani [31], the phenomenon was not investigated more, as we consider that using virgin material for each test and conducting progressive loading will ensure the absence of Mullins effect in experimental data.

2.2.3 Constitutive model for Finite Element simulations

Whereas this work has experimental purposes, it is classical to test and proof algorithms and methods with synthetic data before working with experimental data. A model was then needed to represent the carbon-black filled SBR during Finite Element simulations. The model fitting was made using the included tool of Abaqus CAE [30]. Models are fitted on uniaxial tension data presented in Figure 2.5, with $\dot{\epsilon} = 0.01$ s^{-1}. Several hyperelastic models were proposed and eleven of them are selected:

- Arruda-Boyce, successfully fitted,
- Marlow, unsuccessfully fitted,

- Mooney-Rivlin, successfully fitted only for uniaxial tension,
- neo-Hookean model, successfully fitted,
- Ogden models of first to fifth rank, successfully fitted by Abaqus but exhibiting fitted parameters that do not satisfy polyconvexity requirements,
- Van der Waals, unsuccessfully fitted,
- and Yeoh model, successfully fitted.

Yeoh model [102] is chosen to represent the material. Its strain energy density function is written:

$$W = C_{10}(I_1 - 3) + C_{20}(I_1 - 3)^2 + C_{30}(I_1 - 3)^3, \tag{2.9}$$

with $I_1 = \sum_{i=1}^{3} \lambda_i^2$ and C_{10}, C_{20} and C_{30} being the parameters of the model. The fitted parameters are presented in Table 2.6.

Parameters	C_{10}	C_{20}	C_{30}
Value (MPa)	0.937	-0.269	0.0598

Table 2.6: Parameters of the fitted Yeoh model.

The corresponding initial shear modulus is calculated as:

$$\mu_0 = 2C_{10} = 1.87 \times 10^6 \text{ Pa}. \tag{2.10}$$

2.2.4 Software and computation

This PhD project was achieved thanks to the following numerical tools:

- The codes for numerical procedures, Data-Driven Identification, experimental results analysis and figure plotting are written in Matlab, using Matlab R2020b version [62].
- Digital Image Correlation is run using the open-source software Ufreckles v2.0, developed by Réthoré [82].
- The Finite Element simulations are run with Abaqus CAE software developed by Dassault Systèmes, version 2019 [30]. Interfacing between Matlab and Abaqus has been written using Ufreckles tool to carry out numerical simulations. Abaqus was used using the recommendations of Elshorbagy [35].
- GMSH [39] and Paraview [51] were used for visualisation purposes and figure creation.

2.3 Conclusion

There are still some challenges in identifying the mechanical response of materials. In this study, material characterisation will be conducted for hyperelastic, isotropic and incompressible materials. A carbon-black-filled SBR is used for experimental purposes. Different tests have been conducted to characterise its behaviour. It exhibits some viscous

effects along with the Mullins effect. The multiaxial tests are designed to limit its viscous response and focus on hyperelasticity: the viscous behaviour will be neglected in multiaxial experimental tests. These tests are also designed to apply a progressive loading to avoid the Mullins effect.

Now that the tools for this study have been defined, we can focus on the successive objectives of this work.

- First, synthetic and physical multiaxial tests are presented.
- Test kinematics are extracted from these data, and will be studied using a visualisation tool.
- This tool will be extended to encapsulate the material's stress response.
- Finally, these studies will be used to build two applications: an identification method based on multiaxial tests and the DDI approach, and a reflection on the diversity of deformation modes encountered during our tests.

Part II

Exploring the mechanical response of materials

Chapter 3

Data acquisition

Our synthetic and experimental data are presented in this chapter.

Synthetic data is built using a third-order Ogden model fitted on Treloar's historical data. This "numerical material" is included in a FE model, constructed with a dogbone sample pierced with three holes. This sample is loaded in uniaxial tension with prescribed displacement, until a global stretch of 300%.

Experimental data is obtained using a test bench made of a hexapod device, force sensor and optical camera. The displacement field is measured using DIC. Carbon black-filled SBR membranes pierced with six holes are used. A complex test with a multiaxial loading path is applied with four different execution speeds.

Both synthetic and experimental data sets are formatted into Matlab structures and stored in a public repository for anyone interested in working with them. This public repository is accessible here [22].

Contents

Our synthetic and experimental data are presented in this chapter. The methods for obtaining those data are detailed. The deliverable of this chapter is a public repository for sharing the data used in this work. The datasets presented in this chapter present planar samples built with incompressible materials. The materials are under plane stress.

3.1 Synthetic data

Some numerical data built with Finite Elements simulation on Abaqus is used in this work to validate our methods. This data is similar to the one proposed in Dalémat PhD thesis [28], Chapter 3.

3.1.1 Sample design

The sample geometry used for synthetic data is shown in Figure 3.1. It consists of a dogbone sample of 200 mm height and 100 mm width pierced with three holes: two small holes of 25 mm diameter on the upper part and a larger one of 40 mm diameter near the bottom. The sample presents a vertical symmetry axis. The holes are placed to induce non-heterogeneous strain fields during stretching.

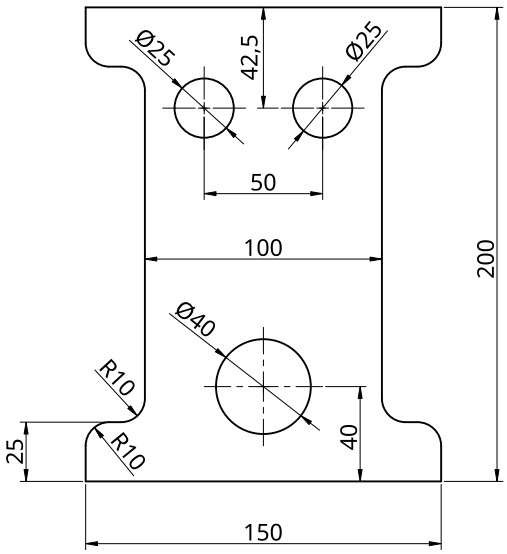

Figure 3.1: Sample shape and dimensions for synthetic data.

3.1.2 FE model

The Finite Element model is built in Abaqus CAE [30]. A third-order Ogden model is used to describe the material behaviour. The corresponding strain energy density is given in Eq. (1.6). Then, the principal Cauchy stress is:

$$\sigma_k = -q \; + \; \sum_{i=1}^{n} \; \mu_i \; \lambda_k^{\alpha_i} \qquad \forall \; k \in \{1,2,3\}. \tag{3.1}$$

The third-order Ogden model's parameters are the ones fitted by Ogden [71] on Treloar's data [90] and are presented in Table 3.1.

Remark: This model is chosen to build synthetic data and begin numerical investigations on a "synthetic material" prior to the first experiments on a test bench. This PhD was conducted during covid-19 pandemic and the experimental part was delayed due to pandemic restrictions.

Parameters	μ_1 (Pa)	μ_2 (Pa)	μ_3 (Pa)	α_1	α_2	α_3
Values	6.18×10^5	1.18×10^3	-9.81×10^3	1.3	5.0	-2.0

Table 3.1: Parameters of the third-order Ogden model used for synthetic data.

Note that the corresponding shear modulus is [45]:

$$\mu = \frac{1}{2} \sum_{i=1}^{3} \mu_i \, \alpha_i \approx 4.14 \times 10^5 \text{ Pa}. \tag{3.2}$$

For simulation, the sample is meshed with 3379 nodes and 6346 linear triangular finite elements.

3.1.3 Numerical experiment

The numerical computation consists of 20 loading steps. The 61 nodes of the lower sample boundary are fixed while the 61 nodes of the upper boundary of the sample undergo a linear prescribed vertical displacement while their x-axis coordinate is fixed. These boundary conditions are illustrated in Figure 3.2. The prescribed displacements of the upper boundary make the sample reach a 300% stretch ratio at the final loading step, with a prescribed vertical displacement of 400 mm.

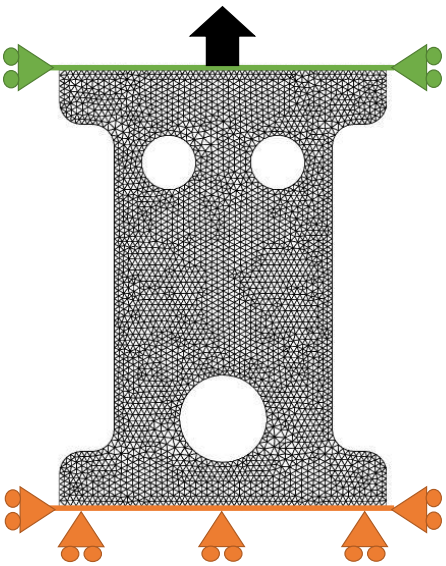

Figure 3.2: Mesh and boundary conditions for the FE model. The upper boundary (green) undergoes prescribed vertical displacement while the lower boundary (orange) is fixed.

3.1.4 References to the dataset through the manuscript

This dataset is referred to as “synthetic data” throughout the manuscript. For enhanced clarity, the icon presented in Figure 3.3 is placed on the side of figures representing data

related to this synthetic data.

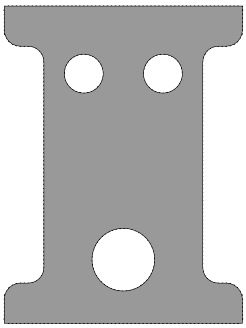

Figure 3.3: Icon representing the synthetic dataset in the manuscript.

Note that Section 6.2 only refers to this dataset.

3.2 Experimental data

This section presents the experimental tests run in this work. Four datasets are presented. The sample geometry and loading conditions are presented and the differences between the four tests are highlighted. The tests are run using the test bench described in Section 2.2.1.

3.2.1 Sample design

The sample is a 100×65 mm^2 carbon-black filled SBR membrane with 6 mm diameter cylindrical bulges to clamp in the machine's jaws. The samples are provided by Michelin. The samples are cut out from one of the SBR plates presented in Figure 2.4. Each sample is referred to as "ANR" followed by two numbers: the number of the 250×100 mm^2 plate it is extracted from and the number of the sample extracted from the same plate. The sample design is shown in Figure 3.4.

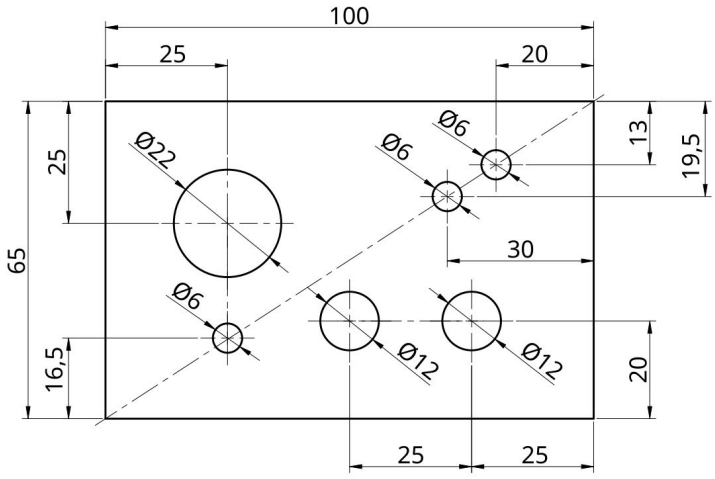

Figure 3.4: Sample used for experimental tests. The 65×100 mm^2 rectangular membrane of 1.6 mm thick is pierced with six holes: one of 22 mm diameter, two of 12 mm diameter and three with 6 mm diameter.

Six holes are pierced with circular cutting tools:

- a large 22 mm diameter hole in the top left part of the sample,
- two 12 mm diameter holes in the lower right part of the sample,
- and three 6 mm diameter holes located in the sample top right corner and bottom left corner.

The different sizes and positions of the holes have been chosen empirically. We create different-sized holes at close locations to intensify the heterogeneity in strain fields.

3.2.2 Experiments

The complex experiment designed for this work is made to use the three degrees of freedom accessible for a planar membrane under plane stress hypothesis. The next chapter illustrates the choice of loading path by characterising the kinematics of the tests. The test consists in 6 loading "steps", shown in Figure 3.5:

- the first step consists of a -20 mm vertical displacement of the moveable plate,
- the second step consists of a $+10$ mm horizontal displacement of the moveable plate,
- The third step consists of a vertical displacement and a rotation of the moveable plate along the sample orthogonal axis of 12°. Those movements are combined to make the sample rotate along its bottom right corner and guarantee it will not buckle.
- the fourth step consists in a -10 mm horizontal displacement of the moveable plate,
- The fifth step consists of a vertical displacement and a rotation of the moveable plate along the sample orthogonal axis of $-12°$. Those movements are combined to make the sample rotate along its bottom left corner and guarantee it will not buckle.
- The sixth and final step consists of a -10 mm horizontal displacement of the moveable plate.

Each displacement trajectory is a half-period sine function with a fixed average speed. The average speed is different for each test run.

3.2.3 Acquiring data: DIC

A speckle pattern is applied on the samples with white paint. Lights are added to the experimental setup to guarantee a correct range of grey levels in the images for the DIC process. An optical camera takes pictures of the sample at a fixed time interval during the test. The pictures are used to measure the displacement field using Digital Image Correlation. Each picture is made of 3000×6000 pixels.

The DIC procedure is performed with Ufreckles [82]. Two screenshots of the software are presented in Figure 3.6. The left-hand side picture presents a picture of the sample before DIC, and the right-hand side picture presents the strain magnitude after DIC computation. The strain field is here presented in the deformed configuration. The deformed configuration calculated with DIC matched the picture of the deformed sample which is visible in the background.

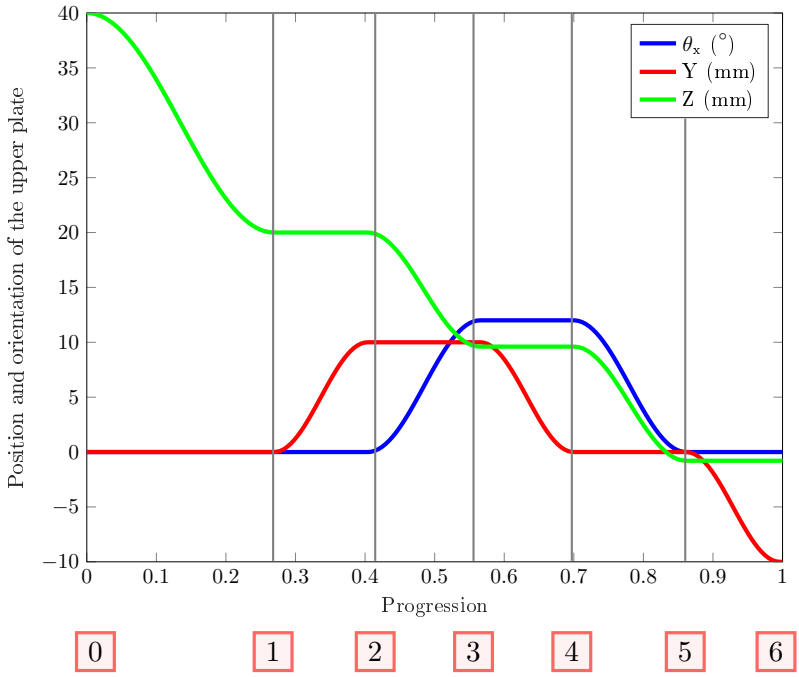

(a) Prescribed displacements of the upper plate of the hexapod device

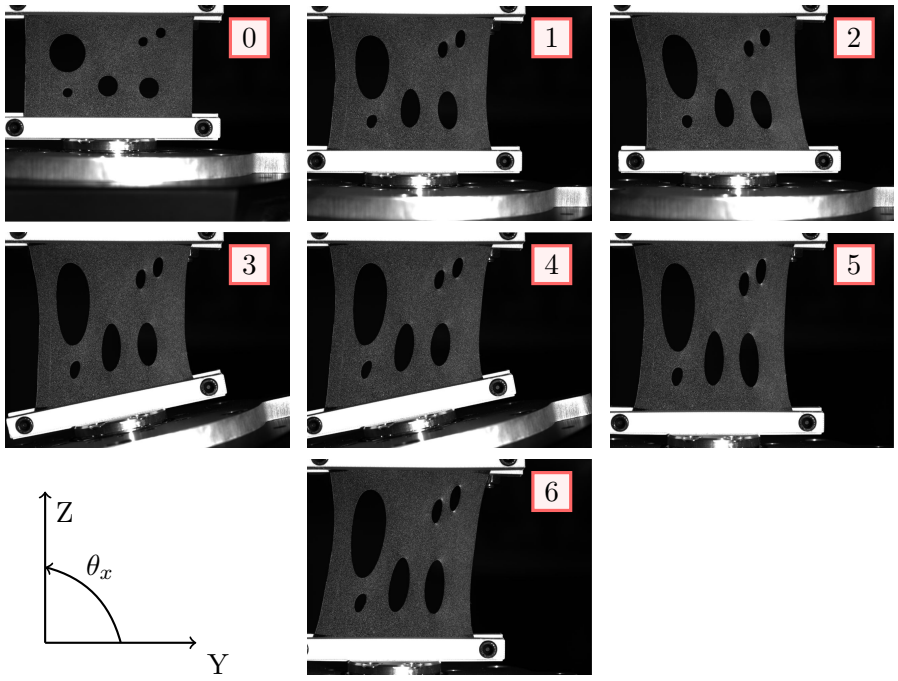

(b) Sample pictures during the experiment

Figure 3.5: Prescribed displacements and corresponding sample pictures. The corresponding time of the pictures is labeled by the numbers.

The DIC hardware parameters are presented in Table 3.2 according to International DIC Society [47].

FE-DIC is run with unstructured triangular mesh elements of 80 px. The parameters of the solver are presented in Table 3.3. DIC is run with sequential analysis and local normalisation. The predictions are explicit.

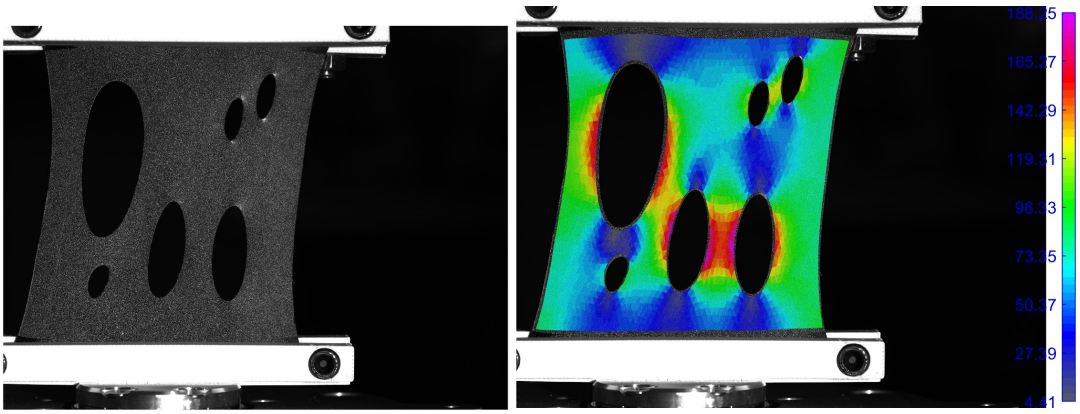

(a) Image of the deformed membrane at the end of the test, before DIC treatement

(b) Results visualisation after DIC treatement: strain magnitude displayed on top of the deformed image

Figure 3.6: Ufreckles software screenshots.

Camera	Vieworks VC-50MX-M30E0
Image Size	6000 × 8000 px^2
Lens	Tokina alx-i 100mm F2.8 FF Macro
Focal Lenght	100 mm
Aperture	100%
Field-of-View	130.7 × 174.2 mm^2
Image scale	45.9 px/mm
Stand-Off distance	460 mm
Patterning Technique	White spray paint
Pattern Feature Size	2 px

Table 3.2: DIC hardware parameters. Some parameters are specific to each dataset and are presented in Table 3.4.

Parameter	**Value**
Pixel size	1
Coarse graining	5
Convergence limit	10^{-3}
Maximal iteration	50
Pixel skip	1

Table 3.3: DIC solver parameters.

Smoothing has not been applied to the DIC results presented here. Some regularisation has been tested on the datasets, but the results were not satisfactory. More explanation on smoothing issues can be found in Appendix C.

3.2.4 The different datasets

Four experimental tests have been carried out. Each one is run on a new sample, which has never been deformed. Four different "global displacement speeds" are tested. These are symbolised by $\bar{V}$. This value corresponds to the average mobile plate displacement speed (mm.s^{-1}) and mobile plate rotation speed (°.s^{-1}). The four samples and their experimental parameters are presented in Table 3.4. Throughout the manuscript, these datasets as referred to as "experimental data". Each figure showing experimental data is accompanied by one icon representing the dataset that is shown. The icons are presented in Table 3.4 as well.

Sample	**ANR 2.1**	Icon
Number of frames	500	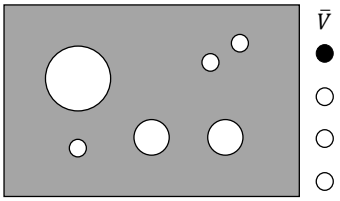
Number of Mesh Elements	4176	
Number of Mesh Nodes	2271	
Picture rate	10 Hz	
Exposure time	3000 μs	
$\bar{V}$	0.66 mm.s^{-1}	

Sample	**ANR 1.2**	Icon
Number of frames	500	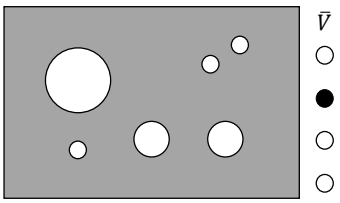
Number of Mesh Elements	3370	
Number of Mesh Nodes	1814	
Picture rate	1 Hz	
Exposure time	8000 μs	
$\bar{V}$	0.066 mm.s^{-1}	

Sample	**ANR 2.2**	Icon
Number of frames	1000	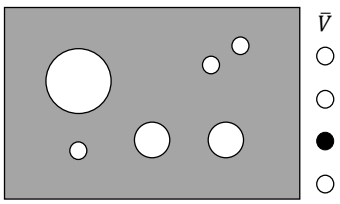
Number of Mesh Elements	3549	
Number of Mesh Nodes	1912	
Picture rate	0.66 Hz	
Exposure time	8000 μs	
$\bar{V}$	0.05 mm.s^{-1}	

Sample	**ANR 3.1**	Icon
Number of frames	1000	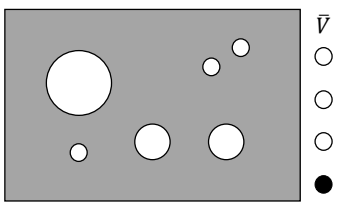
Number of Mesh Elements	3424	
Number of Mesh Nodes	1844	
Picture rate	0.2 Hz	
Exposure time	8000 μs	
$\bar{V}$	0.0066 mm.s^{-1}	

Table 3.4: FE-DIC parameters and associated icon for the four experiments.

3.3 Data structure and open access repository

This section describes the data structures stored in the open-access repository. This repository gathers ten data files, five in *.mat* format and five in *.ascii* format. They contain the data of the synthetic experiment and the four experimental tests described above.

3.3.1 Data structure

Each *.mat* data file contains a Matlab structure named *data*, containing 10 fields for the experimental tests data and 11 for the synthetic data. The name, dimensions and values of each field are described in Table 3.5. The data structure has a dimension of (number of frames $\times$ 1). Synthetic data are the only ones to display the field "sigma", which corresponds to the FE stress field computed by Abaqus.

Field name	**Corresponding feature**	**Dimension**
Connectivity	FE Connectivity matrix	Number of elements $\times$ 3
Dirichlet	Mesh nodes corresponding to Dirichlet boundary conditions	Variable
Force_sets	Mesh nodes where the net force is calculated	Number of boundary nodes $\times$ 1
F	Net force value, with two components	1×2
H	Hencky's logarithmic strain tensor components H_{11}, H_{22} and H_{12}	Number of elements $\times$ 3
Hencky_K1	Hencky's strain tensor invariants	Number of elements $\times$ 1
Hencky_K2		Number of elements $\times$ 1
Hencky_K3		Number of elements $\times$ 1
U	Nodes displacement	Number of nodes $\times$ 2
X	Initial nodes position	Number of nodes $\times$ 2
sigma	Cauchy's stress tensor components σ_{11}, σ_{22} and σ_{12}	Number of elements $\times$ 3

Table 3.5: Data structure fields.

3.3.2 Open access repository

The open access repository is available here [22]. It contains the data files in two different formats. The data structure is described above. The correspondence between experiments and data files is described in Table 3.6.

File name	Sample	Icon
dogbone_3holes_Ogden_synthetic_data.ascii	Synthetic dogbone	
dogbone_3holes_Ogden_synthetic_data.mat		
ANR_1-2_v0066_experimental_data.ascii	ANR 1.2	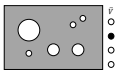
ANR_1-2_v0066_experimental_data.mat		
ANR_2-1_v066_experimental_data.ascii	ANR 2.1	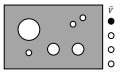
ANR_2-1_v066_experimental_data.mat		
ANR_2-2_v005_experimental_data.ascii	ANR 2.2	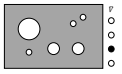
ANR_2-2_v005_experimental_data.mat		
ANR_3-1_v00066_experimental_data.ascii	ANR 3.1	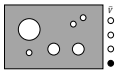
ANR_3-1_v00066_experimental_data.mat		

Table 3.6: File names and corresponding datasets. The file names are ranked in alphabetical order.

3.4 Conclusion

Five experiments have been presented in this chapter. They will be used in this manuscript. The first one is a synthetic experiment, built with Finite Element simulation and using a third-order Ogden model. The four other tests are conducted on an innovative test bench with a hexapod device. Non-homogenous loading paths are applied on pierced carbon-black-filled SBR planar membranes to generate a heterogeneous strain field. The displacement field is measured using DIC.

The five data sets corresponding to the five experiments presented above are stored in a public repository. Researchers may access it and use the data for research purposes. These data sets will be used as inputs for the DDI algorithm and to develop visual tools to describe test kinematics.

Chapter 4

A map to explore the kinematic response of materials

Multiaxial tests can be used for identification purposes. The major benefit of complex experimental tests is the ability to characterise the mechanical response of a material on a large diversity of deformation modes and prescribed loadings. To assess the diversity of the deformation modes encountered during the test, kinematics must be observed and described. The observation of kinematics is made through a graphical tool built with Hencky's logarithmic strain tensor invariants K_1, K_2 and K_3.

The kinematic map is a heatmap of (K_2, K_3) couples plotted on the (K_2, K_3) plane, K_2 indicating the deformation magnitude and K_3 the deformation mode. This tool seeks to provide a visual representation of the various deformations experienced by the material throughout the test, and their distribution in terms of modes and magnitudes. The kinematic map is built for synthetic and experimental data. The synthetic data set built with a perforated membrane undergoing linear axial displacement presents a majority of points exhibiting uniaxial tension deformation mode. However, the experimental tests run with hexapod device with varying imposed displacements exhibit a more distributed kinematic map, enhancing their interest for identification purposes.

By graphically illustrating the complex kinematic behaviour, researchers and practitioners can gain a deeper understanding of the material's response to applied forces and its resulting deformation patterns. This graphical tool can facilitate the analysis and interpretation of test data, leading to improved identification techniques and enhanced comprehension of material behaviour under different loading conditions.

Contents

4.1 Pre-requisites

Kinematics has been described above, and physical features were defined for Continuum Mechanics. This section presents the features used in this work to describe the kinematics of the continuum, and especially the strain tensors. The choice of strain tensor is discussed, and the strain tensor components from synthetic and experimental data are observed.

4.1.1 How to observe the kinematics of an experiment and why

The goal of this chapter is to develop a graphical tool able to fully describe the kinematics of an experiment, in a way that is usable for identification purposes. An experiment mostly stands for measuring and characterising the mechanical response of the material under given loading conditions. The mechanical response of the material consists of the relationship between strain and stress. To describe this mechanical response, the observable features are measured during the experiment. For a planar membrane under plane stress hypothesis, the displacement of the surface of the membrane is observable and measurable through Digital Image Correlation, as illustrated in Figure 4.1. Net forces can be measured by force sensor. This measure is not direct: the forces are measured through the displacement of the mechanical part of the sensor, which undergoes deformation.

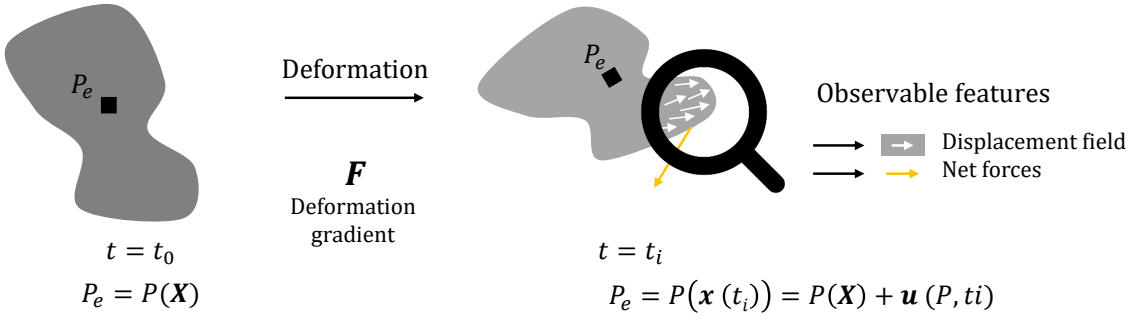

Figure 4.1: Observable features during an experiment. The magnifying glass represents the measuring instruments of physical features during a body deformation.

The observed displacements allow the strain calculation and observation throughout test. However, the stresses are not observable, and the net forces measured do not give sufficient data to obtain the stresses inside the sample. The complete characterisation of material response relies on the missing link between strains and stresses. Experimental cases with strong hypotheses can lead to the direct calculation of stresses, such as the homogeneous test presented in Chapter 2.

Before getting to stresses, the complete knowledge of the kinematics during a given experiment allows to quantify the diversity of the deformation undergone by the sample during this experiment. It also characterises the diversity and magnitude of deformation modes prescribed to the sample during the experiment. The more diverse the deformation modes and prescribed loading are, the more complete and relevant for identification a test is. This is the main reason to develop specific tools to observe and describe the kinematics during a multiaxial test.

4.1.2 Features for finite strain

Different strain tensors were presented in Chapter 1. The present work focuses on soft materials. Thus, the experiments conducted here correspond to finite strain situations. Hencky's logarithmic strain tensor can be used to describe finite strain situations. It is usually used for large strain kinematics description [23], elastoplasticity description for large strains [36] or integrating elastomer's incompressible behaviour in Finite Elements calculations [1]. This strain tensor is chosen for kinematics description in this work, as advised for finite strain Data-Driven Identification according to Dalémat [28]. Hencky's strain tensor $\boldsymbol{H}$, is derived from deformation gradient $\boldsymbol{F}$ polar decomposition:

$$\boldsymbol{H} = \ln(\boldsymbol{V}) \text{ with } \boldsymbol{F} = \boldsymbol{V}\boldsymbol{R}. \tag{4.1}$$

$\boldsymbol{H}$ is also called true strain tensor because it is the large strain extension of $\boldsymbol{\epsilon}$, the infinitesimal strain tensor. For example, in the case of a large strain uniaxial tension test, the strain calculated by incrementing small strain is:

$$\int \mathrm{d}\epsilon = \int_L^l \frac{\mathrm{dx}}{x} = \ln\left(\frac{l}{L}\right) = \ln(\lambda), \tag{4.2}$$

with L the initial length of the sample gauge, and l the length after deformation. We note $\mathrm{d}\epsilon$ an infinitesimal strain increment. So, the eigenvalues of Hencky's strain tensor are the natural logarithm of the principal stretches, which are the eigenvalues of $\boldsymbol{V}$.

Hencky's strain tensor is adapted to finite strain and hyperelastic materials. It can be used to build hyperelastic models, as proposed by Bruhns *et al.* [13]. It is rarely used for writing stress-strain relations, and its time derivative expressions can be found in Xiao and Chen's work [100].

4.1.3 Observing the strain field

Once the strain tensor is chosen and defined, the kinematics of the experiments can be discussed. First, Hencky's tensor components are represented using bar histograms. Each following figure represents three of them: $\boldsymbol{H}_{11}$, $\boldsymbol{H}_{22}$ and $\boldsymbol{H}_{12}$. Indeed, with the plane stress assumption, four of the nine components of the strain tensor are equal to zero and are not represented. The diagonal component $\boldsymbol{H}_{33}$ is calculated using the measured strain components and the incompressibility hypothesis. Moreover, $\boldsymbol{V}$ is symmetrical by property of the polar decomposition, and so is $\boldsymbol{H}$.

Figure 4.2 presents the bar histogram visualisation of Hencky's strain field for the synthetic data presented in Chapter 3.

Those histograms are constructed by considering the full dataset including all mesh elements at each time step. The bar width is fixed and the four histograms of the Figure share axis to make their comparison easy. Each histogram represents the distribution if one tensor component through the elements and the test. It shows that diagonal component $\boldsymbol{H}_{11}$ presents mostly negative values. $\boldsymbol{H}_{22}$ is mostly positive, and reaches higher values: it corresponds to the strain along the loading direction. The only non-diagonal component presented here, $\boldsymbol{H}_{12}$, displays a majority of near-zero values, and both negative and positive values. The large number of null values of this component indicates that deformation occurs within the principal directions.

Figure 4.3 presents the bar histogram visualisation of Hencky's strain field for the experimental data presented in Chapter 3.

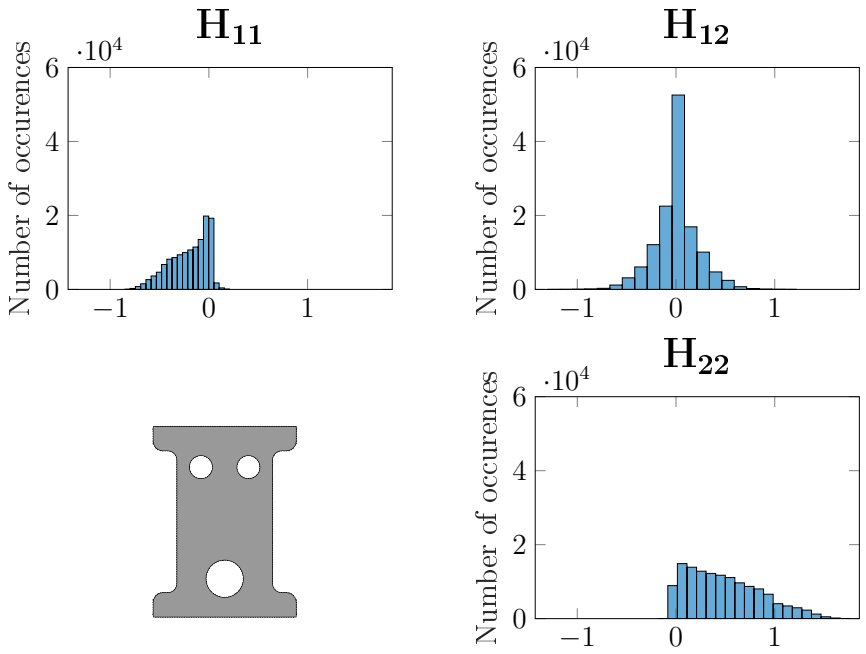

Figure 4.2: Bar histogram visualisation for Hencky's strain tensor components of synthetic data.

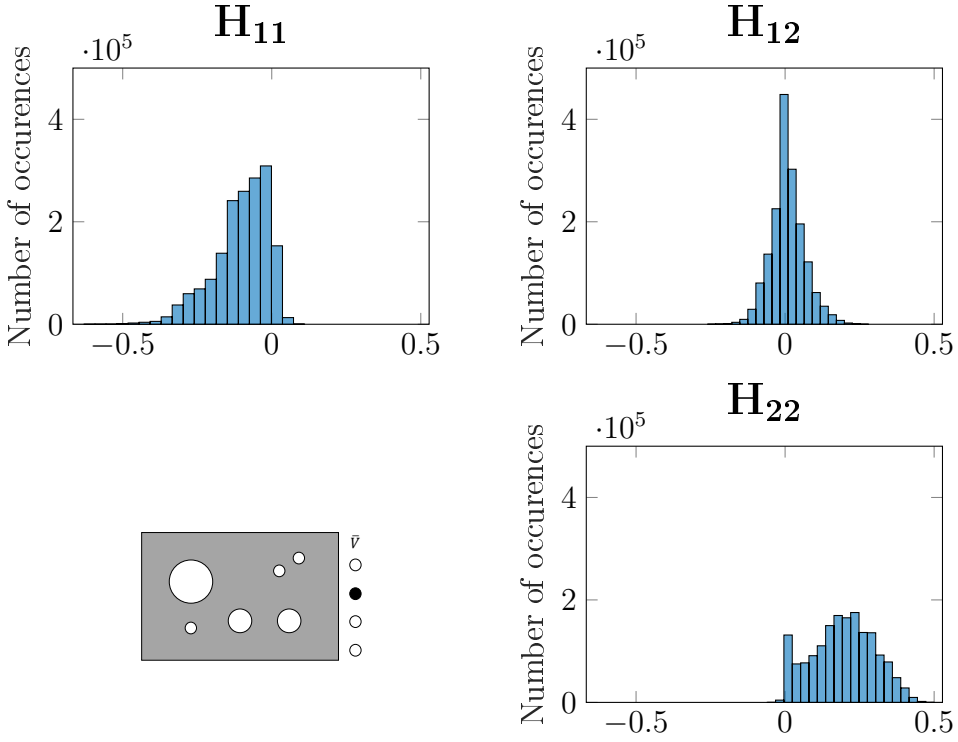

Figure 4.3: Bar histogram visualisation for Hencky's strain tensor components of experimental data.

It shows that diagonal component $\boldsymbol{H}_{11}$ presents mostly negative values. $\boldsymbol{H}_{22}$ is mostly positive. The three diagonal components display very different distributions. The

only non-diagonal component presented here, $\boldsymbol{H}_{12}$, displays a majority of near-zero values, and both negative and positive values. It is difficult to gather information about the deformation modes endured by the material during the experiment using this representation.

Finally, this representation with bar histograms shows the distribution of each tensor component value during the experiment. However, this representation misses the link between the components themselves: are the maximal values of $\boldsymbol{H}_{22}$ related to the zero values of $\boldsymbol{H}_{12}$? Are they related to the minimal values of $\boldsymbol{H}_{12}$? Those questions can be answered by using a different representation of kinematics, involving quantities which summarise the strain tensor to characterise what is endured by the material. The choice is placed upon invariants which ensure the representation does not change with the coordinate system. This is the goal of the following section.

4.2 Building a map to explore the kinematics in materials

The visual representation of a kinematic field is a challenge due to the dimensions of the strain fields. This section aims to build a 2D-map summarising the kinematics of a given experimental test, step by step. Invariants of the logarithmic strain tensor are considered for this purpose. They are first presented below.

4.2.1 Invariants to characterise strain states

4.2.1.1 Definition

Criscione *et al.* have defined Hencky's logarithmic strain tensor invariants [26]. These three invariants are:

$$\begin{cases} K_1 = \mathrm{tr}(\boldsymbol{H}) \\ K_2 = \sqrt{\mathrm{dev}(\boldsymbol{H}) : \mathrm{dev}(\mathbf{H})} \\ K_3 = \dfrac{3\sqrt{6}}{{K_2}^3}\det(\mathrm{dev}(\boldsymbol{H})), \end{cases} \tag{4.3}$$

with

$$\mathrm{dev}(\bullet) = \bullet - \mathrm{tr}\left(\frac{(\bullet)}{3}\right)\boldsymbol{I}, \tag{4.4}$$

$\boldsymbol{I}$ being the identity tensor and $\boldsymbol{H}$ Hencky's strain tensor. The invariants can be written using the principal stretches $(\lambda_1, \lambda_2, \lambda_3)$:

$$\begin{cases} K_1 = \ln(\lambda_1\lambda_2\lambda_3) \\ K_2 = \sqrt{(\ln\lambda_1 - \frac{1}{3}K_1)^2 + (\ln\lambda_2 - \frac{1}{3}K_1)^2 + (\ln\lambda_3 - \frac{1}{3}K_1)^2} \\ K_3 = \dfrac{3\sqrt{6}}{{K_2}^3}(\ln\lambda_1 - \frac{1}{3}K_1)(\ln\lambda_2 - \frac{1}{3}K_1)(\ln\lambda_3 - \frac{1}{3}K_1). \end{cases} . \tag{4.5}$$

These three quantities summarises the logarithmic strain tensor with three distinct characteristics:

- K_1 is a real number characterising the "amount of dilatation", K_1 is equal to zero for incompressible materials, and therefore will not be further considered in this study,

- K_2 is a real positive number characterising the "magnitude of distorsion" of material points, defining a norm for the Hencky's strain tensor,
- K_3 is a real number in the range $[-1; 1]$, characterising the "mode or type of distorsion" of material points. It has three noteworthy values, indicating particular deformation modes. They are summarised in Table 4.1.

K_3	**Type of loading**
1	Uniaxial Tension or Equibiaxial Compression
0	Planar Tension
-1	Equibiaxial Tension or uniaxial compression

Table 4.1: K_3 values and corresponding loading.

The Hencky's logarithmic strain tensor invariants have already been used to characterise strain magnitude and deformation mode in a Data-Driven context by Platzer [80]. Her work on dense databases sampling derives from Kunc and Fritzen sampling method [52]. The authors developped a strain magnitude measure called the "deviatoric amplitude" and a direction vector expressing the deformation mode. The role of these two variables is equivalent to the (K_2, K_3) pair.

Remark 1: *Hencky's logarithmic strain tensors invariants have been used to characterise the strain undergone by rubber during cyclic tension-torsion tests for fatigue testing [56][55].*

Remark 2: *Hencky's strain tensor invariants posess stress counterparts used to describe stress states in the study of elastoplastic behaviours [12]. These invariants are described in Appendix B.*

4.2.1.2 Invariants visualisation

Once the invariants are calculated for each mesh element at each time step, they can be represented on the deformed sample. Figure 4.4 presents the invariants fields on the deformed synthetic sample, at its maximal stretch at last time step.

The deformed mesh exhibits a large diversity of deformation magnitudes, shown in Figure 4.4 (a). The colourbar expresses the deformation magnitude using Hencky's logarithmic strain tensor invariant K_2, which varies from 0 to more than 2 at this time step. The highest K_2 values are located around the sample's holes, and the lowest ones in the sample's larger top and bottom areas. Figure 4.4 (b) displays the deformation modes at this time step on the deformed mesh using Hencky's logarithmic strain tensor invariant K_3. The colourbar represents the different groups of "deformation modes", the red colour expressing mostly uniaxial tension, the cream one is for planar tension and the dark blue one for equibiaxial tension. Any intermediate colour expresses also an intermediate mode. The sample exhibits mostly uniaxial tension deformation mode, and different ones only at the tom and bottom of the sample, which are the less deformed zones. Figure 4.5 presents the invariants fields for experimental data, at the last time step of the experiment.

The deformation magnitude exhibited by Figure 4.5 (a) presents some diversity, with a range of Hencky's logarithmic strain tensor invariant K_2 ranging from 0 to 1.1. The

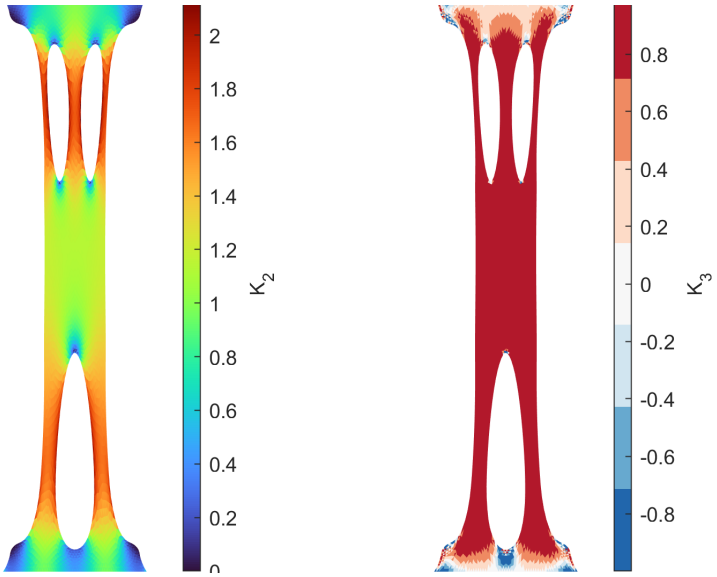

(a) K_2 field (b) K_3 field

Figure 4.4: Invariants fields plotted on the deformed mesh for synthetic experiment at its last time step.

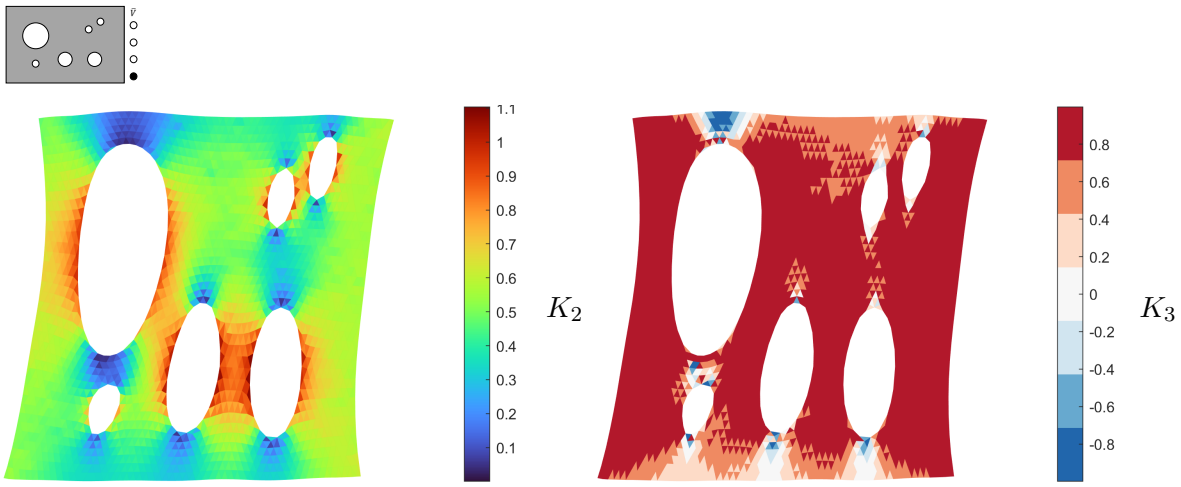

(a) K_2 field (b) K_3 field

Figure 4.5: Invariants fields plotted on the deformed mesh for experimental data at its last time step.

holes boundaries are exhibiting the highest deformation magnitudes on their left and right sides, represented in red, but also the lowest deformation magnitudes on their upper and lower border, represented in dark blue. Various deformation magnitudes are exhibited away from the holes and are represented by varying colours from light blue to orange. The deformation modes, presented in Figure 4.5 (b) shows that the major part of the sample is exhibiting mostly uniaxial tension deformation mode at this time step: the deformed mesh is mostly red. Other deformation modes are exhibited in low deformation magnitudes areas, such as on top or underneath holes.

4.2.2 General principle for building the map

The kinematics map is built using Hencky's logarithmic strain tensor invariants K_2 and K_3, respectively representing the "magnitude of distorsion" and the "mode of distorsion" underwent by the material. The construction of the map is described in Figure 4.6.

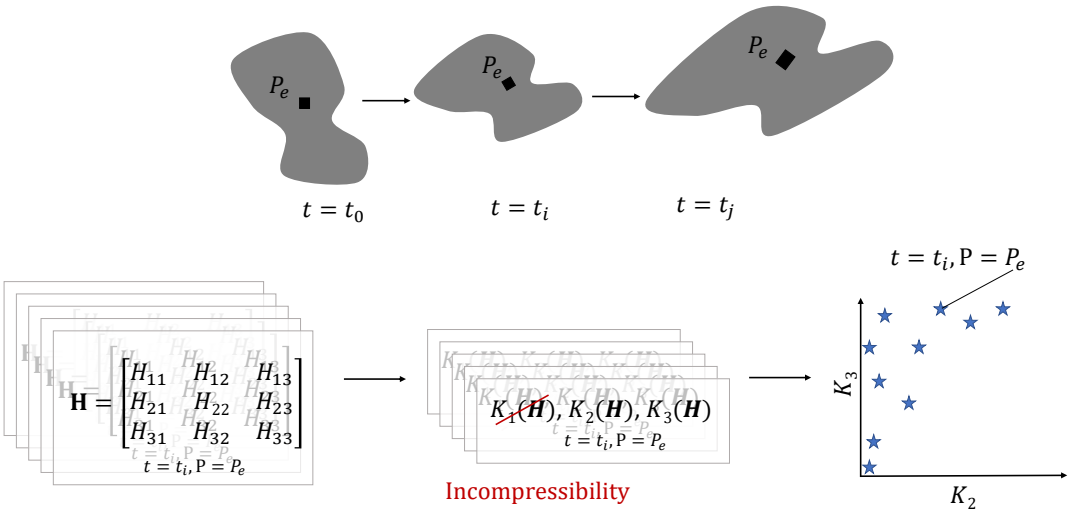

Figure 4.6: General principle of the kinematics map.

The map built-up involves the same process for synthetic and experimental data. The samples are discretised: synthetic data is built with Finite Elements, and the experimental strain field is measured using FE-DIC. The Hencky's logarithmic strain tensor is calculated for each mesh element of the sample at each time step, as shown on the bottom left part of Figure 4.6. Then Hencky's tensor invariants are calculated for each Hencky's strain tensor. K_1 is represented crossed out by a red line because of the incompressibility of the material. This feature is always equal to zero and is not represented in the kinematics map. Once the (K_2, K_3) couples being calculated for each mech element at each time step, they are plotted in the (K_2, K_3) plane, to produce the "kinematic map". An example of such a map is presented in the bottom right part of Figure 4.6. The map in Figure 4.7 is built using Treloar's data [90], representing experimental data for vulcanized sulfut-filled rubber.

It exhibits around fifty points, arranged in three horizontal lines of constant K_3 values, corresponding to the three noticeable values of K_3. Uniaxial tension data from Treloar's experiments is located on the horizontal line corresponding to $K_3 = 1$, the planar tension data on the $K_3 = 0$ line and the equibiaxial tension data on the $K_3 = -1$ line. Treloar's data kinematic map is easily readable because of the scarcity of points.

However, with large experimental databases, such a plot can be difficult to describe if points overlap others, making their density difficult to read. This phenomenon is examplified in Figure 4.8, which presents the (K_2, K_3) couples for synthetic data.

In this figure, the point cloud densely covers the K_3 axis, and spreads horizontally towards high K_2 values. However, the density of points and their overall distribution is not easily visible. This situation triggers the necessity of improving the map to enhance its readability. The process of colour-mapping the density of points is explained in Figure 4.9.

a) the (K_2, K_3) couples are plotted in the (K_2, K_3) plane,

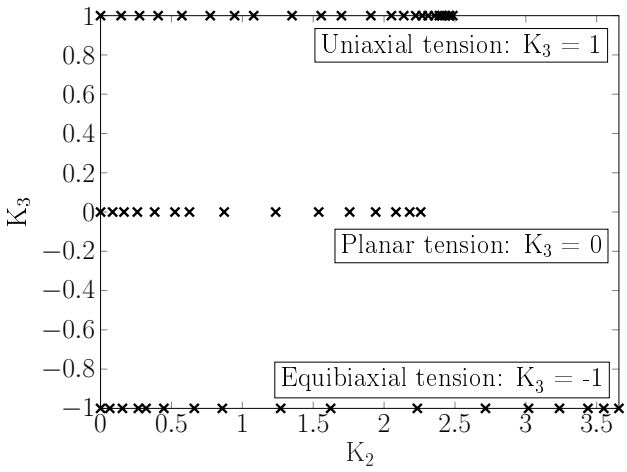

Figure 4.7: Kinematic map for Treloar's data [90].

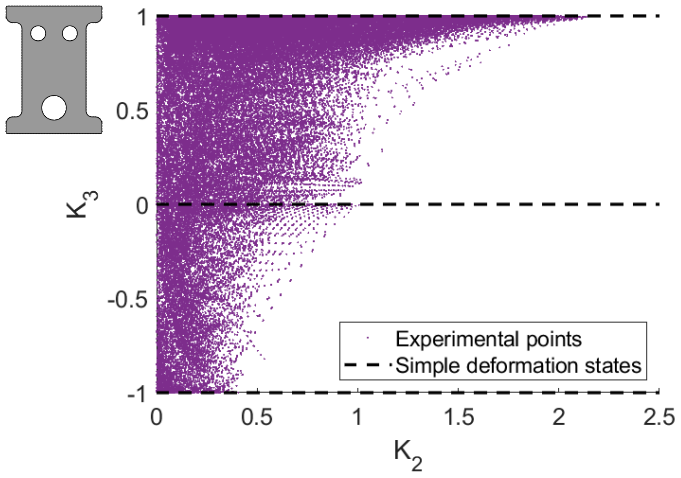

Figure 4.8: Kinematic map for synthetic data. The dotted lines represent the simple deformation states zones.

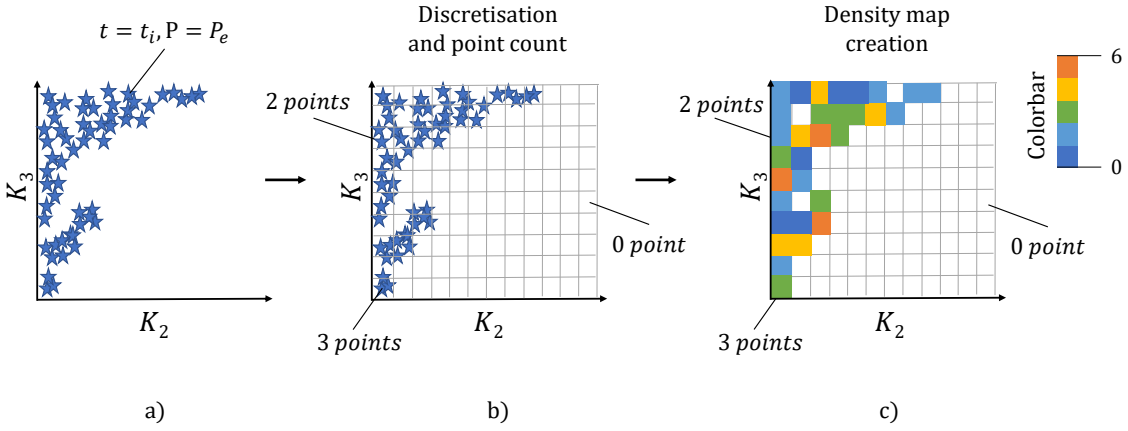

Figure 4.9: Improvement of the final kinematic map.

b) the plane presented above is discretised, with 0.04 intervals in both K_2 and K_3 axis. The (K_2, K_3) points are counted in each parcel of the plane,

c) the obtained number is divided by the total number of points represented on the map. A natural logarithm is applied for enhanced readability. Each parcel of plan is coloured according to the calculated point proportion it contains. The final map represents the density of points on the (K_2, K_3) plane for a given experiment.

4.2.3 Kinematic maps for experiments on planar membranes

In the following, kinematic maps are plotted for synthetic and experimental tests described in Chapter 3. Figure 4.10 presents the kinematics map for synthetic experiment. The density point cloud spreads along the K_3 axis, meaning that all deformation modes are reached during the experiment, from uniaxial tension to equibiaxial tension through planar tension, and mixed modes. However, the colourmap indicates a very dense zone located along the horizontal top line of the graph, corresponding to $K_3 = 1$. This zone corresponds to mesh elements undergoing Uniaxial Tension during the experiment. The colourbar shows that the uniaxial tension zone gathers the majority of points, the yellow and green zones representing up to two decades fewer points than the red zones. This can be due to the choice of loading: during this experiment, the loading consists of a simple vertical displacement, along the principal axis of the sample. While the sample is pierced with holes, the general shape and the loading seem to submit the elements to uniaxial tension. This kinematic map and its analysis did influence the loading path choice for the hexapod experiments. The chosen loading path encompasses different boundary displacements to generate more deformation states diversity, as seen in Chapter 3.

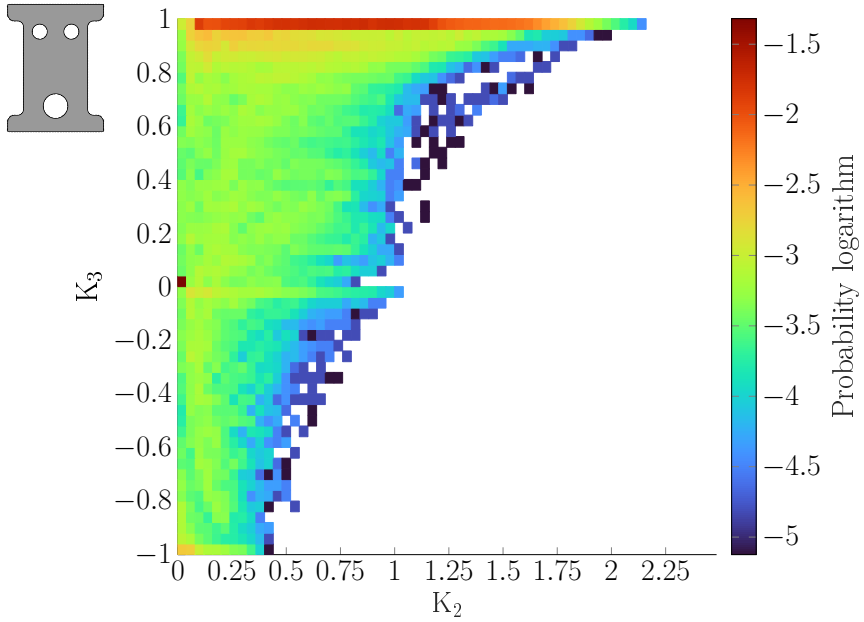

Figure 4.10: Kinematic map for synthetic data experiment. The map represents the point density of the (K_2, K_3) plane on which is plotted (K_2, K_3) couples for every mesh element at each time step.

Figure 4.11 presents the four kinematic maps of the four experimental tests presented in Chapter 3. On those maps, points spread along the K_3 axis, representing all the possible deformation modes. Deformation magnitude spreads from zero to $K_2 = 1.1$. The four maps present a similar shape of dense point clouds, represented by the yellow to green

areas, and a varying dispersion of low-density areas, represented in blue. The slower the speed, the larger the area covered by the point cloud is on this map. The largest density is reached for intermediate K_2 values (around 0.3 to 0.6) in uniaxial tension ($K_3 = 1$). The difference in probability logarithm between the densest area and the rest of the map is less than one decade, meaning that the points are more evenly spread on the plane than for the synthetic experiment. It is due to the use of the hexapod device, allowing multiple directions of loading. The blue areas stand for small numbers of points and the dispersion observed at lower speeds can be neglected for kinematical comparison between the four experiments.

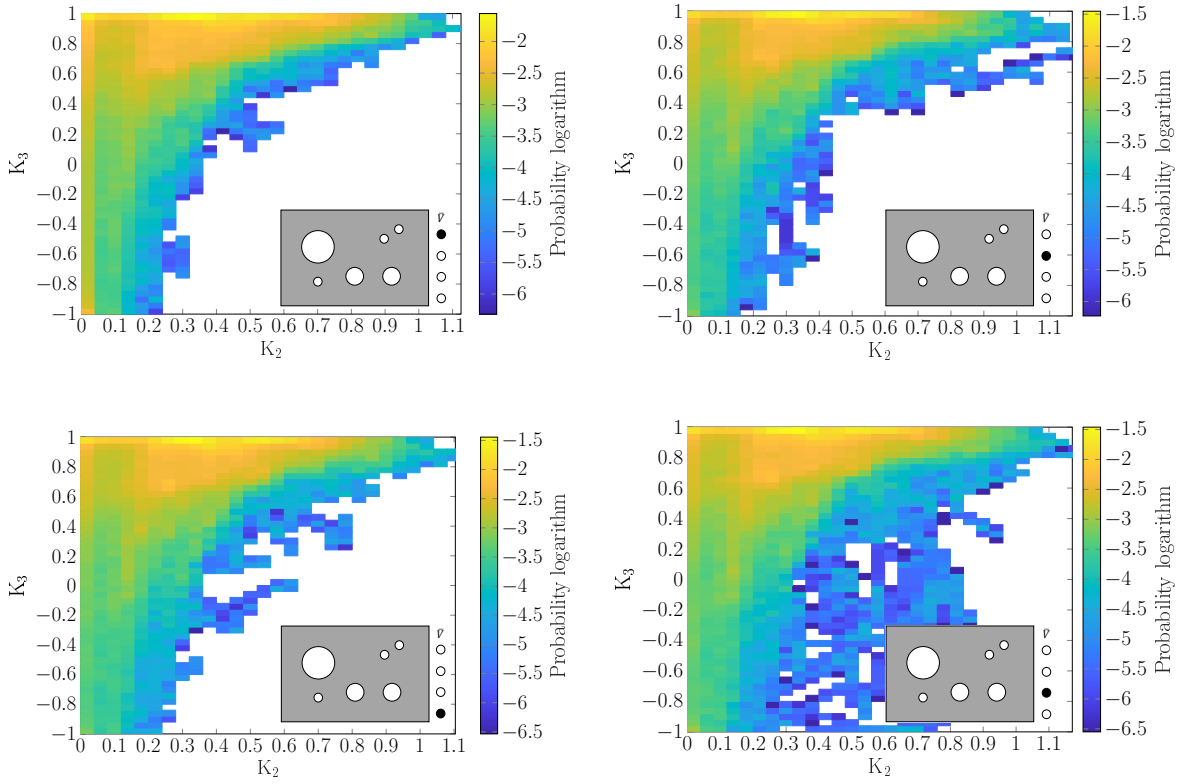

Figure 4.11: Experimental kinematics map for four experiments conducted with the same sample geometry and loading conditions, but at different loading speeds. The map represents the point density of the (K_2, K_3) plane on which is plotted (K_2, K_3) couple for every mesh element at each time step.

This representation helps to characterise the amount of deformation modes and magnitudes encountered by the material during the experiment. However, the representation is dependant of the chosen plane discretisation. Using larger "bins", because our representation is not different from a two-entries histogram, could give a false-sense of plane coverage, by increasing the plane surface covered by the coloured bins, whereas chosing smaller bins could help spot the denser areas and their characteristics. Reducing the size of the bins could, if made extreme, bypass the major interest of the visual tool by resulting of a map with bins so small they just mimic the point cloud representation and do not allow to spot the zones density properly.

4.3 Conclusion

Characterising the strains and kinematics underwent by the material during a complex test allows to assess the diversity of deformation modes and intensities. Experimental tests with several deformation modes are more suited for full-field measurement-based identification purposes. They cover a wider range of strain the material can undergo in service, and promise better identification of models.

Here, an original map has been built to explore the kinematics of multiaxial tests. This map allows to observe the diversity of deformation modes and their distribution in the (K_2, K_3) plane.

Overall, stretching the material in a unique direction seems to generate uniaxial tension deformation mode for the majority of points, whereas multiaxial experiments based on diverse loading directions generate more distributed kinematics maps, even if uniaxial tension mode remains highly represented. Specific deformation modes seem difficult to target when looking at large strain magnitudes, at least with the proposed experimental setup. That is the case of equibiaxial tension for example. The kinematics map allows to choose tests with evenly distributed maps, which will enhance the representativity of the data for identification purposes.

More investigations could be made with this tool, for example by looking at the evolution of the kinematic map during the experiment to assess if the uniaxial tension deformation mode is “preferred” by the material when the deformation magnitude rises.

Chapter 5

Exploring stress and strain energy density fields

The Data-Driven Identification method calculates the experimental stress field without using a constitutive model. This method is based on clustering and relies on the mechanical equilibrium of the structure to provide an admissible stress field. DDI is applied to synthetic and experimental data. The resulting stress fields are observed using bar histogram representation. However, this representation is not suitable to be added to the kinematical map built in Chapter 4 to represent the complete mechanical response of the material.

Strain energy density represents the stress field weighted by the kinematic field. It is a feature encompassing strain and stress into a scalar value. Strain energy density is chosen to represent the mechanical response of materials in the material response map.

The new map encompasses both kinematics and stresses, within a single characteristic graph. By incorporating stress information alongside kinematic data, this enriched graphical tool can provide an overview of the material's behaviour under different loading conditions, enabling a deeper understanding of its mechanical response. This approach facilitates the exploration of stress patterns and their relationships with kinematic features, ultimately contributing to the advancement of data-driven material modelling and characterisation techniques.

Contents

The previous chapters of this document highlighted the variety of existing models for solids and the complexity of identification processes. Modelling inherits an intrinsic modelling error. To avoid this constitutive error and with the help of numerical processes, research teams have developed new identification processes based on discrete databases extracted from experimental data sampling of mechanical behaviour, and called Data-driven methods. Those methods are based on a different representation of materials, constitutive laws being replaced by rich and large databases. This representation is well adapted to new acquisition methods, such as Digital Image Correlation (DIC), and complex experiments which generate large and rich data. In this section, Data-Driven Identification (DDI) and its developments are described and used to measure stress fields from a complex experiment.

Note: Plenty of Data-Driven methods have been developed. The Data-Driven methods described here rely on the Data-Driven paradigm written by Kirchdoerfer and Ortiz in 2016 [50]. The other existing Data-Driven method can be non-parametric methods, as seen in Montans et al. [69]; or involve Singular Value Decomposition and Gaussian processes [96] but they can also be based on an alignment assumption [14]. Data-adaptative methods can also be cited as data-based methods for identification, such as Wiesheier et al. [97]. Other manifold learning methods have been introduced, such as "What-You-Prescribed-Is-What-You-Get", or WYPIWYG, introduced by Latorre and Montans [54], which process has been adapter to hyperelasticity by Crespo et al. [25].

5.1 Using DDI to measure stress fields

The Data-Driven Identification method is a powerful algorithm developped in 2018 by Leygue *et al.* allowing the calculation of balanced stress fields without any constitutive law [57]. This section is dedicated to the description of the method principle and its adaptations to hyperelasticity. The general definitions and equations are writen for a three-dimensional problem. The algorithm principle is schemed using one-dimensionnal features for the sake of clarity.

5.1.1 Principle

The Data-Driven Computational Mechanics paradigm formulated by Kirchdoerfer and Ortiz [50] proposes to bypass the "empirical material modelling step" and solve the mechanical problem without constitutive equations. The mechanical response of the material is represented by a discrete database of points instead of a model equation. In 2018, Leygue *et al.* incorporated this paradigm within a sequential looping algorithm to build Data-Driven Identification (DDI) [57]. Dalémat then adapted this framework to experimental data, with wise adaptations for large strains, experimental boundaries and missing data [29]. The general framework is presented in the following section, then adaptations for our experimental framework are presented.

5.1.1.1 Definitions and parameters

To begin with, some terms and notations are defined:

- The **constitutive space** is a multi-dimensional space where the material behaviour will be approximated. For elastic materials, the constitutive space is a 9×9 space $(\boldsymbol{\epsilon}, \boldsymbol{\sigma})$ where mechanical states and material states can be defined. The constitutive space can be expanded for inelastic problems, including a history variable for example.

- The $\mathbb{C}$**-norm** is defined on the constitutive space using the DDI metric $\mathbb{C}$ and $(\boldsymbol{\epsilon}, \boldsymbol{\sigma})$ an element of the constitutive space:

$$\| (\boldsymbol{\epsilon}, \boldsymbol{\sigma}) \|_C^2 = \boldsymbol{\epsilon} : \mathbb{C} : \boldsymbol{\epsilon} + \boldsymbol{\sigma} : \mathbb{C}^{-1} : \boldsymbol{\sigma}. \tag{5.1}$$

  The **DDI metric** $\mathbb{C}$ is the DDI distance parameter. It makes the features comparable and is used to weight differently strains and stresses for distance calculation. It is a positive definite fourth-order tensor (it has to be invertible). It is different from the elasticity tensor.

- A **mechanical state** is an point of the constitutive space representing the strain and stress state of a point of the sample, most of the time an integration point. The mechanical states are indexed with the element number $\bullet^e$ and a temporal index $\bullet_i$. They are noted $(\boldsymbol{\epsilon}_i^e, \boldsymbol{\sigma}_i^e)$. Mechanical states contain a strain part and a stress part. The strain part is measured and the stress part is estimated by the DDI. Mechanical states constitute the solution to the mechanical problem. A mechanical state preserves equilibrium equations:

$$\sum_{e=1}^{M} \boldsymbol{B}_{ej} w_e \boldsymbol{\sigma}_e = \boldsymbol{f}_j \qquad \forall j, \tag{5.2}$$

  with M the number of mechanical states, $\boldsymbol{B}_{ej}$ the connectivity matrix, w_e the elements weights, and $\boldsymbol{f}_j$ the net forces. The mechanical states are represented by round markers in our figures.

- A **material state** is a point of the constitutive space. The material states constitute a sampling of the mechanical response of the material, but they are not solution to the mechanical problem. The group of the material states is called the **material database**. The material states are represented as stars in our figures. There is N^* material states in the database. The r^* **ratio** is the ratio between the number of mechanical states M and material states N^*. It is one parameter of DDI.

- The **DDI distance** is a distance defined on the constitutive space. It describes the distance between the mechanical states and the material database. The DDI distance is defined as:

$$d = \frac{1}{2} \sum_e \sum_i w_e ||(\boldsymbol{\epsilon}_i^e - \boldsymbol{\epsilon}_{k^{e,i}}^*, \boldsymbol{\sigma}_i^e - \boldsymbol{\sigma}_{k^{e,i}}^*)||_{\mathbb{C}}^2, \tag{5.3}$$

  $(\boldsymbol{\epsilon}_i^e, \boldsymbol{\sigma}_i^e)$ being the mechanical state associated with element e at time step i and $(\boldsymbol{\epsilon}_{k^{e,i}}^*, \boldsymbol{\sigma}_{k^{e,i}}^*)$ the mechanical state of cluster k, in which the element e at time step i is represented, and w_e the weight of element e.

- This distance is used to build a **pairing** between mechanical states and material states: each mechanical state is paired with the closer material state with regards to the DDI distance. This pairing defined N^* clusters of mechanical states, each cluster beeing paired with one material state. When $\mathbb{C}$ increases, the pairing is mostly based on the strain part of the states and when $\mathbb{C}$ decreases, it is mostly based on the stress part of the states.

5.1.1.2 Algorithm structure and principle

The algorithm principle is illustrated in Figure 5.1. The **inputs** are:

- the sample,
- the kinematic fields (strain part of the mechanical states),
- the net forces measured during the experiment,
- and the DDI parameters r^* and $\mathbb{C}$.

The DDI algorithm is searching for the minimisation of the distance between mechanical states and material states for the whole sample and the complete loading history, while constraining the stress part of the mechanical states with the equilibrium equation.After computation, the algorithm delivers three **outputs**:

- balanced stress fields, which are solutions of the mechanical problem (stress part of the mechanical states),
- the material database (the gathering of all the material states),
- and the pairing between mechanical and material states.

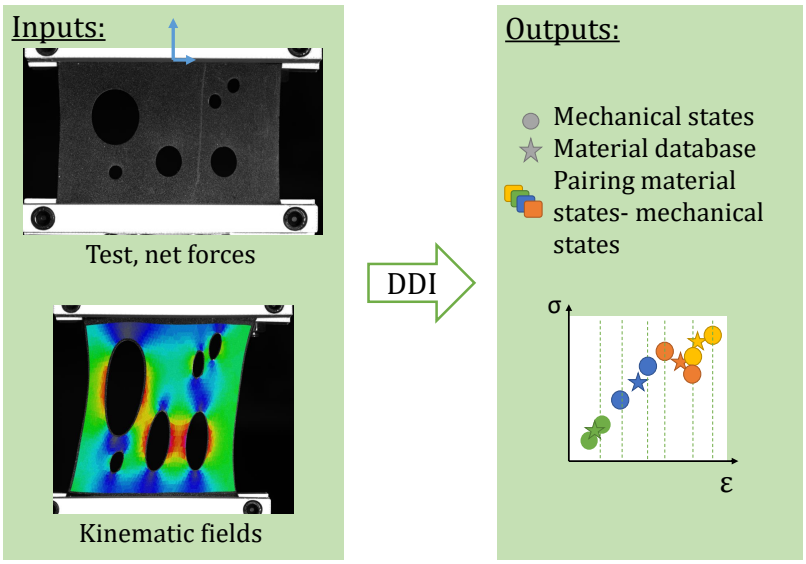

Figure 5.1: DDI algorithm inputs and outputs. The mechanical states are represented by circles while the material states are represented with stars. The clustering of mechanical states and their pairing with material states is represented by the colours. The dotted lines represent the measured strain.

The algorithm has an iterative structure, described in Figure 5.2. The initialisation step consists of the initialisation of the stress part of the mechanical states, and a k-means clustering: mechanical states are paired with material states.

Once the initialisation is completed, the iterations begin. Each iteration is composed of three successive steps:

- First, the strain part of the material states is updated. It consists in adjusting the strain part of the material state to place it at the center of the custer it is paired with. The material strain is the weighted average of its clusters mechanical states strain part. It consists in minimising the distance between mechanical states and the material databases, by searching new material states positions in the constitutive space such as:

$$\text{solution} = \arg\min_{\boldsymbol{\epsilon}^*_{k^e}} \frac{1}{2} \sum_e \sum_i w_e ||(\boldsymbol{\epsilon}^e_i - \boldsymbol{\epsilon}^*_{k^e}, \boldsymbol{\sigma}^e_i - \boldsymbol{\sigma}^*_{k^e})||^2_{\mathbb{C}}. \tag{5.4}$$

- Second, the algorithm enters a nested loop: the stress part of the mechanical states, represented by round markers, is adjusted. This adjustment guarantees that the resulting stress field respects the mechanical equilibrium in the sample, while finding the stress field which minimises the DDI distance between mechanical states and the current material database: it is a minimisation procedure, constrained by the equilibrium equation. The algorithm minimises the distance between the mechanical states and the material database, with the mechanical stresses as parameters, such as:

$$\text{solution} = \arg\min_{\boldsymbol{\sigma}^e_i} \frac{1}{2} \sum_e \sum_i w_e ||(\mathbf{H}^e_i - \mathbf{H}^*_{k^e}, \boldsymbol{\sigma}^e_i - \boldsymbol{\sigma}^*_{k^e})||^2_{\mathbb{C}}, \tag{5.5}$$

  with respect to Eq. 5.2. Then, the stress part of the material states is adjusted by calculating the weighted average of its cluster mechanical states stress part, minimising the distance between mechanical states and the material database, with this time material stresses as parameters, such as:

$$\text{solution} = \arg\min_{\boldsymbol{\sigma}^*_{k^e}} \frac{1}{2} \sum_e \sum_i w_e ||(\mathbf{H}^e_i - \mathbf{H}^*_{k^e}, \boldsymbol{\sigma}^e_i - \boldsymbol{\sigma}^*_{k^e})||^2_{\mathbb{C}}. \tag{5.6}$$

  . This nested loop goes on until the update of the material states stress part is neglectible. It consists in an alternate minimisation procedure.

- Third, the clustering is updated. A k-means algorithm parts the mechanical states in a given number of clusters, using their closeness in the sense of the DDI distance. This is also a distance minimisation procedure, minimising the distance between each material state and the mechanical states it is paired with, according to DDI distance, with the pairing as parameter, such as:

$$\text{solution} = \arg\min_{k^e} \frac{1}{2} \sum_e \sum_i w_e ||(\mathbf{H}^e_i - \mathbf{H}^*_{k^e}, \boldsymbol{\sigma}^e_i - \boldsymbol{\sigma}^*_{k^e})||^2_{\mathbb{C}}. \tag{5.7}$$

The iterative process continues while the clustering is adjusted at the end of each iteration. Finally, the algorithm exits with balanced mechanical states stress field, which is the solution of the mechanical problem and a material database which samples the mechanical response of the material.

This algorithm has been adapted to experimental applications in 2019 [29], but also to plasticity in 2022 [53]. The expansion of the constitutive space to encompass viscous effects or multi-material samples has also been explored [93]; while the coupling between DDI and Digital Image Correlation (DIC) has been studied for experimental purposes in 2023 [101]. This work expands the pioneer steps of Dalémat [29] and encompasses a corrective procedure for erroneous strain results from DIC. This method could be applied

within our framework to ensure a more accurate sress-strain estimation. The sources of uncertainty have recently been modelled using polymorphic uncertainty modelling to ensure DDI can properly deal with material natural variability [103]. Such a procedure could be applied inside our DDI framework, but we did not investigate it due to time considerations.

5.1.2 Adaptations for hyperelasticity

Some adaptations have been made for hyperelastic applications. In her PhD work, Dalémat proposed a modification of the constitutive space for finite strain [28]. It replaces the infinitesimal strain tensor $\boldsymbol{\epsilon}$ by the Hencky's logarithmic strain tensor $\boldsymbol{H}$. Cauchy's stress tensor is kept for the stress part of the constitutive space. The minimisation problem is now written as:

$$\text{solution} = \arg \min_{\boldsymbol{\sigma}_i^e, \mathbf{H}_{k^e}^*, \boldsymbol{\sigma}_{k^e}^*, k^e} \frac{1}{2} \sum_e \sum_i w_e ||(\mathbf{H}_i^e - \mathbf{H}_{k^e}^*, \boldsymbol{\sigma}_i^e - \boldsymbol{\sigma}_{k^e}^*)||_{\mathbb{C}}^2, \tag{5.8}$$

$(\boldsymbol{H}_i^e, \boldsymbol{\sigma}_i^e)$ being the mechanical state associated with element e at time step i and $(\boldsymbol{H}_{k^e}^*, \boldsymbol{\sigma}_{k^e}^*)$ the mechanical state of cluster k, in which the element e at time step i is represented, and w_e the weight of element e, with respect to Eq. (5.2).

The case of missing data has been investigated [28]. The holes in a pierced sample have to be considered. During DIC, the mesh elements cannot fit perfectly the sample's hole boundaries. This boundary has to be constrained to tackle the issue of a missing material strip. Each hole edge is constrained to be balanced within itself, according to Dalémat's recommandations.

When working with a homogenous material, and no consideration for time-dependent response, the stress-strain response is unequivocally defined. The strain part of mechanical states is then sufficient to build a perennial clustering, which will not be updated during DDI iterations. The DDI process used in this work is described in Figure 5.3. The pairing, noted k^e, is now fixed after the initialisation step, and is no longer one of the minimisation problem variable.

The present framework is based on a constitutive space built with the logarithmic strain tensor and Cauchy stress tensor, and a simplified iteration procedure. The initialisation of the stress part of mechanical states is made by setting the stress part to the null tensor. Then, $\mathbb{C}$ is defined by setting Young's modulus to $E = 1$ MPa and Poisson's ratio to $\nu = 0.5$ and writing:

$$\mathbb{C} = \begin{bmatrix} \frac{E}{(1-\nu^2)} & \frac{\nu E}{(1-\nu^2)} & 0 \\ \frac{\nu E}{(1-\nu^2)} & \frac{E}{(1-\nu^2)} & 0 \\ 0 & 0 & \frac{2E}{2(1+\nu)} \end{bmatrix}. \tag{5.9}$$

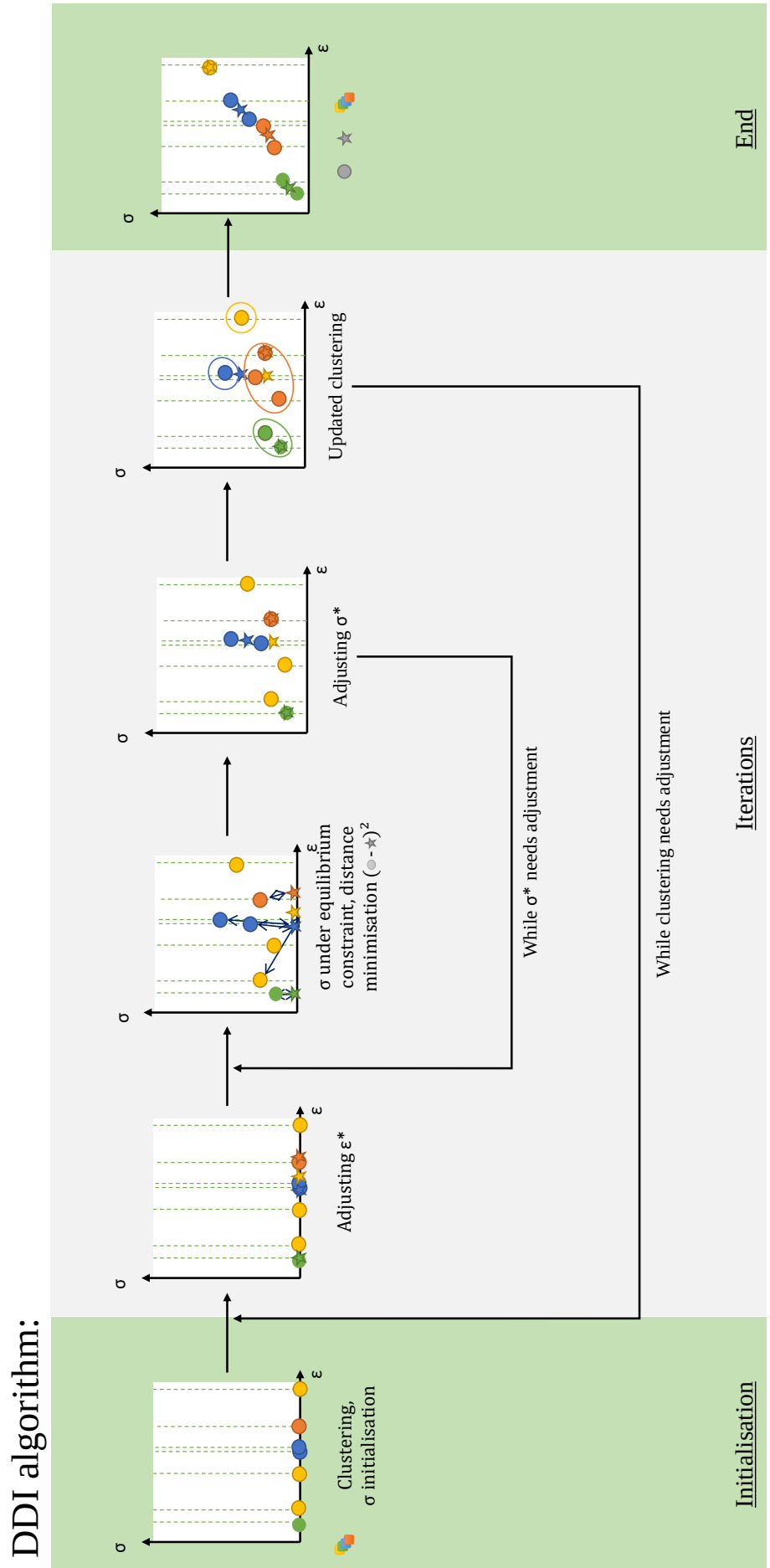

Figure 5.2: DDI: an iterative algorithm. The mechanical states are represented by circles while the material states are represented with stars. The clustering of mechanical states and their pairing with material states is represented by the colours. The dotted lines represent the measured strain.

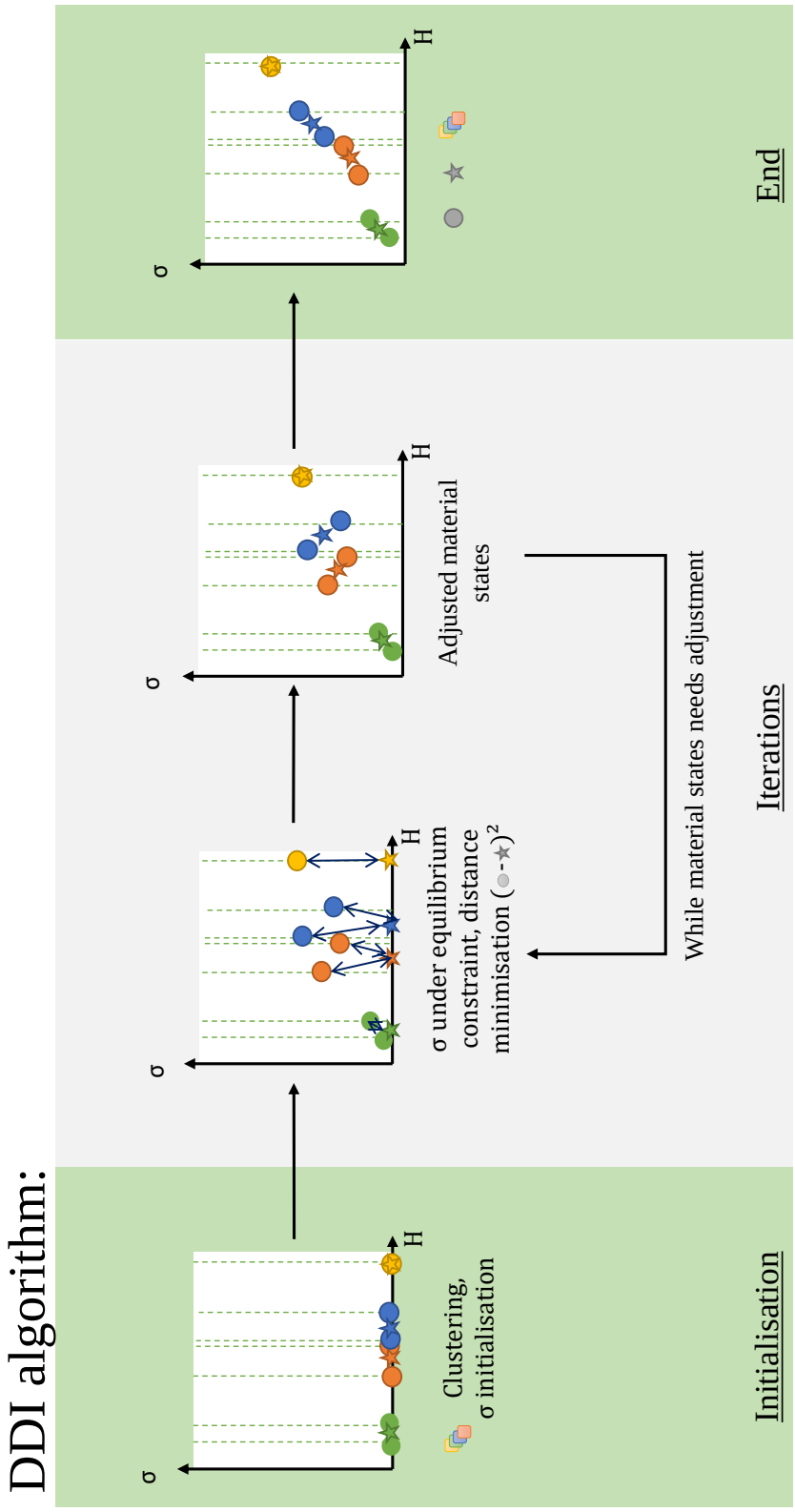

Figure 5.3: Adaptations of DDI algorithm for this work. The mechanical states are represented by circles while the material states are represented with stars. The clustering of mechanical states and their pairing with material states is represented by the colours. The dotted lines represent the measured strain.

The last DDI parameter to be discussed is the ratio between the number of mechanical and material states r^*. For synthetic data, this ratio is chosen at $r^* = 44$, according to Dalémat's recommendations to set it in the $[10; 100]$ interval. For experimental data, r^* is set to 1000. The experimental data presented here do present a tighter time sampling and a higher redundancy than the synthetic data due to the choices of loading: considering that the hexapod device does not operate with sharp slope breaks in the prescribed displacements, all displacement trajectories have been smoothed out with sine functions. The construction of the loading path with sine attenuation at the beginning and end of each phase is one of the providers of redundancy in the data, by generating kinematically close successive time steps when reaching the null derivative. The number of material states is then reduced to avoid overfitting.

5.1.3 Limitations and possible extension

DDI is a quite recent method and can handle specific material behaviours. To this day, we can cite simple elasticity, dealt with in the original publication of Leygue [57], hyperelasticity and noisy data, with an experimental approach, developed by Dalémat [29]. Rethoré [81] completed this work on experimental data with coupling between digital image correlation and DDI stress calculations. Heterogeneous materials have also been submitted to DDI by Valdes-Alonzo [93][92], leading to preliminary work on viscoelasticity. Stress field computation on plastic materials has been developed by Langlois [53], following recommendations of Eggersmann [34] on the plasticity representation. Ciftci *et al.* [18] have been working on the development of DDI approaches for history-dependent behaviours. Their work presents applications for two-dimensional problems. Whereas, Cameron *et al.* [14] have been working on an extension to plasticity, with an alignment assumption between either strain and stress tensors or stress and strain rates (assumption first made by Saint-Venant in 1871) on stress and strain. Their method can be applied to elasto-plasticity in a certain range of strains. Viscoplastic steel response has been successfully characterised with data-driven identification by Vinel [95], using ultra-high speed imaging and digital image correlation. Fracture mechanics have been explored with Data-driven methods by Carrara [15]. All those developments can be coupled with the Data-Driven Model Identification method presented in Chapter 6 to adapt it to multiple cases.

The following section presents DDI results for synthetic data and one of the experimental datasets. The other DDI results are not presented here.

5.2 A 3D-map to explore the mechanical response of materials

This section aims to present an enhanced map derived from the kinematic map built in Chapter 4, representing the full mechanical response of a material (strains and stresses). First, the stress fields estimated by DDI are observed and described before introducing the feature which will be added to the map.

5.2.1 Observation of the stress field

The first observation is made similarly to the observation of strain fields from Chapter 4 with bar histograms. Both experiments presented are under the plane stress hypothesis, and the third diagonal component is always equal to zero. The tensor components represented have been chosen similarly to the previous chapter. The presented stress tensors

contains both the material response and the hydrostatic pressure. Figure 5.4 presents the bar histogram visualisation of the DDI stress field for synthetic data.

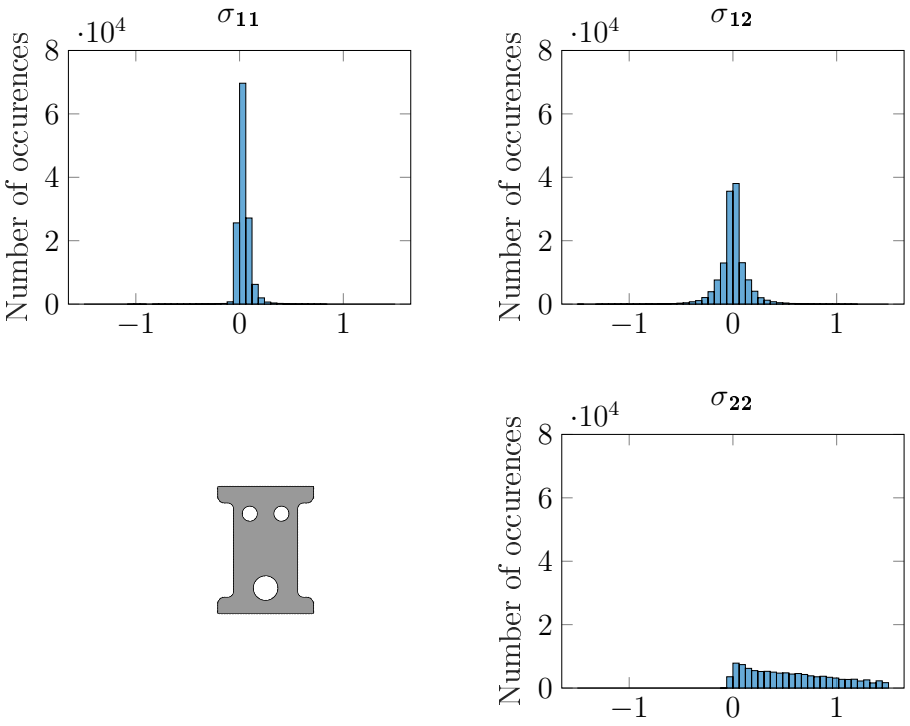

Figure 5.4: Bar histogram visualisation for Cauchy stress tensor components of synthetic data. The stress tensor components values are expressed in Pa.

The second diagonal component, σ_{22}, presented on the bottom right histogram, is mostly positive and presents the highest values. It is consistent with the strain observation made before, and is also consistent with the nature of the loading in this experiment: the sample undergoes a vertical displacement of its upper boundary, the vertical axis being the second of the coordinate system. The first diagonal component presents smaller values, close to zero. It is mainly positive. The shear component σ_{12} seems centred around zero, presenting both positive and negative values. This is consistent with the symmetry of the sample described in Figure 3.1. Overall, the majority of the elements seem to undergo uniaxial tension loading, because both the shear component and the first diagonal component are close to zero, whereas the stress component corresponding to the loading direction is larger and positive.

Figure 5.5 presents the bar histogram visualisation of the DDI stress field for experimental data.

This data set is under the plane stress hypothesis, and the third diagonal component σ_{33} is always equal to zero. The second diagonal component σ_{22} presents positive values, and the maximal values among the components. It corresponds to the direction where the imposed displacement is the highest. The first diagonal component σ_{11} displays positive values of lesser magnitude while the shear component σ_{12} displays both positive and negative values of moderate magnitude.

This representation gives an overview of the stress field but is not suited to indicate the magnitude of the stress nor other relevant information about the stress state the material is in. The choice is made to stick to the definition of hyperelasticity and characterise

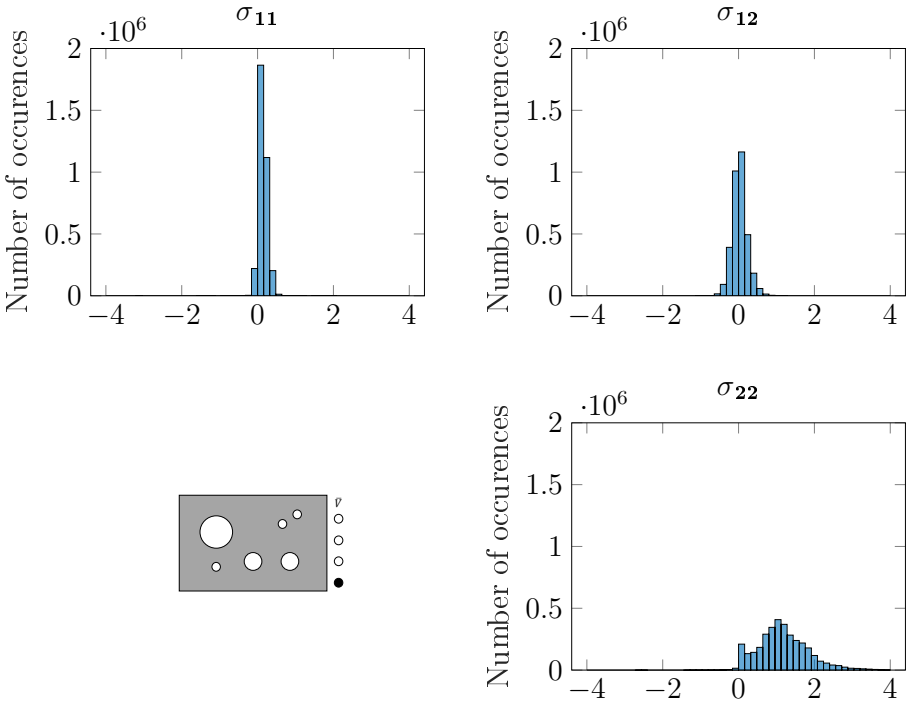

Figure 5.5: Bar histogram visualisation for Cauchy stress tensor components of experimental data. The stress tensor components values are expressed in Pa.

the mechanical response of the material with strain energy density.

5.2.2 From DDI stress field to strain energy density

Hyperelastic materials are usually described using strain energy density. Instead of using a model, strain energy density can be calculated using strain and stress field. The rate of deformation gradient $\boldsymbol{D}$ is defined by [45]:

$$\boldsymbol{D} = \frac{1}{2}((\dot{\boldsymbol{F}} \cdot \boldsymbol{F}^{-1}) + (\dot{\boldsymbol{F}} \cdot \boldsymbol{F}^{-1})^T), \tag{5.10}$$

with $\boldsymbol{F}$ being the deformation gradient. This rate of deformation tensor is used to calculate the strain energy density field:

$$W_i^e = \int_0^{t_i} \boldsymbol{\sigma}^e(t) : \boldsymbol{D}^e(t) \mathrm{d}t, \tag{5.11}$$

for each element e at time step i using DDI stress field $\boldsymbol{\sigma}^e(t)$. This feature encompasses both strain and stress fields, and is used to build a map representing the full mechanical response of the material. Considering that $\mathrm{tr}(\boldsymbol{D}) = 0$, the strain energy density calculus gets rid of the hydrostatic pressure that is encompassed into $\boldsymbol{\sigma}_i^e$. When there is no need to refer to a particular element or time step, W_i^e will be referred to as W_{DDI}.

5.2.3 (K_2, K_3, W) map

Figure 5.6 presents the mechanical response map for the synthetic data presented in Chapter 3.

This map is a three-dimensional plot presenting the strain energy density W obtained experimentally using measured strain field and estimated stress field with DDI, presented along Hencky's logarithmic strain invariants K_2 and K_3. These data are represented by

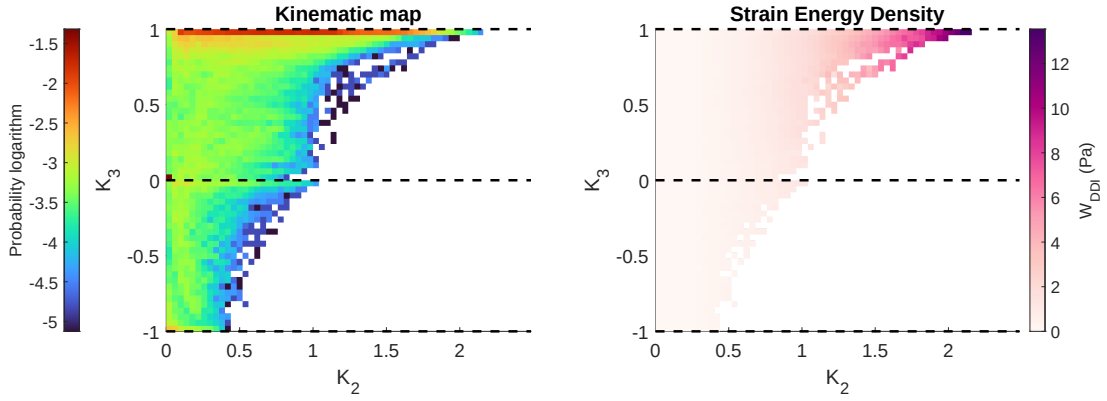

(a)

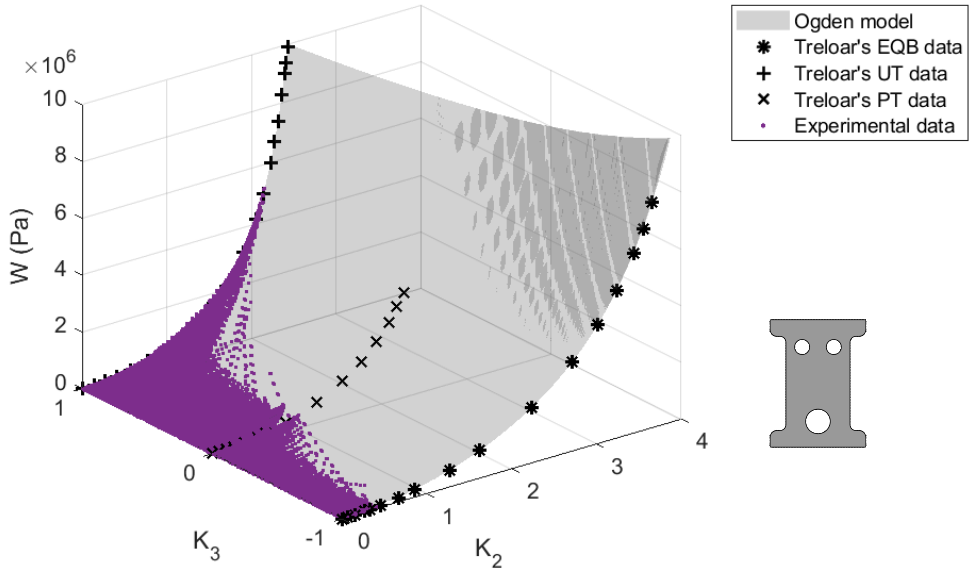

(b)

Figure 5.6: (a) Kinematic map plotted along the projection of W_{DDI} on the (K_2, K_3) plane. On the left figure, the colourmap represents the point density, whereas on the right figure, the colourmap represent the average DDI strain energy density value for the points located in the sub-space. (b) Mechanical response map for synthetic data. The experimental points are presented as purple dots. The grey surface represents the model response of the Ogden model used to build the synthetic data. Trelor's data [91] are presented as black markers.

purple dots. Considering that synthetic data is built using an Ogden model, the surface corresponding to the model is added to the figure. The experimental points show a good agreement with the model surface. The two upper figures represents the kinematic map on the left and an orthogonal projection of W_{DDI} on the (K_2, K_3) plane. For each pixel of the map, the average strain energy density value is calculated. These projections are shown along the mechanical response map to enhance readability.

Treloar's data [91] are also presented on the plot. This mechanical response map gives clues of the necessary data to fit a model to a material response. Identifying the

mechanical response of a material consists in finding the grey surface which will match experimental points the best. In the classical method, described in Chapter 1, simple deformation states experiments are used. They represent three "slices" of the surface and present discontinuous data along the K_3 axis. In full-field measurement-based methods, the data is more spread along the K_3 axis and closely mapping the lower part of the surface, with relevant information for every deformation state. This data spread is believed to be beneficial to ensure identification method provides a model that is adapted to the material for more than simple deformation states. Figure 5.7 presents the experimental strain energy density points plotted along logarithmic strain invariants K_2 and K_3 for our complex experiments.

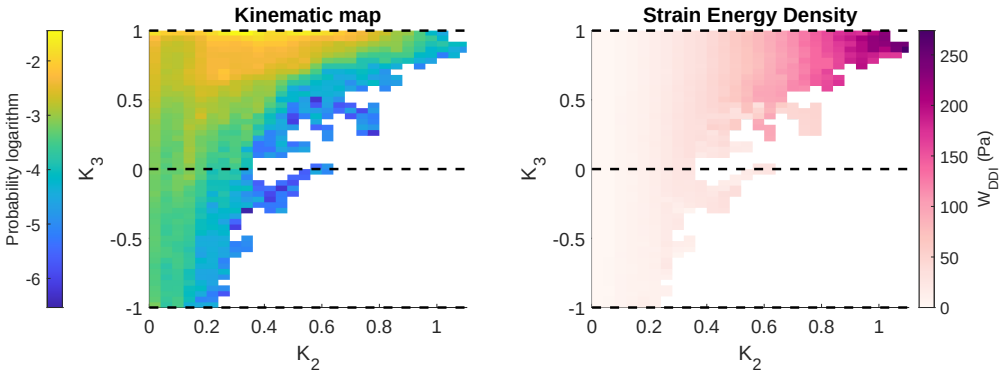

(a)

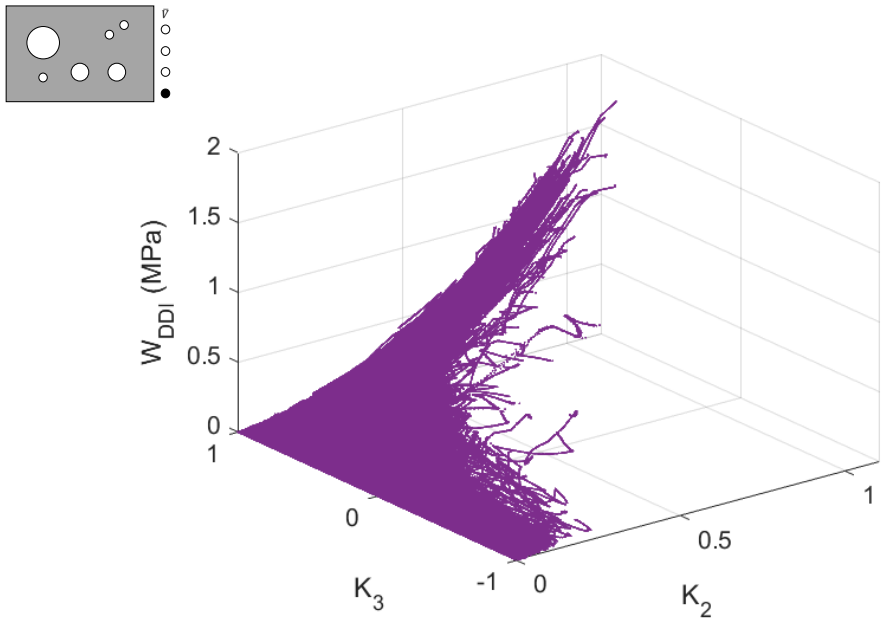

(b)

Figure 5.7: (a) Kinematic map plotted along the projection of W_{DDI} on the (K_2, K_3) plane. On the left figure, the colourmap represents the point density, whereas on the right figure, the colourmap represent the average DDI strain energy density value for the points located in the sub-space. (b) Mechanical response map for experimental data.

The point cloud seems to follow a curved surface. The point cloud is thin in the strain energy density direction, meaning that DDI did estimate close strain energy density values related to close (K_2, K_3) couples. The upper right figure shows some points do not seem to follow the trend of the other points: it seem that their strain energy density values are lower than expected. These points are located around $K_3 = 0.4$ and spread from $K_2 = 0.4$ to $K_2 = 0.8$. Those can be points whose stresses were under-estimated by DDI or points whose kinematics were triggered by a huge amount of noise during DIC procedure. Their number is not significant enough for them to corrupt further applications (see Chapter 6).

This mechanical response map is used in Chapter 6 to visualise the agreement between a fitted model and DDI results for experimental data. Further observation of DDI strain energy density results can be conducted. Figure 5.8 presents "slices" of the (K_2, K_3, W) point cloud in the (K_2, W) plane at five different K_3 values. The sampling along K_3 axis is chosen to be periodic with a 0.5 step. The thickness of the resulting filtred point clouds can be observed. The first one, corresponding to $K_3 \geqslant 0.995$ has a maximal thickness of 0.075 MPa, while the other point clouds exhibits a maximal thickness around 0.05 MPa. The observed thickness appears to confirm the good strain energy density estimation made with DDI. Some noise can be observed, resulting from DIC noise or "weak" clusters during DDI process. Another layer of analysis could be added by plotting the same five point clouds with a density plot, assessing if the thickness inherits from a few scattered and noisy points or if the point cloud is homogeneous along its thickness. A hint on the answer is provider later in the manuscript with Figure 6.15.

5.3 Conclusion

The DDI method allows to calculate an admissible stress field from experimental data. The diverse observations of the stress field, either with bar histograms or using Lode invariants, show a good agreement between DDI stress data and kinematic experimental data. These multiple features could not be easily encompassed in a mechanical response map, and another feature is chosen to represent the stress response of the material.

The DDI stress field can be used to calculate the strain energy density field, which characterises the mechanical response of hyperelastic materials. Strain energy density is then plotted on a three-dimensional graph along Hencky's logarithmic strain tensor invariants K_2 and K_3. The resulting point cloud is widely spread along the K_2 and K_3 axis, but thin the strain energy density axis: it defines a mechanical response surface, specific to the tested material.

This graphical tool summarises the identification process for a full-field measurement-based method: identification is finding the equation of the surface that is best matching with the point cloud of the mechanical response map. It can also help design experimental tests precisely meshing the response surface to enable good quality identification procedures.

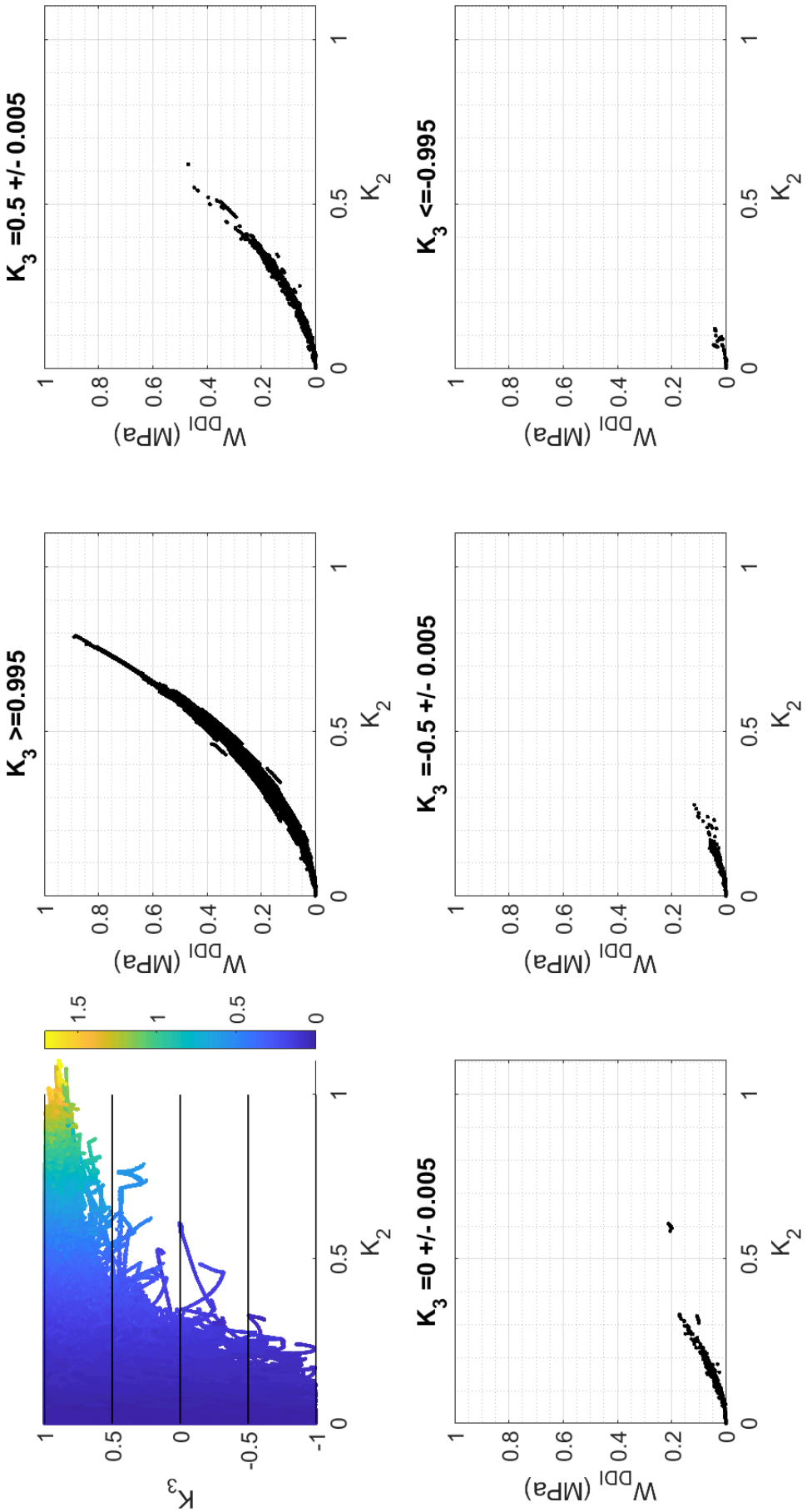

Figure 5.8: DDI (K_2, K_3, W) point cloud and (K_2, W) plane projections of the point cloud data filtred by K_3 value.

Part III

Application to material characterisation

Chapter 6

Data-Driven Model Identification

Data-Driven Model Identification or DDMI is an identification method which aims to combine the benefits of both the classical identification method and full-field measurement-based identification methods. It consists in running a multiaxial experiment and measuring the corresponding kinematical fields, then running DDI to estimate stress and strain energy density fields. Once the features are collected, a model can be chosen and fitted to experimental data. The fitting procedure can be applied to the DDI stress field or strain energy density field. Different objective functions have been tested and compared on synthetic data. The best method is then applied to experimental data.

Overall, the best and most convenient fitting method relies on an absolute error-based objective function written with a variable change, and minimising the distance between strain energy density fields.

DDMI is applied to experimental data. Two models are fitted on the DDI strain energy density field: the third-order Ogden model and the Yeoh model. Both model strain energy density fields are compared with the DDI strain energy density field and show error levels consistent with the ones observed with synthetic data. The comparison with uniaxial tension data proves that the two DDMI-fitted models can represent the material behaviour in the strain range of the experimental dataset.

Contents

The identification methods have been explored in Chapter 1. The analysis of the methods and their costs led us to propose an identification method that gathers the benefits discussed in the first chapter: a unique and complex experiment benefiting from DIC to measure experimental fields, and a "off-line" fitting step allowing to choose the model after the high "cost" identification steps. As Data-Driven methods have already the ability to generate new constitutive laws, for example with unsupervised learning [37], the proposition is to use DDI to build an identification method. This method has been described in an article accepted for publication in Rubber Chemistry and Technology [24]. This Chapter presents an extended version of the publication.

6.1 Method

6.1.1 Concept and general framework

The Data-Driven Model Identification process is schemed in Figure 6.1; it consists of three successive steps.

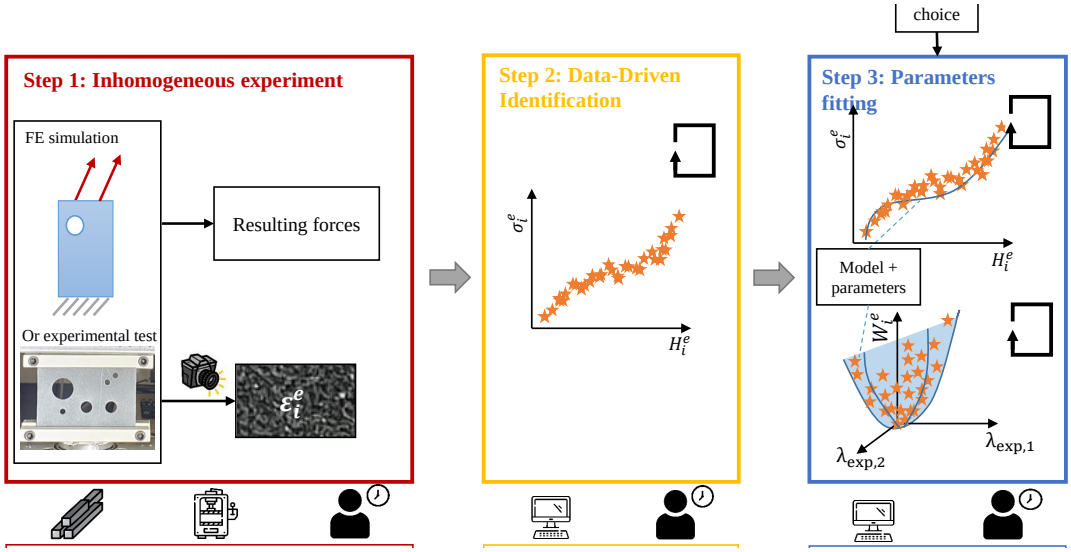

Figure 6.1: Data-Driven Model Identification method process. The costs are expressed for each identification step: test, DDI algorithm and parameters fitting. Those costs can be human time, testing machine time, material or samples, and computation time. The process can be adapted to both synthetic and experimental data. Two distinct paths can be explored for fitting parameters on the DDI stress field or fitting parameters on the associated strain energy density field. The optimisation procedures are symbolised by the squared looping arrows referring to Eqs. (5.8) in the second step and (6.2) and (6.3) in the third step.

The first step is experimental and inherits from full-field measurement methods with a unique complex test to run. The tests are presented in Chapter 3. The second step inherits from the features choice step of the standard identification method to compute stress fields. Nevertheless, the complex experiment generates non-homogeneous stress fields that cannot be simply computed with experimental features but need the help of a dedicated algorithm. Here, we use the DDI technique proposed by Leygue *et al.* in 2018 [57] and its extension to large strain provided by Dalémat [28] as presented in Chapter 5 to estimate the stress fields without any constitutive law. Finally, similarly

to the standard method, a constitutive law can be chosen and its parameters fitted, "off-line". A qualitative evaluation of the costs of this method is proposed in Figure 6.1. This evaluation is similar to the ones presented for the classical Identification method and FEMU in Chapter 1. The first step is equivalent to the first FEMU step and evaluated as such: with low material sample costs and intermediate costs in machine and human time. The last step is similar to the last step of the standard one, and evaluated at a low cost in computational time and an intermediate cost in human time. The majority of the cost inherits from the DDI step, needing larger computational time.

This method is applied to numerical data presented in Chapter 3 in Section 6.2, and to experimental data in Section 6.3.

6.1.2 Minimisation problem

Some methods and tools have to be defined regarding Data-Driven Model Identification. This section will focus first on the objective functions defined for material model parameters fitting.

As shown in Figure 6.1, the last step of the Data-Driven Model Identification method consists of choosing a model and fitting its parameters to experimental data. Different fitting approaches are presented here:

- on the stress field, as done classically with simple deformation states experiments,
- on the strain energy density field, using the energetic formulation of hyperelastic constitutive models. This procedure can be achieved thanks to the DDI stress field, which can be used to calculate the strain energy density field W_{DDI}. Once the strain energy density field calculated, hyperelastic models parameters can be determined on strain energy density, as seen in Figure 6.1. For a hyperelastic material, strain energy density can be calculated using stress field $\boldsymbol{\sigma}^e_{DDI_i}$ and $\mathbf{D}$, the Eulerian deformation rate tensor, computed from the deformation gradient $\mathbf{F}$, which is extracted from the kinematic fields measured using DIC:

$$W^e_{DDI_i} = \int_0^{t_i} \boldsymbol{\sigma}^e_{DDI}(t) : \boldsymbol{D}^e(t)\mathrm{d}t, \text{ with } \boldsymbol{D} = \frac{1}{2}((\dot{\boldsymbol{F}} \cdot \boldsymbol{F}^{-1}) + (\dot{\boldsymbol{F}} \cdot \boldsymbol{F}^{-1})^T). \quad (6.1)$$

Third-order Ogden models are fitted on both the DDI stress field and strain energy density field. Ogden model formulation for stress and strain energy density is given in Eq. (3.1) and (1.6).

Three types of objective functions are used on numerical data, and the most convenient one is used for DDMI on experimental data. The first objective function that is considered is based on relative errors between model data and DDI data, and the second one is based on absolute errors. The third one is absolute errors-based and includes a variable change to guarantee the model's polyconvexity during optimisation procedure. They are described in the next sections.

6.1.2.1 Relative error-based objective functions

The first method investigated when developing DDI is based on relative errors. The objective function for the "stress-fit" path is expressed using the DDI $\boldsymbol{\sigma}^e_{DDI_i}$ and model

$\hat{\boldsymbol{\sigma}}_i^e(\mathbf{y})$ stress tensors associated with each mesh element e at each time step i and is given by:

$$\mathbf{y}_{\text{sol}} = \arg\min_{\mathbf{y}} \sum_i \sum_e \frac{\| \hat{\boldsymbol{\sigma}}_i^e(\mathbf{y}) - \boldsymbol{\sigma}_{DDI_i}^e \|_2}{\| \boldsymbol{\sigma}_i^e \|_2}, \tag{6.2}$$

with $||\boldsymbol{\sigma}||_2^2 = (\boldsymbol{\sigma} : \boldsymbol{\sigma})$ and the model parameters being represented by $\mathbf{y}$. The second fitting path is built considering the availability of the stress field calculated with DDI, and the non-linear elastic nature of the materials used for this identification path. The fitting process is adapted to hyperelastic constitutive laws and models, written as strain energy densities, and based on a new objective function:

$$\mathbf{y}_{\text{sol}} = \arg\min_{\mathbf{y}} \frac{1}{2} \sum_i \sum_e \frac{\left[W_{DDI_i}^e - W_i^e(y)\right]^2}{(W_{DDI_i}^e)^2}, \tag{6.3}$$

$W_{DDI_i}^e$ being the DDI strain energy density for element e et time step i, and $W_i^e(y)$ being the model's strain energy density calculated with parameter set y, where the double summation accounts for all the discrete time steps i and finite elements e. The major advantage of relative error is to lower the importance of the errors associated with large reference values. These points are scarce in our datasets, meaning larger possible errors after DDI calculus. This is caused by the clustering regularisation. However, relative errors tend to enhance the importance of errors related to lower reference value-associated points.

6.1.2.2 Absolute error-based objective functions

The second method investigated for DDI is based on absolute error. The objective functions are described below:

To discuss the choice of fitting the strain energy density rather than stress data, we modify Eq. (6.2) by changing the cost function as follows:

$$\mathbf{y}_{\text{sol}} = \arg\min_{\mathbf{y}} \frac{1}{2} \sum_i \sum_e \left\| \boldsymbol{\sigma}_{\text{DDI}_i}^e - \boldsymbol{\sigma}_i^e(y) \right\|_2^2. \tag{6.4}$$

Let y denote the vector of parameters involved in the model, and $W_i^e(y)$ represent the computed strain energy density to be fitted to the measured strain energy $W_{\text{DDI}_i}^e$ data points. The solution y_{sol} is obtained by minimising the following objective function:

$$\mathbf{y}_{\text{sol}} = \arg\min_{\mathbf{y}} \frac{1}{2} \sum_i \sum_e \left[W_{\text{DDI}_i}^e - W_i^e(y) \right]^2. \tag{6.5}$$

The absolute error minimisation processes gather the opposite advantages that the ones described for relative error earlier.

6.1.2.3 Objective function with variable change

As an example, we selected a 3-term Ogden strain energy function, which is the same model used to generate the data. It is well-known that each pair of parameters (μ_i,α_i) must satisfy $\mu_i\,\alpha_i > 0$ to ensure the polyconvexity of the strain energy function (see for example [45]). To naturally incorporate this constraint into the identification process, the strain energy density Eq. (1.6) or stress Eq. (3.1) is expressed in terms of (μ_i, β_i), where $\beta_i = \sqrt{\mu_i\,\alpha_i}$, ensuring that μ_i and α_i have the same sign.

The objective functions are the same as the ones from the previous section (6.1.2.2), the only features that change are the model's strain energy and stress formulation. Ogden's model is written with the variable change below:

$$\sigma_k = -q + \sum_{i=1}^{N} \mu_i \lambda_k^{\frac{\beta_i^2}{\mu_i}}, \tag{6.6}$$

q being the hydrostatic pressure, λ_k (k = 1,2,3) being the principal stretches, σ_k the principal stresses, N the order of the model, and (μ_i, β_i) the model parameters after the variable change. The same variable change can be applied to Ogden's model strain energy density formulation, as follows:

$$W = \sum_{i=1}^{N} \frac{\mu_i^2}{\beta_i^2} \left(\lambda_1^{\frac{\beta_i^2}{\mu_i}} + \lambda_2^{\frac{\beta_i^2}{\mu_i}} + \lambda_3^{\frac{\beta_i^2}{\mu_i}} - 3 \right). \tag{6.7}$$

6.1.3 Visualisation tools

This paragraph aims to present and describe the graphical tool that is used to compare strain energy density fields in the following sections. The choice has been made to represent strain energy density fields and stress fields. The stresses are six-component tensors and are compared using two metrics: the spherical part of the tensor $\sigma_S = \frac{1}{3}\text{tr}(\boldsymbol{\sigma})$ and the Von Mises norm of the stress tensor:

$$\sigma_{\text{VM}}^2 = \frac{1}{2}\left[(\sigma_1 - \sigma_2)^2 + (\sigma_2 - \sigma_3)^2 + (\sigma_3 - \sigma_1)^2\right]. \tag{6.8}$$

In this section, the visualisation tool is introduced with a focus on strain energy density representation. The same process is applied to the stress metrics. This graphical tool is a plot expressing the distribution of relative errors plotted against reference data. The reference data is from the finite element simulation described in Chapter 3. The horizontal axis expresses x, the relative error between the reference strain energy density field W_{ref} and a given strain energy density field W:

$$x(W) = \frac{W_{\text{ref}} - W}{W_{\text{ref}}}, \tag{6.9}$$

and the vertical axis expresses the reference strain energy density field W_{ref}. To display the distribution of relative error $x(W)$, the graph is discretised in a 100×100 grid. For each square of the grid, the number of points plotted inside is counted, and divided by the total number of points: this is the probability for one point $(x(W), W_{\text{ref}})_i^e$ associated with the element e at time i taken randomly in this experience to appear in the given square. For the sake of reading, a natural logarithm is applied to the probabilities and a corresponding colour bar is used: a red square expresses a high probability for a point taken randomly in this experience to appear in the given square, and a blue square a low density of points. It can be noted that several decades can separate blue and red squares. Overall, a point located in the right part of the figure, with $x(W) > 0$, expresses an overestimation of the quantity while a point located on the left part of the figure expresses an underestimation of the quantity.

Figure 6.2 presents four illustrative cases, built with Gaussian distributions:

- the top left figure represents the relative error distribution for a perfect method ($W = W_{\text{ref}}$), with a Gaussian distribution of reference data: relative errors are set to zero, and colours express the distribution of the reference data,

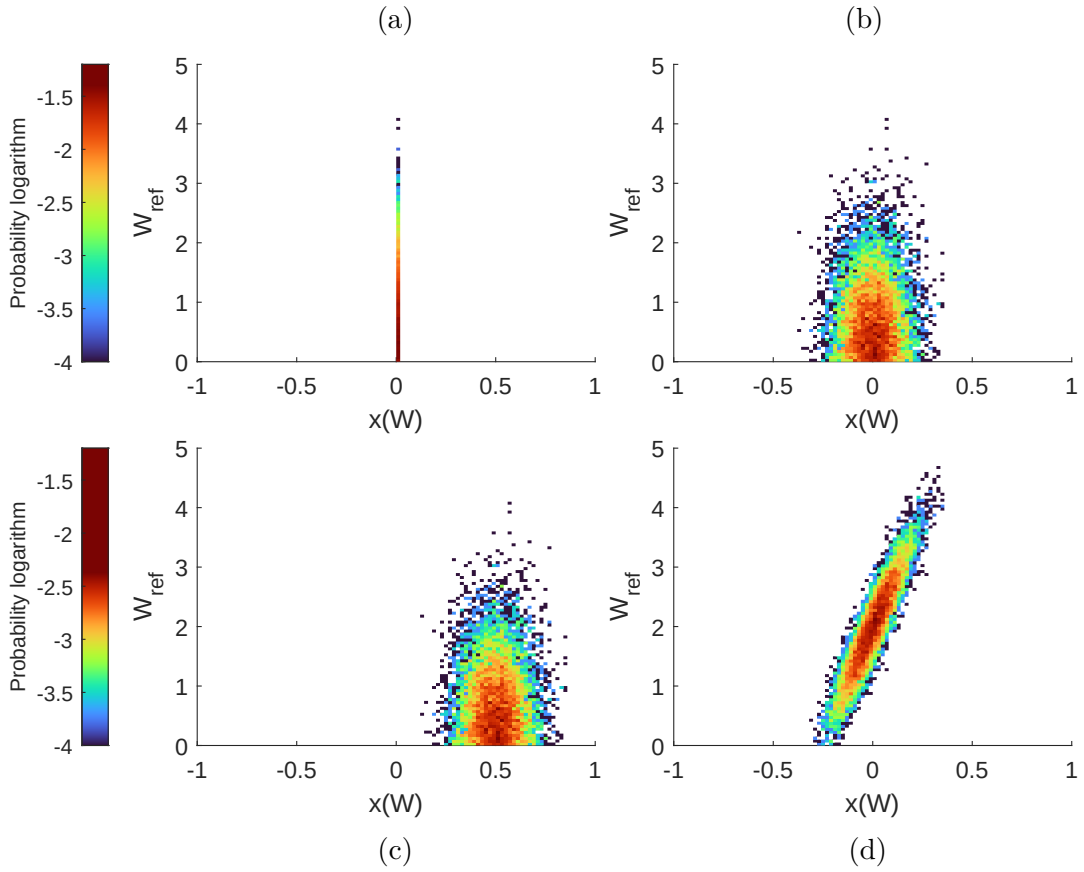

Figure 6.2: Four illustrations of density plots expressing reference data W_{ref} as a function of relative error $x(W)$.

- the top right plot represents the distribution of normally distributed relative errors, centred in zero and with a standard deviation of 0.1 ($< W >=< W_{\text{ref}} >$),
- the bottom left plot represents the distribution of normally distributed relative errors, centred in 0.5 and with a standard deviation of 0.1: this shows a systematic over-estimation of the data ($W_i^e > W_{\text{ref},i}^e \; \forall \; (i,e)$ and $< W >= 1.5 < W_{\text{ref}} >$),
- the bottom right plot represents a method that over-estimates data at large reference data values and under-estimates data at lower reference data values.

These artificial examples show the general trends that can be exhibited by the density plots. As shown in the following, these plots can be completed with other distribution visualisation tools such as histograms representing relative error distribution at a fixed reference data value.

6.2 Validation on synthetic data

The goal of this section is to present the results of the three fitting campaigns run on DDI data coming from the numerical experiment. First, DDI stress and strain energy density data are compared with the reference data, extracted from finite element simulations. Figure 6.3 displays the distribution of relative error between DDI and reference strain energy density plotted along the reference strain energy density.

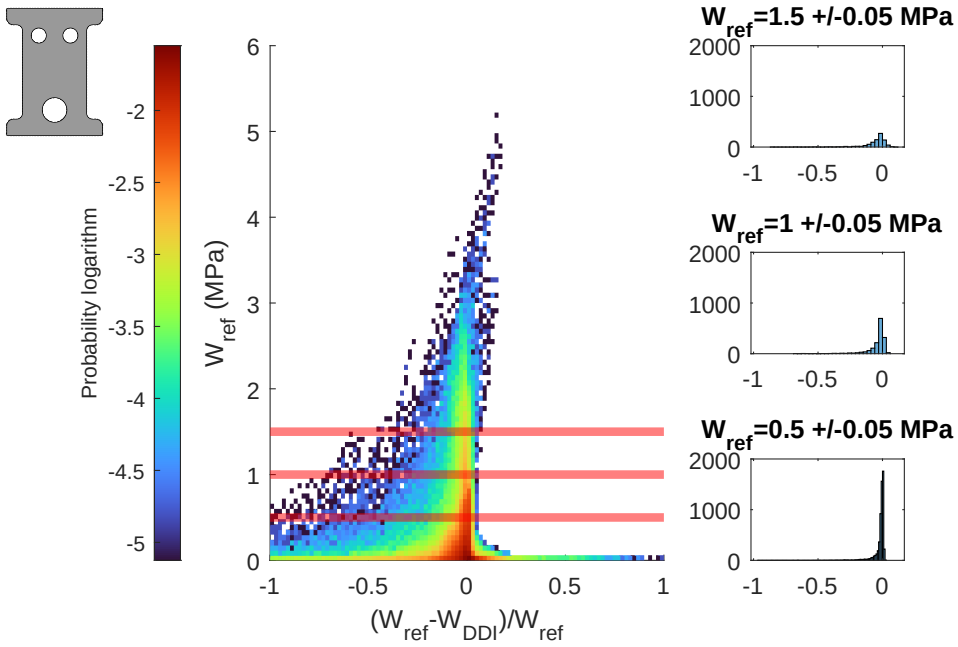

Figure 6.3: Relative error between DDI strain energy density and reference strain energy density field from Finite Element simulation. The three histograms on the right express the distribution of points within a small variation of reference strain energy density value.

The left part of the plot is based on the visualisation tool presented above. At first sight, one can observe that the vast majority of points, located in the red and orange areas, are located mostly along the vertical axis, meaning that this majority of points have a really small error. The DDI seems to estimate well the stress field when compared with the reference stress field.

The cloud point is shifted on the left at small reference strain energy density values and shifted on the right at larger reference strain energy density values. It seems that DDI is overestimating stress values at low reference strain energy density values and underestimating stress values at high reference strain energy density values. This phenomenon can be explained by the DDI path: the stress field estimated by DDI is constrained by mechanical equilibrium. If DDI overestimates some stress values, it has to underestimate other stress values to guarantee equilibrium.

The three histograms on the left-hand side relate the distribution of error along a fixed reference strain energy density value. The error distribution is centred on zero for the three cases. However, the distribution appears to be thinner when the number of points is larger. Again, this can be explained by the DDI resolution path: clustering is one of the keys of the algorithm, and DDI needs a certain number of points to cluster together to gain efficiency.

6.2.1 Fitted parameters

The first try of the method consisted in minimising the relative error between the fitted model and DDI stress and strain energy density fields, according to Eqs. (6.2) and (6.3). The two-term Ogden model and three-term Ogden model have been fitted on the DDI stress field, and the second-order Ogden model on DDI strain energy density data. The following sections focus on the "best" fits of the method: the second-order Ogden model

fitted on DDI strain energy density and the third-order Ogden model fitted on DDI stress field, which admits a smaller objective function value than the second-order Ogden model fitted on the same data.

6.2.1.1 Minimisation on relative error

The fitted parameters and corresponding shear modulus are presented in Table 6.1. The order of magnitude of each parameter is consistent with the reference model parameters presented in Table 3.1. The shear modulus μ, calculated according to Eq.(3.2), is in agreement with the reference shear modulus.

6.2.1.2 Minimisation on absolute error

The second test on the method was achieved using objective functions that minimise the absolute error between fields. Three-term Ogden models were fitted on both DDI stress and strain energy density. The fitted parameters and related shear modulus are presented in Table 6.2. Similarily than in the previous case, the order of magnitude of each parameter is consistent with the reference model parameters (Table 3.1), and the shear modulus μ is in agreement with the reference shear modulus.

6.2.1.3 Minimisation on an absolute error with variable change

The third test of the method was achieved using the same minimisation on absolute error but the procedure incorporates the above-mentionned variable change which constrains the admissibility of the parameters. The fitted parameters and related shear modulus are presented in Table 6.3. Similar conclusions than the two previous cases can be drawn. Note that two of the α parameters are close to zero, 10^{-11} and 10^{-12} respectively, and those terms do not influence the model much.

6.2.2 Comparison with DDI fields

As a summary, six models have been fitted. For each model, stress and strain energy density fields are calculated according to Eqs. (1.6) and (3.1). The visualisation tool presented in Section 6.1.3 is used to compare the different fields. Each method is represented by a given colour map. The models fitted on the stress field are presented on the left-hand side of the figure and the ones fitted on strain energy density fields are presented on the right-hand side.

First, the six model fields are compared with DDI stress then strain energy density fields in Figures 6.4 and 6.5. “High-density point clouds” are mentioned in the analysis of the following figures. This term corresponds to the point cloud, representing most points through its density. It corresponds to figure areas coloured with the highest colourbar colour.

6.2.2.1 Comparison with DDI stress fields

Representing stress tensors is difficult because of the dimensions of the objects. In this section, the choice is made to represent and compare two scalar features for stress field representation:

- the spherical part of the tensor,
- the Von Mises norm of the tensor.

Fit	Parameters						Shear modulus
	μ_1 (Pa)	μ_2 (Pa)	μ_3 (Pa)	α_1	α_2	α_3	μ (Pa)
On $\boldsymbol{\sigma}_{\text{DDI}}$	5.71×10^5	1.133×10^4	-	1.3	3.4	-	3.9×10^5
On $\boldsymbol{\sigma}_{\text{DDI}}$	5.49×10^5	1.02×10^4	1.18×10^4	1.3	3.5	1.3	3.8×10^5
On W_{DDI}	7.31×10^5	1.17×10^4	-	1.1	3.3	-	4.2×10^5

Table 6.1: Material parameters of the fitted Ogden model with minimisation on the relative error.

Fit	Parameters						Shear modulus
	μ_1 (Pa)	μ_2 (Pa)	μ_3 (Pa)	α_1	α_2	α_3	μ (Pa)
On $\boldsymbol{\sigma}_{\text{DDI}}$	4.12×10^5	9.23×10^3	2.27×10^3	1.74	1.74	1.74	3.7×10^5
On W_{DDI}	5.20×10^5	1.21×10^4	9.96×10^4	1.1	0.62	2.26	4.0×10^5

Table 6.2: Material parameters of the fitted Ogden model with minimisation on the absolute error.

Fit	Parameters						Shear modulus
	μ_1 (Pa)	μ_2 (Pa)	μ_3 (Pa)	α_1	α_2	α_3	μ (Pa)
On $\boldsymbol{\sigma}_{\text{DDI}}$	4.24×10^5	27.3×10^6	-5.65×10^5	1.74	0	0	3.7×10^5
On W_{DDI}	2.83×10^5	46.64×10^6	-3.15×10^5	1.91	5.85×10^{-4}	-0.84	4.0×10^5

Table 6.3: Material parameters of the fitted Ogden model with minimisation on the absolute error with variable change.

Figure 6.4 presents the comparison between fitted models and DDI stress fields.

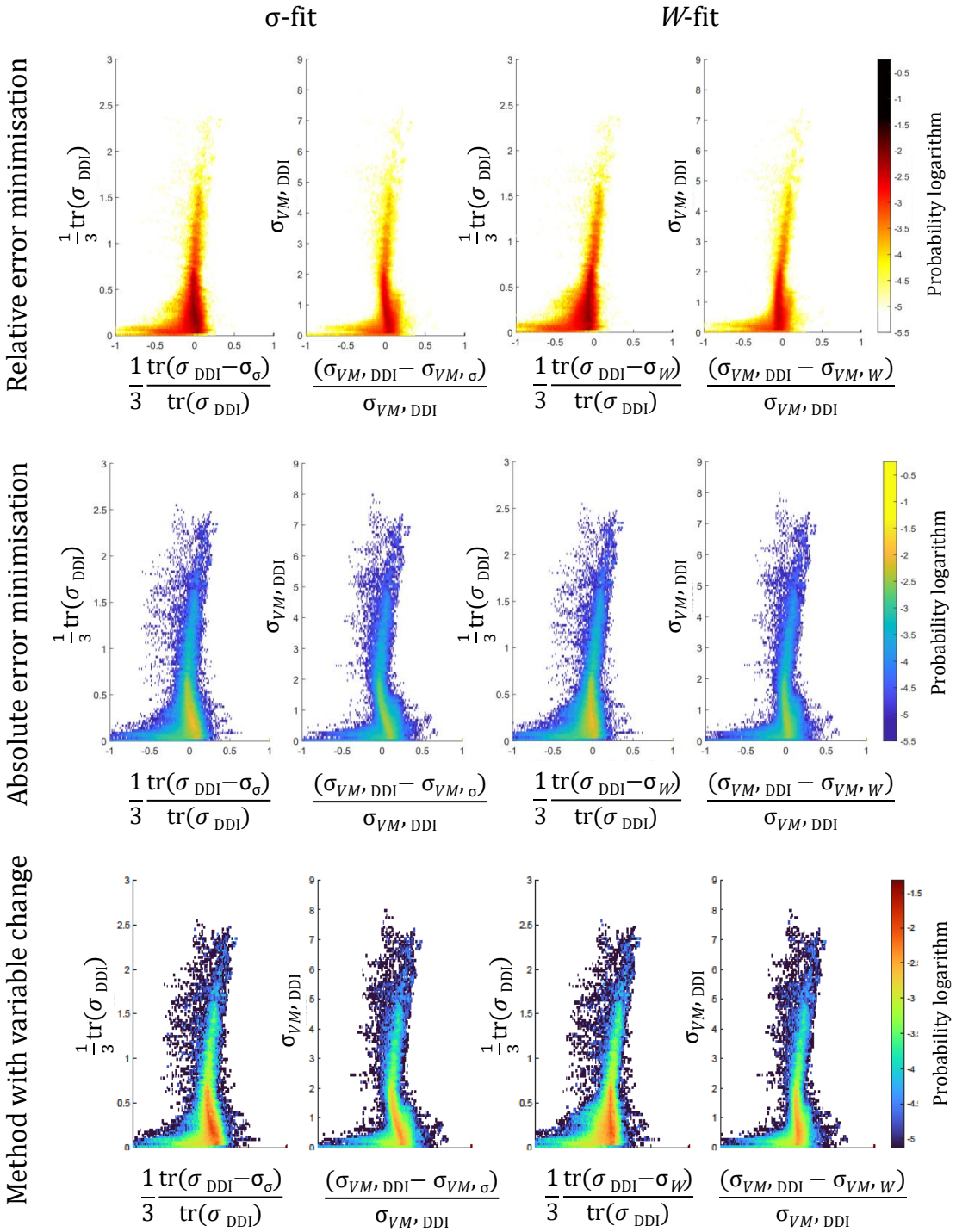

Figure 6.4: Comparison of stress fields between fitted models and DDI results. The first column indicates the method. Each figure presents a left plot representing the relative error between the spherical part of the stress tensors, and a left plot representing the relative error between the Von Mises norm of the stress tensors.

Each figure presents the relative error between the spherical part of the tensors on the left and the relative error between the Von Mises norms on the right. The methods are presented from top to bottom: relative error minimisation, absolute error minimisation,

and absolute error minimisation with variable change. Stress-fitted models are presented on the left and strain energy density-fitted models on the right.

At first sight, the six figures are very similar. For the six of them, the majority of points are located near the ordinate axis, meaning that the relative error between fitted model fields and DDI fields is low, due to the minimisation problem. Those zones presents a point density three to four decades higher than the external point cloud zones. The large base of the cloud point is due to the choice of representation: relative errors increase when the reference field value decreases. There is some scattering to be observed: some points present a larger error than others. Moreover, the scattering is wider on the spherical tensor part-related figures, meaning that the relative error between the DDI stress field and the identified stress field is higher on the spherical part of the stress field.

Differences can be observed between the methods: for the same minimisation error, the point cloud corresponding to the strain energy density-fitted model seems more vertical at the base, where the majority of points are. Overall, the same amount of scattering can be observed in both methods. Some seem to exhibit a better fit, with the high-density point cloud highly vertical and centred on the ordinate axis. That is the case of the W-fitted model with variable change, which can be observed at the bottom right cell of the figure.

6.2.2.2 Comparison with DDI strain energy density field

Figure 6.5 presents the comparison between fitted models and DDI strain energy density fields, using the visualisation tool presented in Section 6.1.3.

Again, the six figures are very similar, showing some scattering, which is amplified at low DDI strain energy density values by the representation of the relative error. The majority of points, represented by the top colours of each colourbar, are located near the ordinate axis in each figure, assessing that the two fields exhibit close values. Those zones presents a point density three to four decades higher than the external point cloud zones.

However, there are differences between the six high-density cloud points (dark red to black for the first picture row, orange to yellow for the second row and orange to dark red for the third row). In the case of stress-fitted models, the origin of the dense cloud point, with DDI strain energy density values close to zero, seem not to match with the origin of the axis, meaning that a systematic error on the stress field can exist at low DDI strain energy density values.

The strain energy density-fitted models exhibit again more upright dense cloud points, located close to the ordinate axis, with an origin located on the axis origin. This representation shows that fitting on strain energy density might be more precise than fitting on stresses.

6.2.3 Comparison with reference fields

The major benefit of testing this identification method on synthetic data is the availability of "reference" fields, calculated by finite element simulation. This section is dedicated to the comparison between fitted model fields and reference fields.

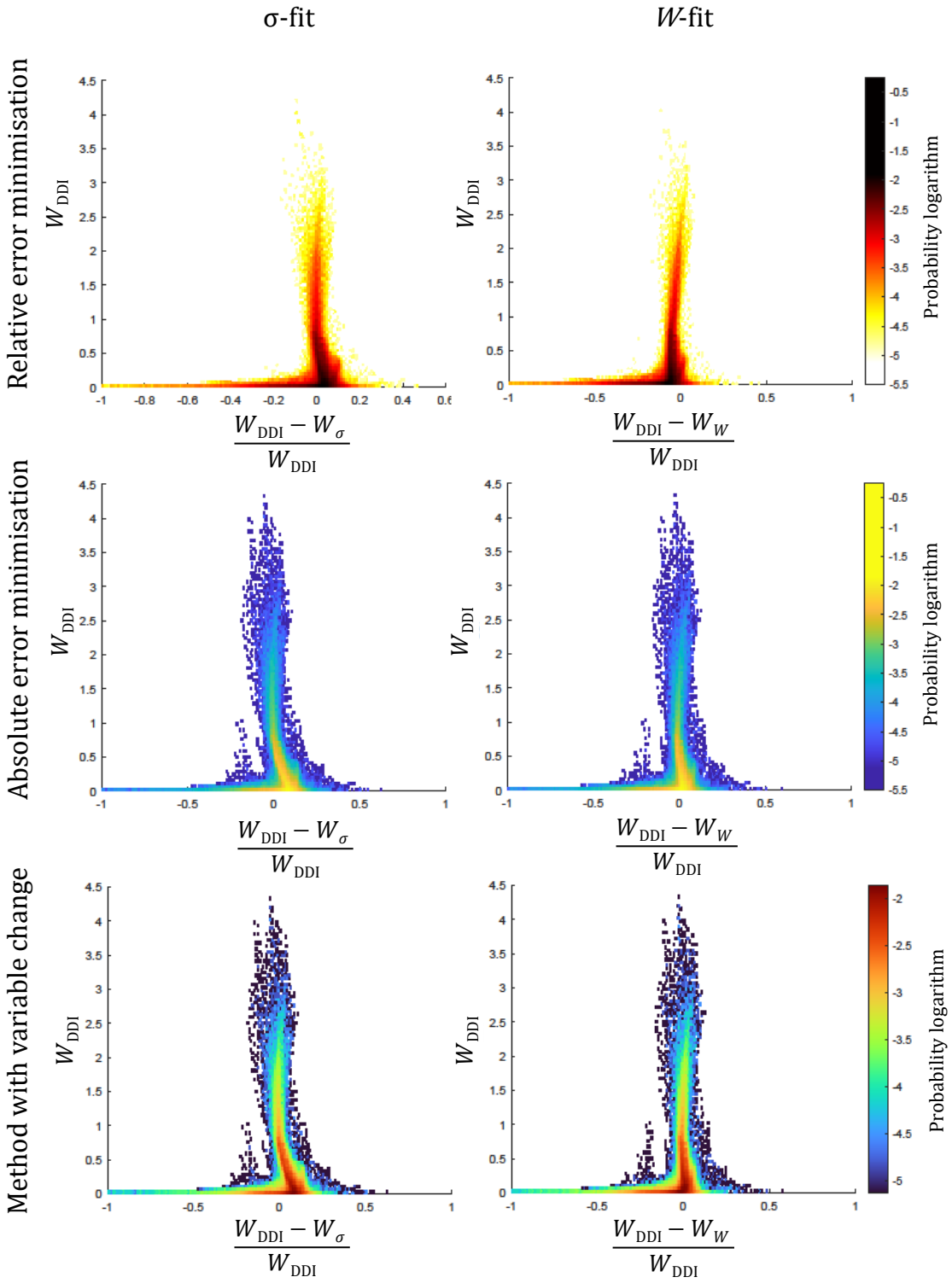

Figure 6.5: Comparison of strain energy density fields between fitted models and DDI results. The first column indicates the method. Each figure presents the relative error between the DDI and fitted models' strain energy density fields.

6.2.3.1 Comparison with reference stress field

Figure 6.6 presents the comparison between fitted models and reference stress fields. Each figure presents the relative error between the spherical part of the tensors on the left and

the relative error between the Von Mises norms on the right.

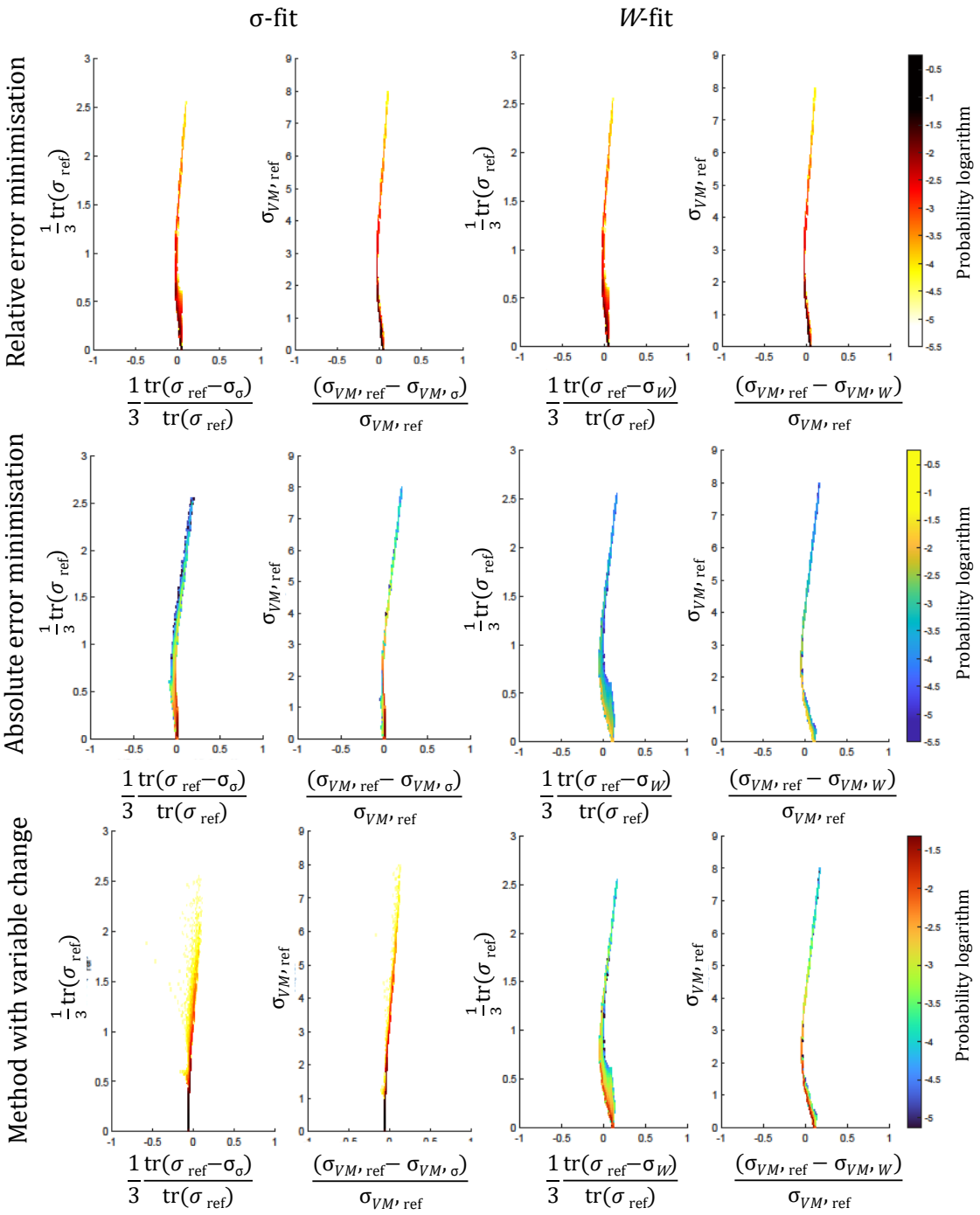

Figure 6.6: Comparison of stress fields between fitted models and FE reference solution. The first column indicates the method. Each figure presents a left plot representing the relative error between the spherical part of the stress tensors, and a left plot representing the relative error between the Von Mises norm of the stress tensors.

The six figures present a significantly smaller scattering than the DDI-fit comparative figures. The fitted models appear to match the reference data with more accuracy than DDI. Here, the six models have filtered the scattering observed amongst DDI data in Figure 6.3. Again, the spherical tensor part-related figures (on the left of the plots)

present a wider scatter than the plots related to the Von Mises norm. Once again, it is a consequence of the incompressibility (see above).

The relative-error minimisation method with a fit on strain energy density seems to generate more scattering than the other five methods at large reference values, giving the top right figures a firework look. The third method, absolute error minimisation with variable change, exhibits again the most upright and zero-centred dense cloud. This method seems to be the most promising one among the six.

6.2.3.2 Comparison with reference strain energy density field

Figure 6.7 presents the comparison between fitted models and reference strain energy density fields, using the visualisation tool presented in Section 6.1.3.

The six figures present thin and upright point clouds, differing by their general shape (straight or curved) and the position of the lowest point of the point cloud (aligned with axis origin or not).

The three stress-fitted models present a curved form and a point cloud origin which is not aligned with the axis origin. The two absolute error and stress-fitted models display a similar curvature; the relative error and stress-fitted models are more upright and closer to the ordinate axis.

The relative error and strain energy density fitted model (top right figure) presents a scatter at large reference values (firework shape) and the origin of its dense cloud point does not match with the axis origin. This model seems not to be the best fitting to our "numerical material". The absolute error and strain energy density-fitted model presents a limited curvature and a reduced scattering; whereas the absolute error with variable change and strain energy density fitted model (bottom right figure) presents a more upright point cloud with a very limited scattering. Its dense point cloud origin matches the axis origin. It is the best matching model in this comparison with reference data.

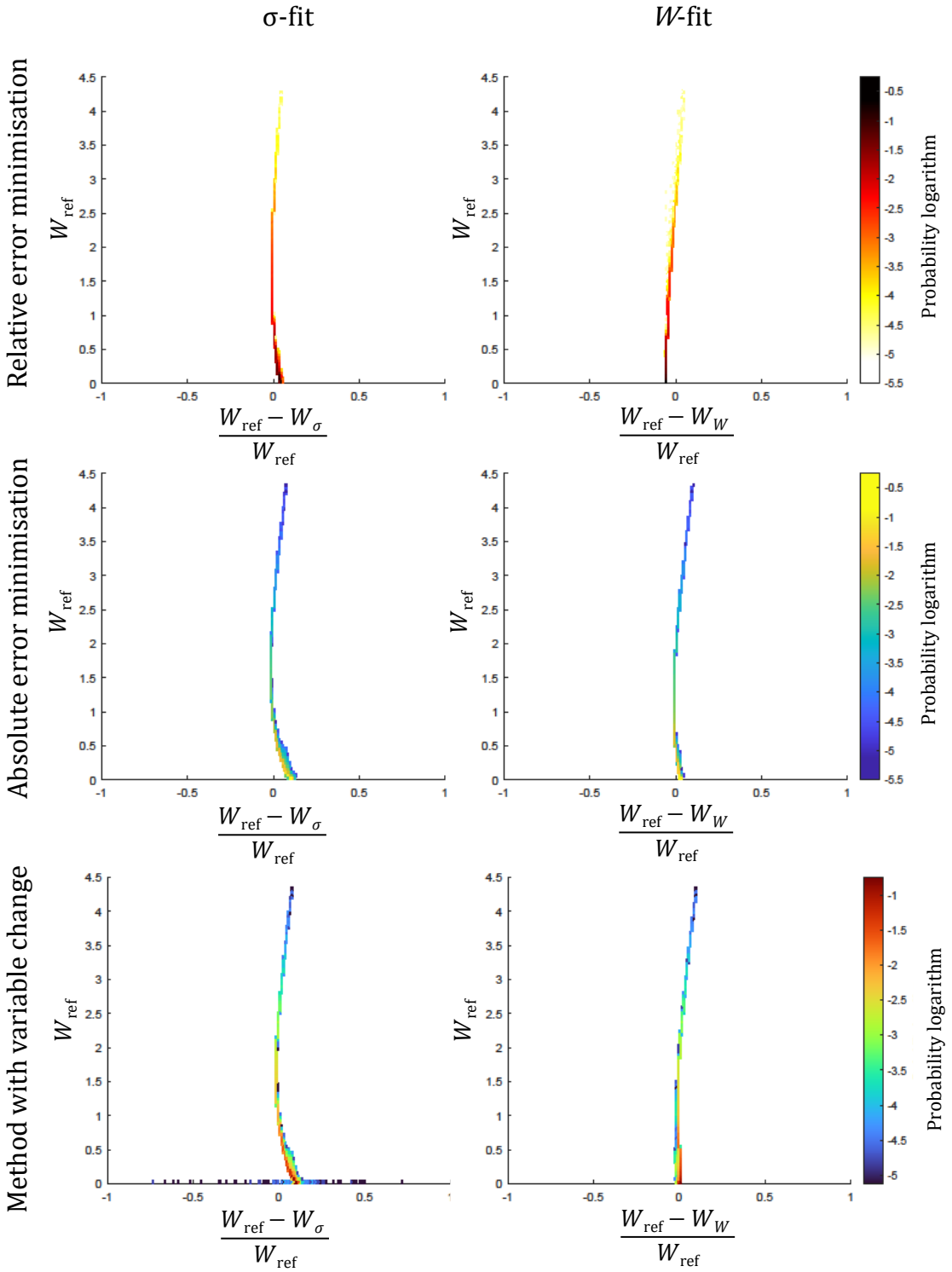

Figure 6.7: Comparison of strain energy density fields between fitted models and FE reference solution. The first column indicates the method. Each figure presents the relative error between the reference and fitted models' strain energy density fields.

6.2.4 Evaluation of two models on simple deformation states experiments

A different validation approach has been conducted on the two absolute errors with variable change models. This "evaluation" is inspired by the classical identification method, described in Section 1.2, which is based on simple deformation states experiments, and is used to extrapolate the material behaviour at complex deformation states, using the fitted model. Considering that the DDMI approach is based on multiaxial experiments, the fitted models are evaluated on simple deformation states experiments, reversing the concept of the classical identification method. The models have been evaluated based on the stretch ratios achieved in Treloar's experiments [90]. The comparison of their shear modulus, calculated according to Eq. (3.2), and presented in Tables 6.1, 6.2, and 6.3 shows that the W-fitted models are more likely to restitute the original shear modulus than the σ-fitted models. Figure 6.8 presents synthetic uniaxial tension curves corresponding to the different fitted models.

From a global perspective, both models successfully reproduce the material response for the range of stretch ratios used in the identification process. However, there is a discrepancy in the case of uniaxial tension for stretch ratios greater than 4, specifically corresponding to $K_2 > 1.7$. By examining Figs. 4.8 and 4.10, it is evident that there are very few data points in this region. As a result, these points have minimal impact on the objective function.

However, it is important to note that the extrapolated portions of the curves deviate significantly from the initial model, regardless of the experiment. This observation is a common phenomenon in hyperelasticity. It is widely recognised that accurately predicting the large strain response of elastomers requires relevant data points for model fitting.

Finally, it is worth noting that the small strain predictions in both planar and equibiaxial tension experiments exhibit excellent agreement for the model identified using the strain energy density field. However, the stress-fitted model shows relatively poorer agreement in these cases.

6.2.5 Conclusions on the methods applied to synthetic data

Three distinct methods have been investigated on synthetic data. As detailed in the previous sections, the models that reproduce the "numerical material" behaviour the best are the models fitted on strain energy density. It seems that by considering the strain energy density, the identification process becomes less biased towards uniaxial tension data, which typically provides a large number of data points. Strain energy density balances the stress field with the strain field. This mitigates the potential dominance of a single mode of deformation and allows for a more balanced and robust identification of the material response.

Differences in convenience have also been noted amongst the methods. The relative-error-based method generates more scattering in comparison with reference data. Both relative-error and absolute error-based methods had a strong tendency to generate non-admissible parameters. Numerous optimisation starting points had to be tested to finally fit an admissible parameter set. This complicates the application of the method and increases the computing time. Yet, the variable change significantly simplifies the process, and the third method, based on absolute error and written with variable change, has been

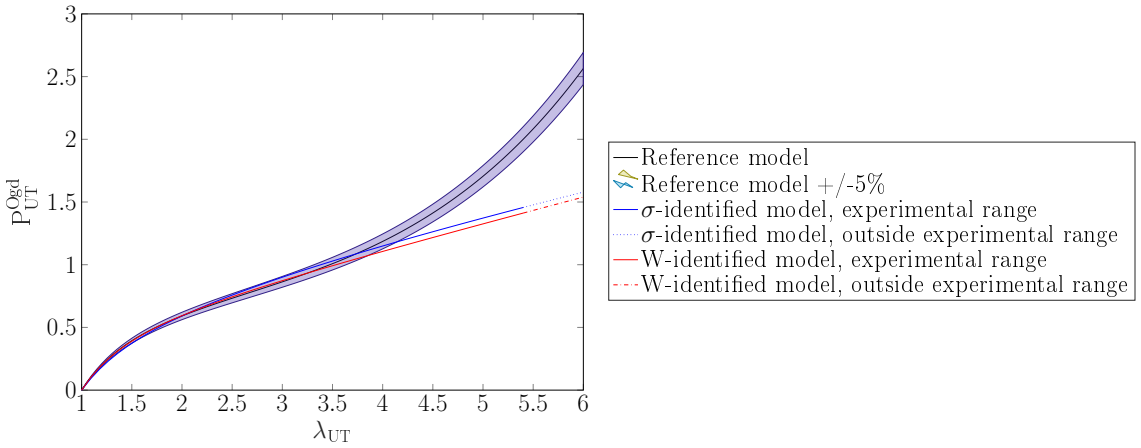

(a) Uniaxial Tension

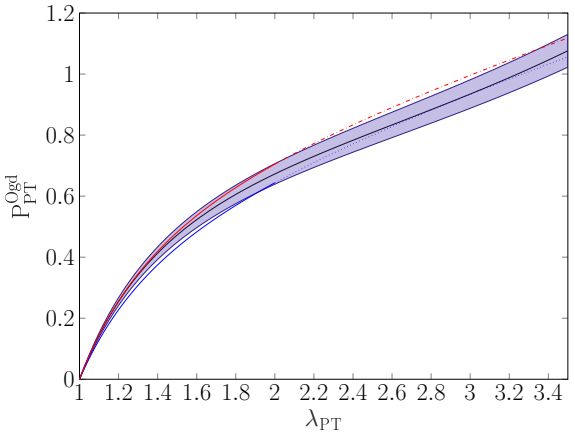

(b) Planar Tension

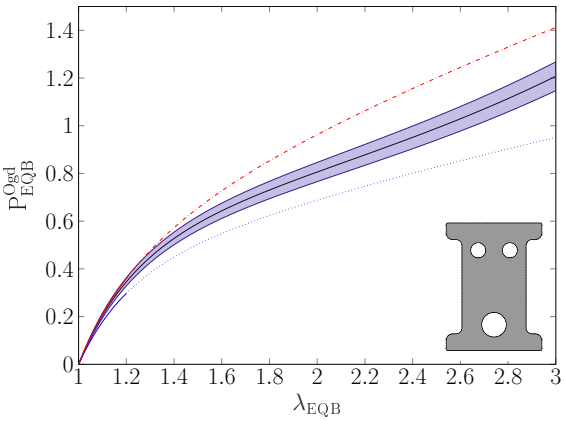

(c) Equibiaxial Tension

Figure 6.8: Accuracy of the models for the three simple experiments: nominal stress vs. largest stretch ratio for (a) uniaxial tension, (b) planar tension, and (c) equibiaxial tension. The initial model is represented by a black continuous line, and the corresponding stress values are depicted by a sky-blue surface with a tolerance of ±5%. For each identified model, represented by blue (identified with $\boldsymbol{\sigma}_{\mathrm{DDI}}$) and red (identified with W_{DDI}), the solid line illustrates the model response at stretch ratios achieved by at least one finite element during the heterogeneous test. The dashed and dotted lines are used for extrapolation beyond the tested range.

the most convenient and most efficient method of the three.

After testing the six methods on synthetic data, DDMI is tested on experimental data, using the strain energy density and absolute error with the variable change method.

6.3 Application to real experimental tests

Once DDMI has been proven efficient on synthetic data, we can now apply it on experimental data. The chosen test and its parameters are described in the following.

6.3.1 Experimental methods

6.3.1.1 Experimental data

The experimental dataset chosen for this application of DDMI on experimental data is described in Table 3.4 and corresponds to the sample ANR 3.1. It corresponds to the slower experimental test. The corresponding DDI strain energy density field is presented in Figure 5.7.

6.3.1.2 Models and fitting methods

Two models have been fitted on the DDI strain energy density field:

- a three-term Ogden model, using absolute error with variable change objective function as described in Section 6.1.2.3,
- a Yeoh model, described by Eq. (1.7), because it is one of the models fitted on the uniaxial tension curves of the carbon-black filled SBR which presented a good agreement with the experimental data. This Abaqus-fitted model will be used as a comparison with the DDMI-fitted models.

The two models' energetic formulations are recalled below:

$$W = \sum_{n=1}^{N} \frac{2\mu_n}{\alpha_n^2} \left(\lambda_1^{\alpha_n} + \lambda_2^{\alpha_n} + \lambda_3^{\alpha_n} - 3\right),$$

describing Ogden model, with α_i, and μ_i being the parameters of the model and

$$W = \sum_{i=1}^{3} C_{i0} \left(I_1 - 3\right)^i,$$

describing Yeph model, C_{i0} being the parameters of the model.

6.3.1.3 Validation path

Working with experimental data means that reference data is not available, and other "control points" have to be defined to assess the efficiency of the method. First, fitted models stress and strain energy density fields will be compared with DDI data using the visualisation tool developed in Section 6.1.3. These figures will be compared to the ones obtained with synthetic data, to qualitatively evaluate the influence of the use of experimental data. Second, the fitted models are compared with uniaxial tension data, reversing the classical identification process. Finally, DDI data is compared to uniaxial tension data to explain the differences that can be observed between the Abaqus-fitted model and the DDMI-fitted models.

6.3.2 Results

This section is dedicated to the presentation of the results of DDMI applied to experimental data. The fitted-models strain energy density fields are compared with DDI fields in the following.

6.3.2.1 Ogden model

The first fitting procedure conducted with DDI experimental data is set to fit a three-term Ogden model [71]. The fitted parameters are given in Table 6.4.

Parameters	μ_1 (Pa)	μ_2 (Pa)	μ_3 (Pa)	α_1	α_2	α_3
Values	3.76×10^6	1.72×10^6	-2.34×10^6	1.96×10^{-9}	3.70×10^{-9}	-1.35

Table 6.4: Parameters of the three-term Ogden model fitted on DDI experimental data.

This model's corresponding strain energy density field is compared with DDI data using the visualisation tool presented in Section 6.1.3. Figure 6.9 presents the absolute and relative error between the model's strain energy density and DDI strain energy density as a function of W_{DDI}.

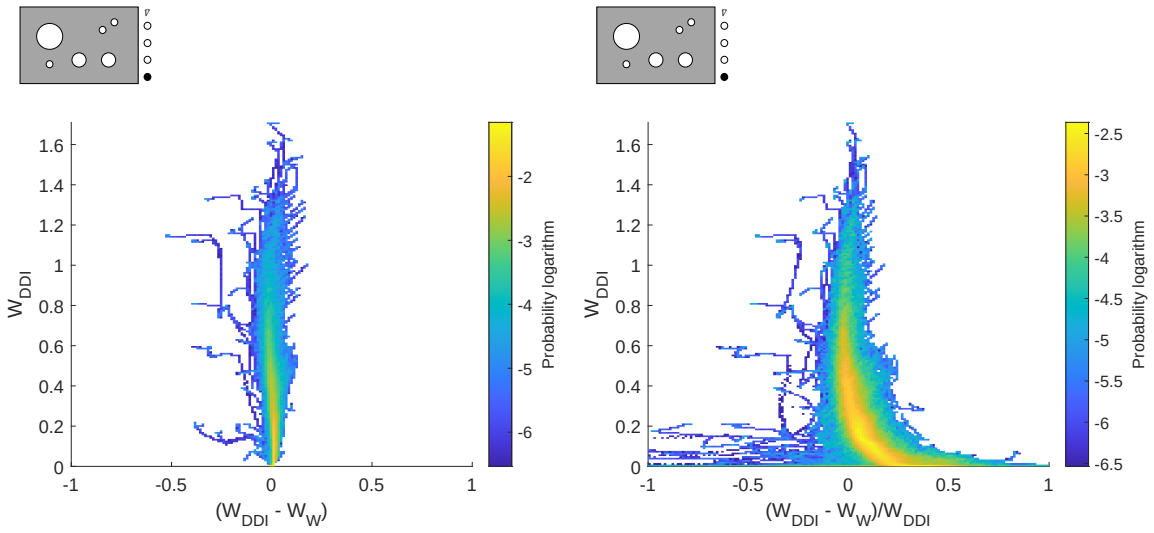

(a) Vertical plot with absolute error

(b) Vertical plot with relative error

Figure 6.9: Comparison between fitted Ogden model strain energy density field and DDI strain energy density field.

The absolute error plot, on the left-hand side of the figure, presents a vertical point cloud, centered on a null error, with highly dense areas located along the ordinate axis. The majority of the points are located along the ordinate axis, meaning that the absolute error is low for the majority of points. Some points are diverging away from the rest of the point cloud, leading to the blue slopes that can be observed in both left-handside and right-handside plots. The right-hand side plot, showing the relative error between the DDI and fitted strain energy density field, exhibits a larger point cloud, especially at the bottom of the plot where the majority of points, yellow and orange areas, is diverging towards the right side of the plot, meaning that DDI strain energy density values tend to be higher than the corresponding fitted strain energy density, for small strain energy density values. DDI may overestimate these small strain energy density values. Overall, the middle to the upper part of the plot is well-centred on the ordinate axis, confirming the observations made on the left-hand side plot. Additionnaly, the absolute error plot of Figure 6.9 (a) is filtred to focus on the denser areas of the plot. The result is shown in Figure 6.10. The plane section representing a number of points corresponding to a

hundreth of the point number of the densest area or less are removed. Only 4% of the data is removed. The resulting density plot is an upright form, centered on the ordinate axis. This figure shows the accuracy of the fitted model for representing the experimental data.

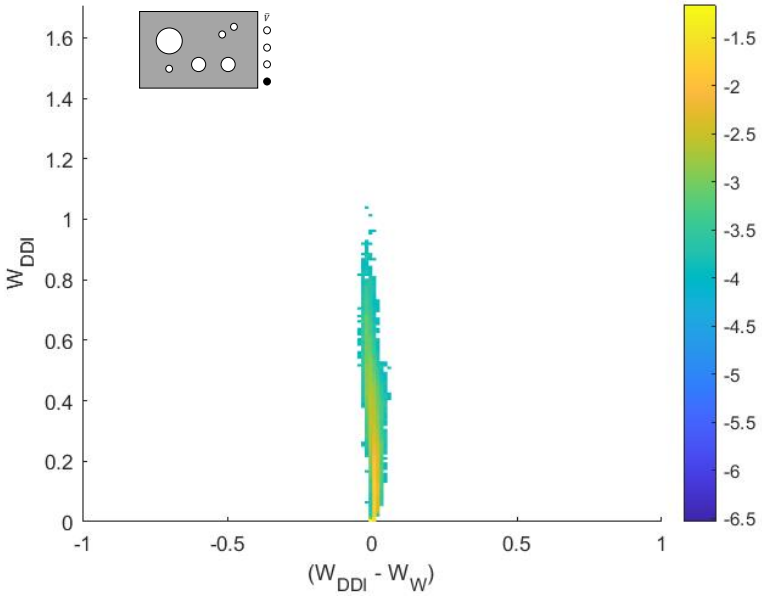

Figure 6.10: Comparison between fitted Ogden model strain energy density field and DDI strain energy density field: absolute error display. The data is filtred. The plane sections representing more than a hundredth of the densest plane section are represented. Only 4% of the data points are removed.

6.3.2.2 Yeoh model

The second fitting procedure with DDI experimental data is set to fit Yeoh's model [102]. The fitted parameters are given in Table 6.5.

Parameter	C_{10}	C_{20}	C_{30}
Value (MPa)	0.745	-0.191	0.0341

Table 6.5: Parameters of the Yeoh model fitted on DDI experimental strain energy density field.

Figure 6.11 presents the comparison of the fitted Yeoh model strain energy density field and DDI strain energy density field.

The left-handside plot presents the absolute error while the right-handside plot presents the relative error. The observations made in Figure 6.9 apply to this figure as well, because both figures exhibit the same characteristics. It can be noted that both figures look like the plot presented for numerical data in Figure 6.5, but with the characteristic diverging at the bottom of the plot. Both models seem well fitted considering that the majority of points are located close to the ordinate axis. Additionnaly, the absolute error plot of Figure 6.11 (a) is filtred to focus on the denser areas of the plot. The result

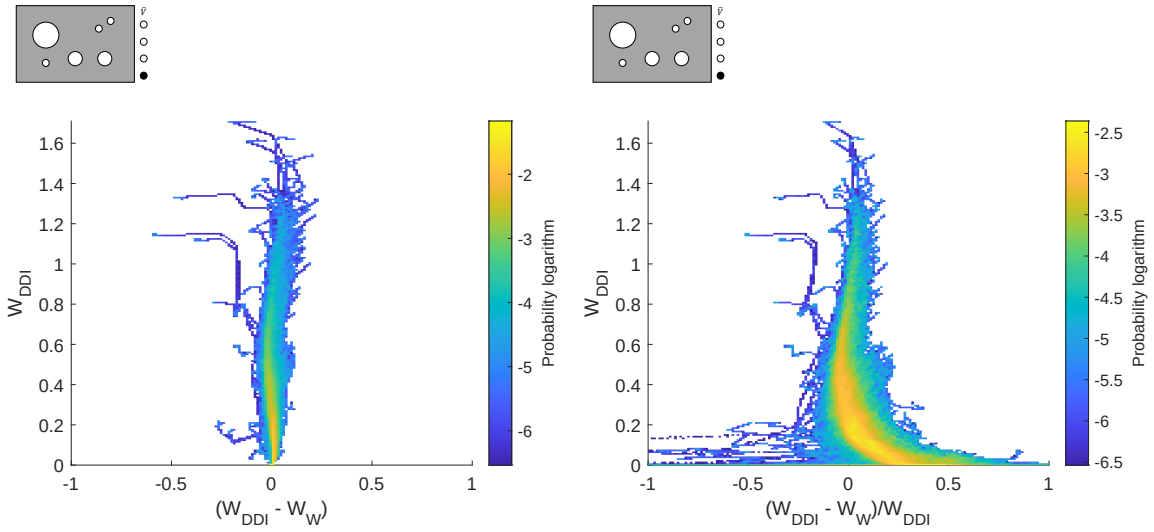

(a) Vertical plot with absolute error

(b) Vertical plot with relative error

Figure 6.11: Comparison between fitted Yeoh model strain energy density field and DDI strain energy density field.

is shown in Figure 6.12. The plane section representing a number of points corresponding to a hundreth of the point number of the densest area or less are removed. Only 4% of the data is removed. The resulting density plot is an upright form, centered on the ordinate axis. A slight bend can be observed, meaning that the model seem to slightly over-estimate some of the strain energy density values and under-estimate others. This figure shows again the accuracy of the fitted model for representing the experimental data.

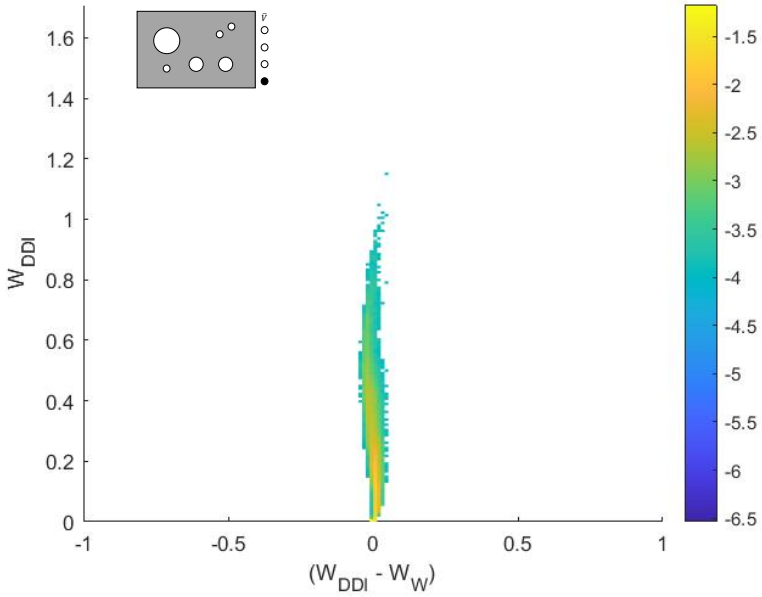

Figure 6.12: Comparison between fitted Yeoh model strain energy density field and DDI strain energy density field: absolute error display. The data is filtred. The plane sections representing more than a hundredth of the densest plane section are represented. Only 4% of the data points are removed.

6.3.3 Discussion

DDMI has been applied to experimental data. Two models were successfully fitted to experimental data through the DDMI procedure. They have to be compared to other material data to investigate their capacity to predict the material behaviour.

The initial shear modulus of the two DDMI-fitted models and the Abaqus-fitted model described in Section 2.2.3 are calculated according to EQs. (3.2) and (2.10) and presented in Table 6.6.

Model	Abaqus-fitted Yeoh	DDMI-Ogden	DDMI-Yeoh
Shear modulus (MPa)	1.87	1.57	1.49

Table 6.6: Comparison of the initial shear modulus of the fitted models.

The three shear moduli share the same order of magnitude. However, the two DDMI-fitted models' shear moduli are the closer values, and the modulus of the Abaqus-fitted model is higher.

Figure 6.13 shows two three-dimensional representations of the two DDMI-fitted models as grey surfaces and DDI strain energy density data as black dots. These plots present the DDMI-fitted Ogden plot on the left-hand side of the figure and the DDMI-fitted Yeoh model on the right-hand side plot.

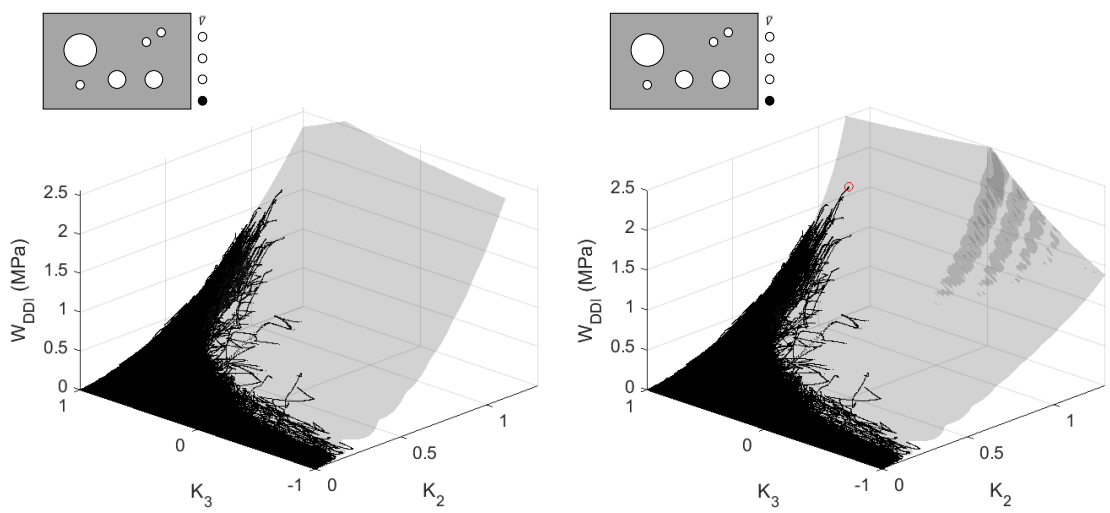

(a) Fitted Ogden model

(b) Fitted Yeoh model

Figure 6.13: Visualisation of fitted models surfaces and DDI strain energy density data as functions of K_2 and K_3.

There is a very good agreement between the DDI data and the model in both cases. The DDI data seems to be laying on both model surfaces, except for some points exhibiting strain energy density values lower than expected, as mentioned in Section 5.2.3. The two models exhibit a different curvature when K_2 increases: the fitted Yeoh model exhibits a stiffer slope than the fitted Ogden model. These curvature differences are observed at K_2 levels that are poorly or not covered by the experimental data on which they have been

fitted: this difference is due to the model formulations. Without further data, we meet one of the limits of every identification method: the model extrapolation on missing data is one possible description of the material behaviour, but we cannot argue that the material behaves like this without further experimental investigation. This difference between the three fitted models is also shown in Figure 6.14.

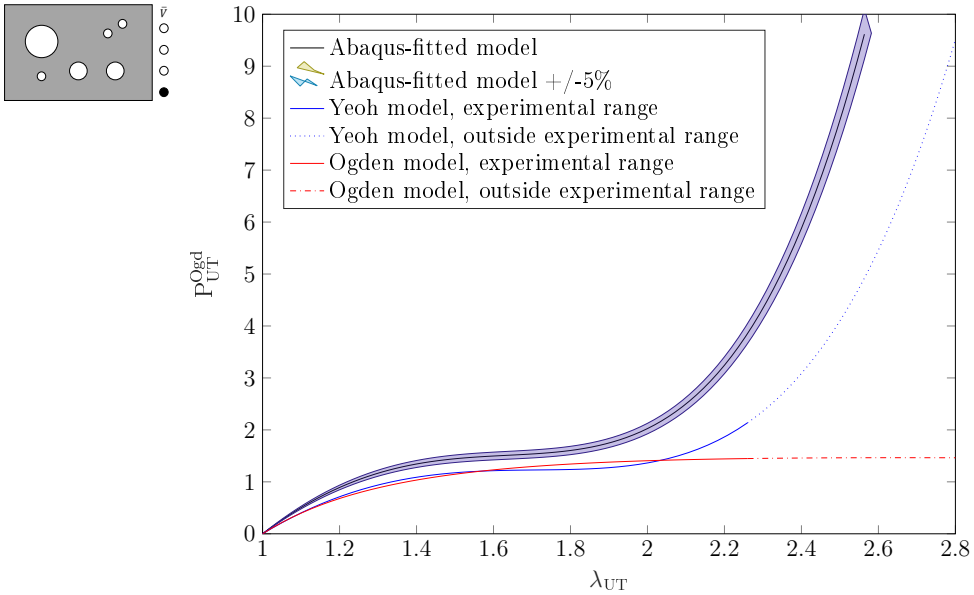

Figure 6.14: Evaluation of fitted models along with the model fitted by Abaqus on uniaxial tension data. This is a projection of the experimental data as seen in Figure 5.7 (b) on the (K_2, W) plane. The dark blue zones represent one point or less.

This figure shows the evaluation of the three fitted models, the Abaqus-fitted Yeoh model and the DDMI-fitted Ogden and Yeoh model, on synthetic uniaxial tension curves. The two DDMI-fitted models are very close to each other in the stretch range corresponding to the experimental data we fit them on, represented by plain lines in the plot. They diverge around $\lambda_{UT} = 2.15$, at stretch levels where the experimental data is scarce. Their slope in the range $\lambda_{UT} \in [2.3, 2.8]$ is very different. The DDI-fitted Ogden model presents a single inflexion. Two of its power parameters, α_1 and α_2 are close and act as a single term, as shown in Table 6.4. The Abaqus-fitted model presents stiffer slopes and is always located above the two others. This model has only been fitted on uniaxial tension data and no other deformation mode. It seems that either the Abaqus-fitted model overestimated stress, or the two DDMI-fitted models underestimated stress. One way to sort this out is to compare DDI data and uniaxial tension data. Figure 6.15 presents the comparison between DDI data, expressed in terms of strain energy density as a function of K_2, and uniaxial tension data.

Experimental data is represented with a density plot, the yellow areas representing the highest density of points, and the uniaxial tension data is presented as a black line. This figure highlights the position of the DDI point cloud compared to the Uniaxial Tension curve: again, the uniaxial tension data is located above the dense DDI point cloud. This could explain the differences observed above between the Abaqus-fitted model and DDMI-fitted models.

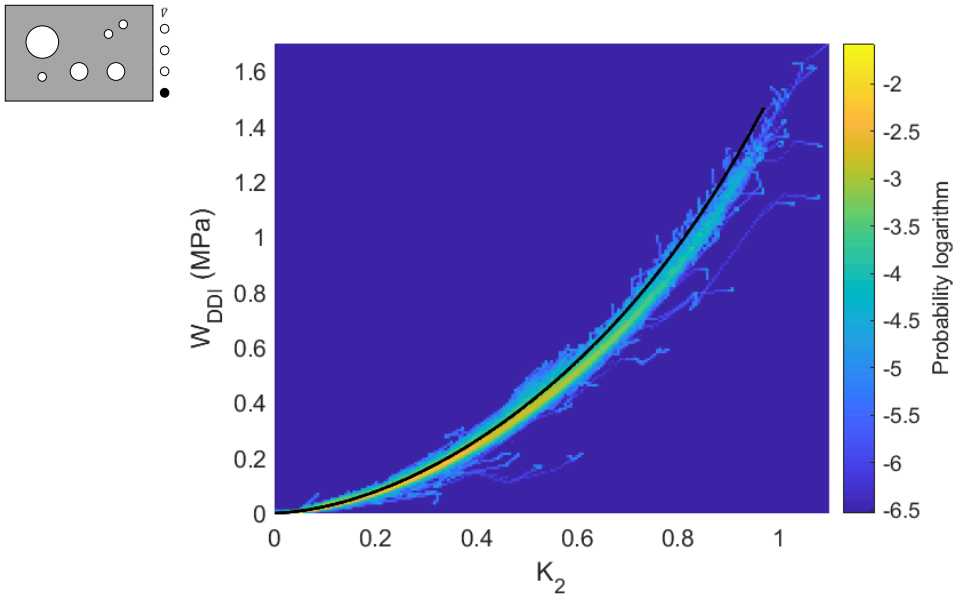

Figure 6.15: Comparison of DDI strain energy density data with Uniaxial Tension data. DDI data is presented as a density plot using the colour bar and the uniaxial tension data is represented by the black line.

6.4 Conclusion

The data-Driven Model Identification method is an innovative identification method to reconciliate models and Data-Driven approaches. This identification method allows the exploration of a large variety of deformation modes and preserves the model choice for the very end of the process, generating a less biased stress field. DDI stress field can be used to calculate a corresponding strain energy density field. Both fields can be used to fit models.

The method has proven its capacity to fit a model which is representative of the entry data, first with synthetic data and then with experimental data. The investigations run with synthetic data highlighted the benefits of fitting models on strain energy density data. The experimental investigations are run with a strain energy density model fit.

DDMI is still limited both by the Data-Driven Identification applications, which are increasing year by year, but also by the classical identification limits, such as data extrapolation for example.

Overall, this method has proven its efficiency for the identification of hyperelastic material models using non-homogeneous tests on elastomeric planar membranes, in both synthetic and experimental cases.

Chapter 7

Sample design for full-field measurement-based identification methods

---

After exploring the identification methods, the kinematic map built in Chapter 4 is used to design samples that maximise "the multiaxiality" of a heterogeneous test. Two metrics are defined:

- a measure of the surface covered by the kinematic map points,
- an entropy measure, describing the scattering of the points on the map.

Twelve sample geometries are proposed. They are based on a 100×65 mm^2 planar carbon-black filled SBR membrane pierced with holes of different sizes. Finite element simulations are run, the corresponding kinematic maps plotted and metrics calculated. The two sample geometries maximising the metrics are chosen to be tested experimentally. Experimental tests are run and kinematic fields are measured with DIC. The experimental kinematic maps are plotted and compared with the ones from finite element simulations.

The experimental maps present smaller surface measurements due to the strip of material that is not considered due to the difficulty of making the DIC mesh match the boundaries of the sample. Their entropy measure is better than the finite element simulations, meaning that there are fewer "hot spots" with a high point density on the experimental kinematic map.

Contents

The design of multiaxial tests for full-field measurement-based methods relies on the choice of the loading conditions and the geometry of the sample. This chapter explores the possibilities to enrich the kinematics of an experiment by modifying the shape of the sample. The kinematic map built in Chapter 4 is used to compare the different proposals.

7.1 Framework

This study was conducted by third-year engineering school students (equivalent to undergraduate Master's students) from Ecole Centrale de Nantes, in the specialty of Materials and Processes. The aim of the study was to optimise the shape of a pierced planar membrane to enhance the heterogeneity of an experimental test designed for identification purpose. Aboth numerical and experimental approach was chosen to allow students to carry on finite element simulations and experimental tests. The goal was to propose samples for enhanced deformation modes and strain magnitude distribution. Carbon-black-filled SBR rubber presented in Chapter 2 is used for this study. Only planar membranes are considered.

7.1.1 Sample base

To be easily reproducible, the samples are designed on a similar basis. They are rectangular-shaped planar membranes of 100×65 mm^2 with 1.6 mm thickness. Holes are punched within the rectangular shape to create a non-heterogenous strain field. Both size and position of these holes influence the strain field.

The hole punchers used are shown in Figure 7.1.

Figure 7.1: Hole punchers available for sample design. The diameters vary from 3 to 30 mm.

Fifteen sizes are available, with diameters from 3 to 30 mm. The pressure required for cutting is applied manually, using a lever mechanism similar to that used on drill presses. These conditions meet the requirement of a reproducible and accessible sample-cutting process. The different sample designs are meshed and a FE model is built accordingly to reproduce the loading conditions.

7.1.2 Experiment

The experiment chosen to test the different designs of samples is presented in Chapter 3. It is applied on the samples with the chosen velocity $\bar{V} = 0.05$ mm.s^{-1}. The experimental tests are run on the hexapod device, using the test bench described also in Chapter 3.

Numerical simulations are run using Abaqus CAE software [30]. The "numerical material" is modelled with the Yeoh model [102], defined by Eq. (1.7), whose coefficients have been determined by Abaqus using uniaxial tension data. The model is described in Table 2.6. Once the simulations run, metrics are calculated and used to compare the different designs.

7.1.3 Metrics

Metrics are scalar quantities considered relevant for the choice of the sample geometries. They are derived to choose the sample that maximises the "multiaxiality" of a given test. Figure 7.2 is used to define the two metrics used to compare sample designs.

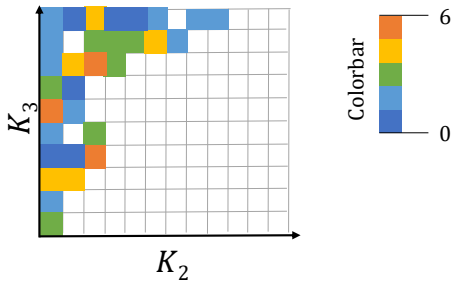

Figure 7.2: Kinematic map example for metrics definition.

- The first metric considered is a measure of the surface occupied by the kinematics map points. This metric is calculated by counting the number of non-zero squares in the partition of the (K_2, K_3) plane. This measure can be compared between the different sample geometries because the size of the partition squares is fixed among the experiments. For example, referring to Figure 7.2, the surface is constituted of 6 dark blue squares, 10 light blue, 7 green, 5 yellow and 3 orange. We have $S = 31$.

- The second metric is an entropy measure. It is calculated as:

$$E = -\sum_{K_2,K_3} p \ln p, \tag{7.1}$$

using the kinematics map. Here, p stands for the probability corresponding to a given (K_2, K_3) point of the kinematic map. This metric measures the regularity of the point's spreading across the (K_2, K_3) plane. Any concentration of points will make the entropy drop. For the kinematic map presented in Figure 7.2, we have:

$$N_{\text{points}} = 6 \times 1 + 10 \times 2 + 7 \times 3 + 5 \times 4 + 3 \times 5 = 82, \tag{7.2}$$

so the probability associated with each square is $\frac{1}{82}$ for dark blue squares, $\frac{2}{82}$ for light blue, $\frac{3}{82}$ for green, $\frac{4}{82}$ for yellow and $\frac{5}{82}$ for orange. The entropy associated with this heatmap is:

$$E = -\sum_S p \ln p$$
$$= -6 \times \left[\frac{1}{82} \ln\left(\frac{1}{82}\right)\right] - 10 \times \left[\frac{2}{82} \ln\left(\frac{2}{82}\right)\right] - 7 \times \left[\frac{3}{82} \ln\left(\frac{3}{82}\right)\right]$$
$$- 5 \times \left[\frac{4}{82} \ln\left(\frac{4}{82}\right)\right] - 3 \times \left[\frac{5}{82} \ln\left(\frac{5}{82}\right)\right] = 3.32. \quad (7.3)$$

Remark: The entropy value variation is illustrated in Figure 7.3. The blue dotted line represents $-p \ln p$ as a function of the probability value p between 0 and 1. The maximum of this function is located around $p = 0.37$. However, the entropy is calculated using every point of the kinematic map. Let us consider fictive situations where all the points of the map have the same probability p. Their number is then a $N = \frac{1}{p}$. Therefore, $E = -\frac{1}{p} p \ln p = -\ln p$. 200 of these fictive situations are represented by round red markers. This illustrates that the entropy increases with a more evenly distributed map instead of several concentrated areas.

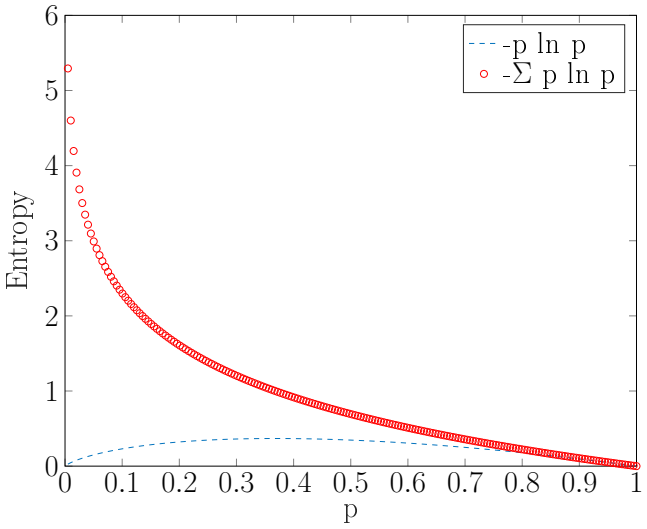

Figure 7.3: Entropy metrics visualisation. The blue dotted line represents the value of $-p \ln p$ for given probability values, and the red round markers represent $-\sum p \ln p$ for a dataset where every point has an equal probability value p.

Other metrics could have been chosen, such as the average maximum K_2 for each layer of K_3, representing the maximum strain magnitude reached to a given close group of deformation modes.

Other methods exist and have been developed to optimise sample shape to maximise a metric: shape optimisation procedures. They are based on an objective function to maximise or minimise and a series of constraints [10]. They can be used to design heterogeneous interior notched specimens for material mechanical characterisation [21]; or to maximise the heterogeneity of the strain and stress states using topology optimisation [7]. Those methods were not explored here because the resulting designs usually require specific cutting tools to realise the notches or specifically designed holes.

7.2 Designs and simulation results

Once the methods and metrics are defined, several sample geometries are investigated. Their geometry is designed using GMSH [39] and then used in finite element calculations and the corresponding kinematic map is plotted. Metrics are then calculated and compared to choose the geometries that will undergo experimental testing.

7.2.1 Designs

Twelve geometries are considered for the test phase. They are shown in Figure 7.4.

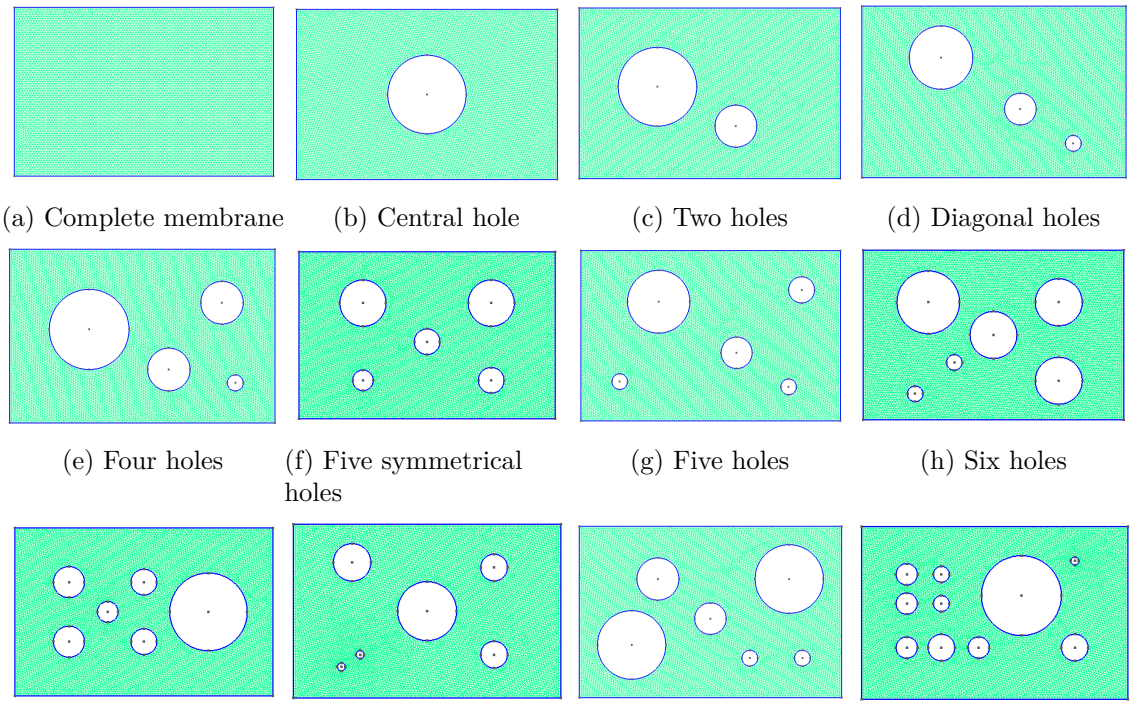

(a) Complete membrane (b) Central hole (c) Two holes (d) Diagonal holes

(e) Four holes (f) Five symmetrical holes (g) Five holes (h) Six holes

(i) Six holes with one bigger (j) Six medium holes (k) Six holes with two bigger ones (l) Ten holes

Figure 7.4: Sample geometries for FE simulations.

The number of holes varies from zero to ten, with different positions:

- no hole or a unique hole, for samples (a) and (b),
- a few holes of different sizes to trigger mixed deformation modes between the holes, for samples (c) to (g),
- and several holes with close positions for samples (h) to (l).

7.2.2 Kinematic maps

Kinematic maps are plotted for each sample geometry, and corresponding metrics are calculated. Two of them are presented in Figure 7.5: sample (c) on the left-handside and sample (f) on the right-handside.

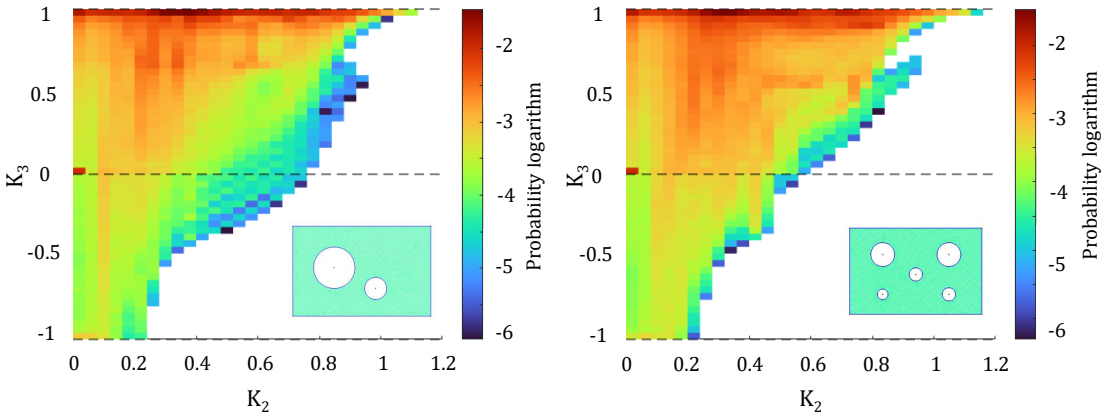

Figure 7.5: Kinematic maps of two sample geometries. Left: sample (c). Right: sample (f).

The two kinematic maps admit a large surface, covering the K_3 axis integrally, meaning that all deformation modes are triggered by the experiment. The highest strain levels are reached in uniaxial tension for both samples. Sample (f) presents a highly distributed map, with a large area covered by the warm colours of the colour map. The sample (c) presents a less distributed map, with denser areas located in the top half of the map. Both maps present their maximal point density in uniaxial tension and a concentration around $K_3 = 0$ and $K_2 \approx 0$.

Similarily than in experimental maps presented in Chapter 4, it seems easier to fill up the upper half of the map, between planar tension and uniaxial tension deformation modes, than the lower half of the map, and especially the deformation modes close to equibiaxial tension. The classical way to trigger this deformation mode is either by inflating a membrane or using a specific machine with two clamping jaw pairs positioned perpendicularly [60]. Neither the experimental setup nor the chosen loading corresponds to these two methods. It explains the difficulty encountered to trigger equibiaxial tension with larger strain during the tests.

7.2.3 Metrics comparison

The two metrics are calculated for the twelve proposed designs. The results are presented in Table 7.1.

Sample	(a)	(b)	(c)	(d)	(e)	(f)	(g)	(h)	(i)	(j)	(k)	(l)
Surface S	651	789	**828**	795	748	762	787	788	738	803	777	742
$S/S_{\max}$ (%)	78.6	95.3	100	96.0	90.3	92.0	95.1	95.2	89.1	97.0	93.8	89.6
Entropy E	2.42	2.39	2.43	2.45	2.40	**2.47**	2.45	2.36	2.44	2.45	2.40	2.38
$E/E_{\max}$ (%)	98.0	96.8	98.4	99.2	97.7	100	99.2	95.6	98.8	99.2	97.2	96.4

Table 7.1: Metrics values for the twelve samples of Figure 7.4. The highest values of each metric is highlighted.

The surface values vary between 651 and 828, with an average value of 767.33 and a median of 782. Half of the designs obtain a surface value between 750 and 800. The sample with the largest surface measure is sample (c), designed with two holes of different

diameters. The entropy values vary between 2.36 and 2.47, with an average value of 2.42 and a median of 2.425. This presents a tight standard deviation. The sample with the greatest entropy measure is the sample (f), designed with five holes arranged symmetrically. The two samples that maximise the metrics are chosen for experimental tests.

7.3 Experimental results

The two selected sample geometries are tested experimentally. The tests are run on the hexapod test bench. Experimental results are presented in the following.

7.3.1 Samples and experimental conditions

Samples (c) and (f) have been chosen for the experiments. Two samples (c) are tested to ensure the consistency of the results: sample ANR 2.3 and ANR 3.3. The geometry (f) is made on the sample ANR 3.2. Holes are punched into 100×65 mm^2 planar membranes. A speckle pattern is applied with white paint. The final samples are shown in Figure 7.6.

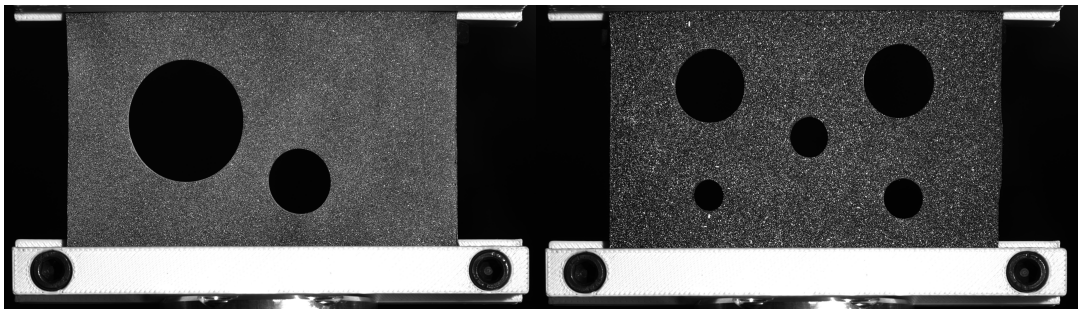

Figure 7.6: Experimental samples for improving deformation modes and diversity. On the left-hand side Sample (c): ANR2.3, is presented and Sample (f): ANR3.2 in the right-hand side. A speckle pattern has been applied with white paint for Digital Image Correlation purposes. The samples are clamped in the experimental setup.

The three tests are recorded using an optical camera. FE-DIC is applied for kinematic field measurement. Table 7.2 presents the DIC parameters of the three tests. The other DIC parameters are presented in Table 3.3. The picture rate is 0.66 Hz, and the exposure time is 8000 μs.

Sample	Time steps	Mesh nodes	Mesh elements
ANR 2.3, design (c)	518	2122	3987
ANR 3.3, design (c)	521	2428	4509
ANR 3.2, design (f)	533	2260	4222

Table 7.2: Tests parameters.

7.3.2 Experimental kinematic maps

The three corresponding experimental kinematic maps are presented in Figure 7.7.

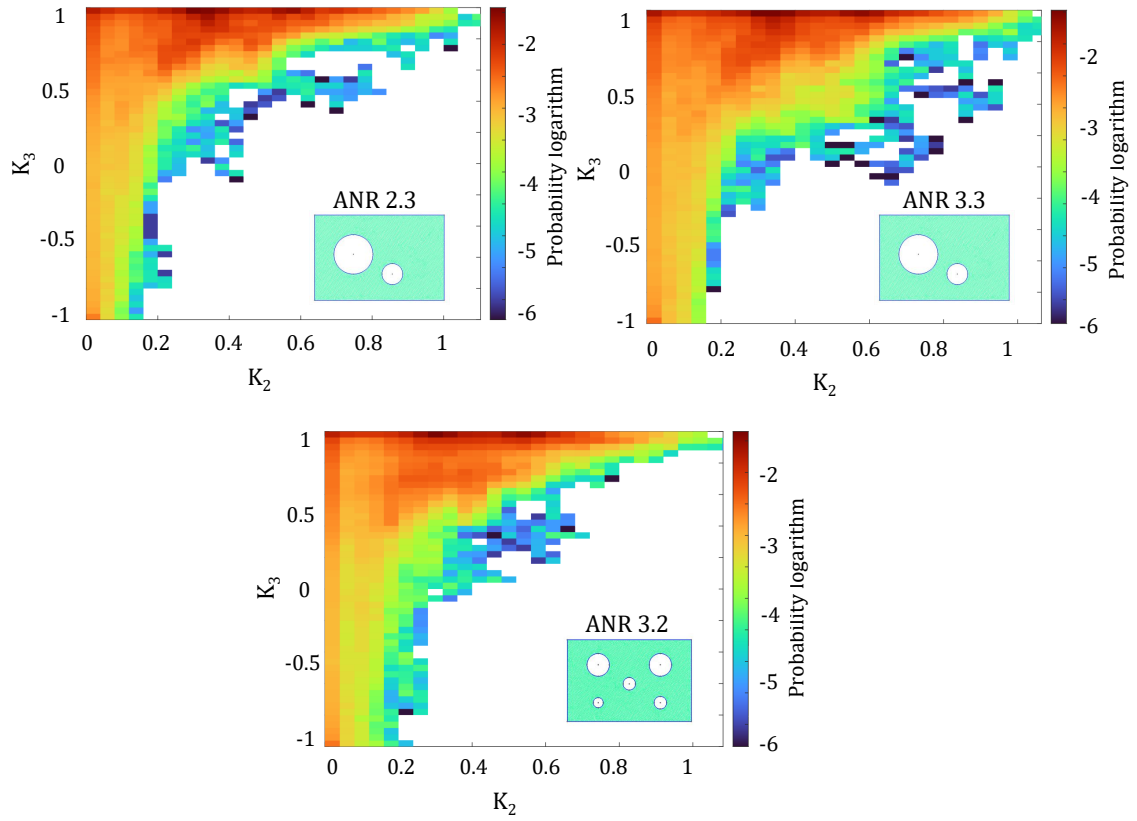

Figure 7.7: Experimental kinematic maps obtained for samples (c) and (f). Geometry (c) (top figures) is tested twice to check reproducibility.

The two upper pictures correspond to the geometry (c) and the third one to the geometry (f), as represented by the miniature icons. The two upper samples have a similar high-density surface, represented by the red and dark orange areas. However, the low-density surface, represented by the blue to yellow areas is different. The second sample, ANR 3.1, presents a larger surface. The three kinematic maps present a sample response fully covering the K_3 axis, and variable K_2 maximum values reached for each deformation mode. Uniaxial tension remains the deformation mode reaching the largest strain magnitudes, around $K_2 = 1.2$. The kinematic maps of the two samples (c) present the same dense areas, located close to $K_3 = 1$ and in the region limited by $K_2 \in [0.2; 0.5]$ and $K_3 \in [0.6; 1]$. Their difference is highlighted in Figure 7.8. This figure is built by superimposing the two kinematic maps: sample ANR 3.3 kinematic map is placed below, with a grey level colourmap, while sample ANR 2.3 kinematic map is plotted above to highlight the differences of coverage. This figure shows that the difference in covered surface represent a relatively small portion or surface. The second highlight of this figure comes from colourmaps. The only parts of ANR 3.3 kinematic map that are visible on the superimposed figure correspond to sparse areas, which do not represent a large amount of points. The majority of points seem located in the common area of the two kinematic maps.

These experimental kinematic maps can be compared qualitatively with the finite element kinematic maps presented in Figure 7.5. The experimental map surface seems smaller than the ones exhibited by FE simulation maps, especially for K_3 values between -0.2 and 0.6. The DIC technique can explain this discrepancy. When setting up the

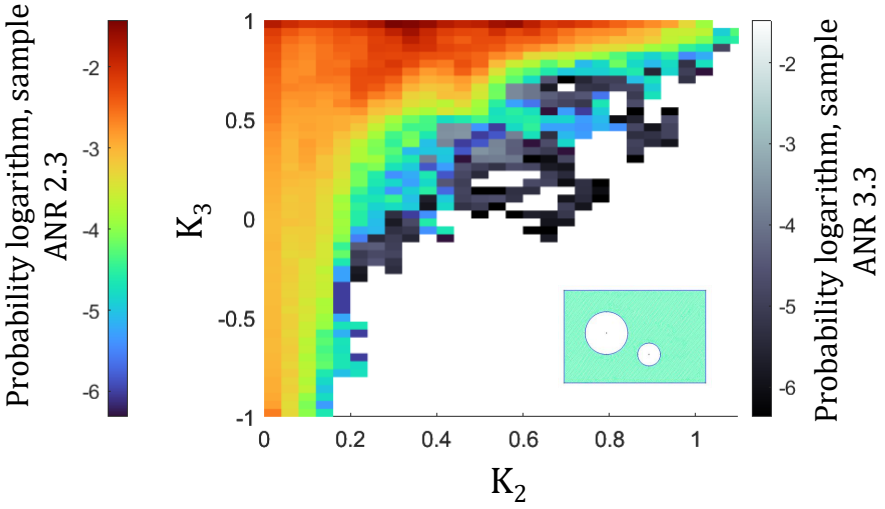

Figure 7.8: Superimposition of the two kinematic maps of the (c) samples. The sample ANR 3.3 is presented in grey levels while the sample ANR 2.3 is presented in colours.

mesh for the FE-DIC process, it is difficult to make the boundaries of the mesh match the boundaries of the sample. Most of the time, the mesh lacks a piece of material around the holes and outer boundaries. Yet these pieces of material are submitted to potential large strain magnitudes, with the stress concentration role of the holes, or mixed modes when two close holes influence the behaviour of a piece of material located in-between. This results in a less heterogeneous kinematic map. Overall, the dense regions of the synthetic maps corresponds to the dense areas of the experimental maps. The major differences are observed in sparser regions of the maps, highlighting that the majority of points of experimental maps, presented in warm colours on the kinematic maps, seem to match with the densest regions of the synthetic maps.

7.3.3 Experimental metrics

The two metrics presented above, kinematic map surface and entropy measure, are calculated for the three experiments. The results are presented in Table 7.3. The surface measurements meet the lowest surface values calculated with FE simulations of the twelve geometries. The covered surface is lower on the experimental maps than on the corresponding numerical map, as observed earlier. However, the entropy measure is better in the experimental maps, meaning that the points are more evenly distributed in the covered area.

Numerically, the sample (c) maximises the surface measure while the design (f) maximises the entropy measure. Experimental results show that the sample ANR 3.1 with design (c) maximises the two metrics. Its entropy measure surpasses the ones calculated with synthetic data while its surface measure reaches the lowest surface measure of the numerical simulations.

Considering the ability of elastomers to “chose” uniaxial tension over other deformation modes, and the fact that this mode is easily triggered at large strain, the metrics could have been calculated on a truncated kinematic map more representative of the “most difficult to reach” deformation modes.

Geometry	Sample	Surface	Entropy
(c)	ANR 2.3	567	5.21
	ANR 3.3	672	5.39
	mean	619.5	5.3
	FE	828	2.43
(f)	ANR 3.2	606	5.24
	FE	762	2.47

Table 7.3: Experimental metrics for the chosen designs.

7.4 Conclusion

The choice of sample design can influence the diversity of deformation modes and magnitudes observed during a test. Pierced membranes have been tested with heterogeneous tests in this study.

Metrics have been defined to characterise the "multiaxiality" of the test. The Finite Element Simulation results differ from the experimental results. This can be due to the choice of model, but also due to the testing protocol where some slipping of the sample was observed in the jaws.

Further investigation on the influence of sample design on tests' "multiaxiality" could be conducted using Topology Optimisation methods.

General conclusion

General conclusion

In the intricate and ever-evolving realm of mechanics of materials context, our expedition into the mechanical response of hyperelastic materials, examplified by synthetic rubber, has unveiled a world of challenges and untapped potential. As we conclude this exploration, we are left with a profound appreciation for the complexities that underlie the seemingly simple behaviour of these materials.

Identifying the mechanical response of materials remains one of the challenges of mechanics of materials. The diversity of materials, identification methods and models renders identification a tricky process. However, modelling the complete mechanical response of materials is needed for design and industrial applications. The state-of-the-art of identification methods and models is still expanding as researchers develop new methods and models to address the challenge of identification. This work is focused on hyperelastic materials. It addresses the question of identification through the exploration of both the kinematic and complete (stress, energy) mechanical responses of materials. The kinematic part of the mechanical response of materials is measurable through DIC techniques while the stress part of the mechanical response is not. However, recent developments in model-free Data-Driven methods allow us to estimate a balanced stress field without the influence of a model: this is the role of the Data-Driven Identification (DDI) method [57]. The method provides a stress field that is not smoothed or filtered by the application of a continuous model. The diversity of the experimental data but also its noise is conserved. Motivated by the exploration of the possibilities offered by the DDI method, the present thesis has investigated the exploration and understanding of the kinematic and mechanical response of hyperelastic elastomer materials to complex loads. Motivated also by the development of tests designed for identification, this study provides the keys to assessing the quality of mechanical tests in terms of the diversity of deformation states, tests made possible by an innovative test bench featuring a hexapod machine.

After describing the state-of-the-art of identification methods and their respective challenges, as well as mechanical models for hyperelastic materials, the objectives of the study were defined. The first one was to generate synthetic and experimental data on multiaxial tests designed for pierced elastomeric membranes. A kinematic response map of the material was then created. This map involves well-chosen invariants of Hencky's logarithmic strain tensor to describe the deformation modes and amplitudes undergone by a material during a test. Representation of the density of points on the map enables comparison between several tests. However, the kinematic map is not sufficient to describe the complete mechanical response of the material: a stress component is missing. Integrating it into the kinematic map to create a mechanical response map of the material was the next objective. For this purpose, a scalar physical quantity was chosen: the strain energy density. Often used to derive hyperelastic models, the strain energy density can be calculated from the strain field and the associated stress field. The mechanical response map describes the mechanical response of the material by relating kinematic response and strain energy density in a visual tool. In this work, experimental

stress fields are calculated without a model, using the DDI method in a formulation adapted to hyperelastic problems. The mechanical response map of materials is included in the Data-Driven Model Identification (DDMI) method validation process: it shows how close the adapted models are to the experimental data. The kinematic response map is used to design specimens that maximise the diversity of deformation states encountered during testing. Two metrics based on the kinematic map rule the final sample choice.

The major contribution of this thesis work is the development of a new identification method which reconciles "model-free Data-Driven" methods and models. DDMI was tested on synthetic data and then successfully applied to experimental data. It emerges that it is possible to estimate a balanced stress field from a multiaxial test without a constitutive law, and then to calculate the associated strain energy density field, before adjusting the parameters of a model to it, a model which is chosen at the end of the process. The estimated stress field is then free of modelling bias and faithful to the experimental deformation field. The choice of the model postponed at the end of the process allows it to be changed easily and at a lower cost. The method also allows fitting models on multiaxial experimental strain energy density field, which represents a new possibility for identification.

Several minor contributions can be highlighted. First, the enrichment of the test databases on SBR by making available the experimental data acquired during this thesis work. Secondly, the development of the two maps allowed us, in this manuscript, to successively explore the kinematic response of the materials and their complete mechanical response. These easy-to-use visual tools allow an overview of the characteristics of a triplet (material, sample (geometry), loading conditions). They can be used to characterise a test or to include the quantification of multiaxiality during its development. Finally, this work renders it possible to consider the optimisation of the geometry of the experimental specimens developed for identification.

Several prospects emerge from this work:

- The DDMI method could be tested with other materials whose behaviours are covered by the DDI method: with heterogeneous samples or elastoplastic materials in a short-term study for example.
- A medium-term prospect could be to enrich the two maps to include additional features to represent different behaviours, such as dissipation for plastic materials, or temporal features for viscoelastic materials.
- Regardless of viscous effects, time could be considered when observing the characteristics of a multiaxial test. The follow-up of the position of a given mesh element on the kinematic map during the test could be studied. This short-term study would bring more understanding of the benefits of the sample geometry on multiaxiality.
- Sample design could be studied with more advanced techniques, such as topology optimisation to generate "tailor-made" samples matching with particular prescribed experimental conditions.

In the end, the prospects proposed here are a reflection of the work from which they derive: multiple, exploring several directions of work, but all serving the same purpose, the enrichment, however small, of knowledge around materials and the means to know their mechanical behaviour a little better.

Appendices

Annexe A

Résumé étendu en français

Cette annexe répond à la demande de l'Ecole Doctorale Sciences de l'Ingénierie et des Systèmes de fournir un résumé substantiel en français pour tout manuscrit rédigé en langue anglaise. Il présente le travail de thèse dans sa globalité, en suivant le plan du manuscrit. La majorité des figures du manuscrit ne sont pas reprises afin d'alléger ce résumé.

Contents

A.1 Introduction

Les matériaux qui nous entourent sont tous différents et possèdent des propriétés uniques. Il n'a pas fallu longtemps à l'humanité pour découvrir ces différences de propriétés. L'ingéniérie mécanique a fait naître le besoin d'identifier et de modéliser le comportement mécanique des matériaux. « Identifier » le comportement mécanique du matériau signifie souvent lui associer une équation appelée modèle de comportement, puis ajuster ses paramètres sur des données expérimentales. En changeant de paradigme et en s'autorisant à représenter le comportement des matériaux de manière discrète, « identifier » peut alors vouloir dire « estimer la partie manquante de la réponse mécanique des matériaux par une approche sans modèle ». C'est le cas de la méthode Data-Driven Identification (DDI, ou identification pilotée par les données).

Considérant que l'identification, la modélisation et la prédiction du comportement mécanique des matériaux constitue toujours un défi pour les chercheurs, ces travaux abordent les questions suivantes :

- Comment peut-on développer des essais hétérogènes pour des matériaux élastiques en grandes déformations ?
- Peut-on faire collaborer les méthodes pilotées par les données et les approches classiques de modélisation pour bénéficier des avantages de chacune ?

Pour répondre à ces questions, nous proposons d'explorer la réponse mécanique des membranes élastomères, de la conception d'éprouvettes d'essai au développement d'une nouvelle méthode d'identification.

Le résumé suivant est structuré en trois sections successives. La première aborde le contexte général et l'état de l'art des méthodes d'identification, puis développe le cadre de travail. La seconde section présente les essais développés pour l'étude puis conduit le lecteur dans l'exploration de la réponse cinématique du matériau puis sa réponse mécanique complète. Enfin, la troisième section présente une nouvelle méthode d'identification alliant méthode pilotée par les données et modélisation, puis une courte étude de l'influence de la géométrie des éprouvettes sur la multiaxialité des essais.

A.2 Contexte général et cadre de travail

Cette section résume les travaux présentés dans la première partie du manuscrit. Dans un premier temps, l'état des connaissances concernant les méthodes d'identification, leurs avantages et inconvénients sont présentés. Dans un second temps, les objectifs de ces travaux de thèse sont explicités, ainsi que le matériau utilisé pour les essais expérimentaux.

A.2.1 Identification

Avec l'ingénierie mécanique est apparue la nécessité d'identifier et de modéliser la réponse mécanique des matériaux. Cette modélisation permet aux ingénieurs de concevoir des pièces industrielles, de comprendre, reproduire et prédire leur comportement. Les modèles, ou lois constitutives, sont l'outil clé pour modéliser la réponse mécanique du matériau. Il s'agit d'équations reliant au moins une mesure de déformation à une mesure de contrainte, et faisant intervenir un ou plusieurs paramètres. Il existe de nombreuses lois constitutives, adaptées à un type de matériau ou à une propriété, pour une plage de déformation donnée.

Quelques bonnes pratiques pour l'utilisation des lois constitutives et modèles sont mises en évidence dans ce travail. L'identification ou « l'art » d'adapter un modèle de comportement à la réponse expérimentale d'un matériau donné est étudiée. La méthode classique, basée sur des essais à états de déformation simples, permet d'adapter les paramètres du modèle au champ de contraintes. Ce champ de contraintes peut être directement calculé à partir de mesures expérimentales, grâce aux modes de déformation simples. La méthode est illustrée sur la Figure A.1.

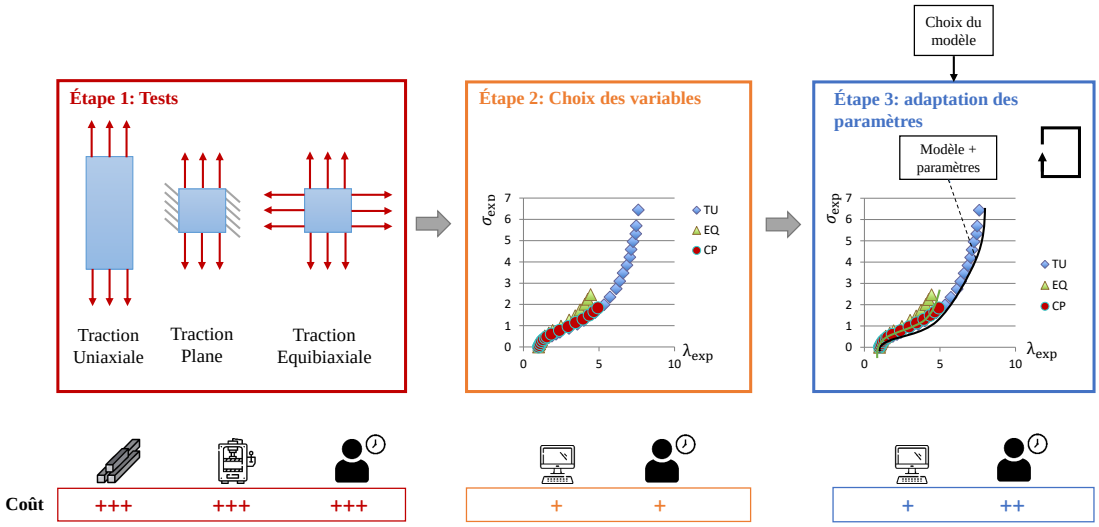

FIGURE A.1 : Illustration des étapes nécessaires à l'identification d'un modèle de comportement, selon la méthode classique. Les coûts exprimés pour chaque étape sont évalués qualitativement. Ils représentent des coûts en matériaux, temps d'utilisation de machines, temps humain ou encore temps de calcul.

Des méthodes d'identification basées sur des mesures de champ ont récemment vu le jour, grâce à la corrélation d'images numériques, permettant l'identification sur une seule expérience multiaxiale. La méthode FEMU (Finite Element Model Updating) est présentée comme un exemple de méthode d'identification basée sur des mesures de champ. Ses coûts qualitatifs comparés à ceux de la méthode classique sont présentés en figure A.2

A.2.2 Objectifs

Cette section se concentre sur la définition et la description des objectifs de l'étude :

- la mise en place et l'exécution d'**essais multiaxiaux**,
- le développement d'un outil de visualisation pour décrire la cinématique de l'essai : la **« carte cinématique »**,
- l'amélioration l'outil de visualisation pour englober la réponse en contrainte du matériau et créer la « **carte de réponse mécanique du matériau** »,
- le développement d'une **méthode d'identification pilotée par les données** basée sur des essais multiaxiaux et reposant sur un choix de modèle en fin de procédure,
- et finalement l'utilisation de la carte cinématique pour améliorer la **diversité des modes de déformation** de l'essai en développant de nouvelles géométries d'éprouvettes.

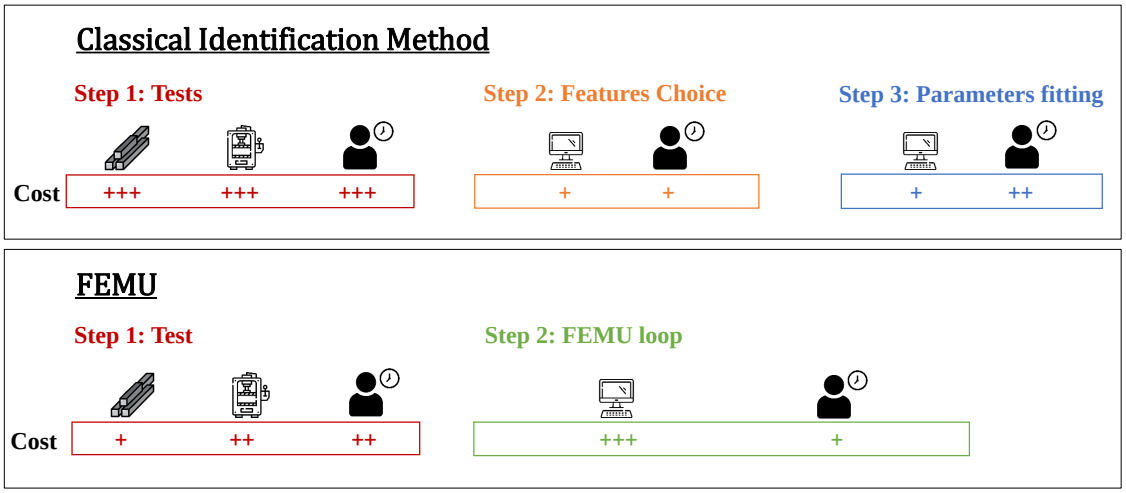

FIGURE A.2 : Qualitative costs evaluation comparison for Classical Identification method and FEMU. The description of the different steps can be found in Figures 1.3 and 1.4.

Le SBR chargé au noir de carbone utilisé à des fins expérimentales est étudié au moyen d'essais de traction uniaxiale présentés sur la Figure A.3, d'essais de relaxation, d'essais de traction uniaxiale cyclique et d'une analyse mécanique dynamique (DMA). Le matériau présente certaines propriétés visqueuses, observées sur les courbes de traction uniaxiales à différentes vitesses de déformation, et est sujet à l'effet Mullins. Les essais expérimentaux mis en oeuvre dans la suite de la thèse sont effectués avec un chargement toujours croissant pour éviter de déclencher l'effet Mullins, et des taux de déformation lents et fixes pour minimiser les effets visqueux.

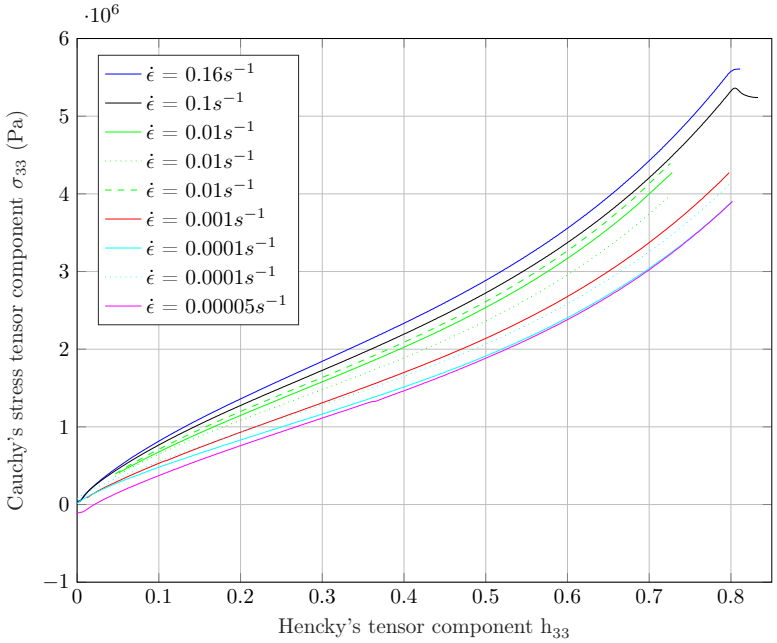

FIGURE A.3 : Courbes de traction uniaxiale expérimentales pour le SBR chargé au noir de carbone utilisé pour l'étude. Les essais ont été réalisés à 24°C, et six vitesses de déformation différentes.

Ce travail est mené à l'aide de Matlab pour le développement de code, Abaqus pour les simulations éléments finis, GMSH pour les maillages et Ufreckles pour la corrélation d'images numérique.

A.3 Explorer la réponse mécanique des matériaux

Cette section explore les méthodes expérimentales utilisées dans ces travaux. Ensuite, la représentation de la réponse mécanique des matériaux est envisagée au travers de la création d'une « carte de réponse cinématique » puis d'une « carte de réponse mécanique des matériaux ».

A.3.1 Acquisition de données

Les données synthétiques et expérimentales sont présentées dans ce chapitre.

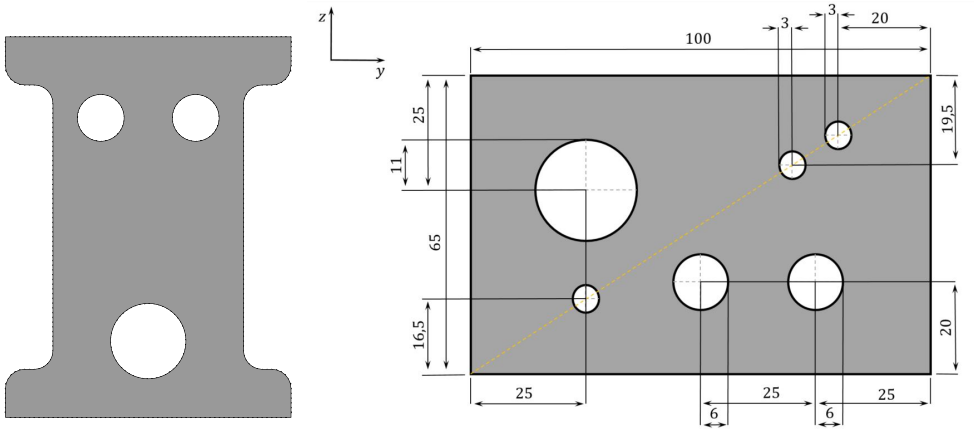

(a) Eprouvette pour les données synthétiques

(b) Eprouvette pour les données expérimentales

FIGURE A.4 : Géométrie des éprouvettes utilisées pour les campagnes d'essais.

Les données synthétiques sont construites à l'aide d'un modèle d'Ogden du troisième ordre ajusté sur les données historiques de Treloar [90]. Ce« matériau numérique » est inclus dans un modèle elements finis, construit avec une éprouvette type traction uniaxiale percée de trois trous, présentée en Figure A.4. Cet échantillon est chargé avec un déplacement imposé de sa limite supérieure, jusqu'à un étirement global de 300 %.

Les données expérimentales sont obtenues à l'aide d'un banc d'essai construit avec un hexapode, machine à six vérins et six degrés de liberté, un capteur de force et une caméra optique. Le banc expérimental est présenté sur la Figure A.5. Le champ de déplacement est mesuré à l'aide d'une méthode de corrélation d'images numériques. Des membranes SBR chargé au noir de carbone et percées de six trous sont utilisées. Leur géométrie est présentée sur la Figure A.4. Un essai complexe avec une trajectoire de chargement hétérogène est appliqué avec quatre vitesses de chargement différentes.

Les bases de données synthétiques et expérimentales sont formatées de manière homogène et stockées sur un dépôt public en ligne pour que toute personne intéressée puisse travailler avec. Ce dépôt public constitue le livrable de ce chapitre, il est disponible ici [22].

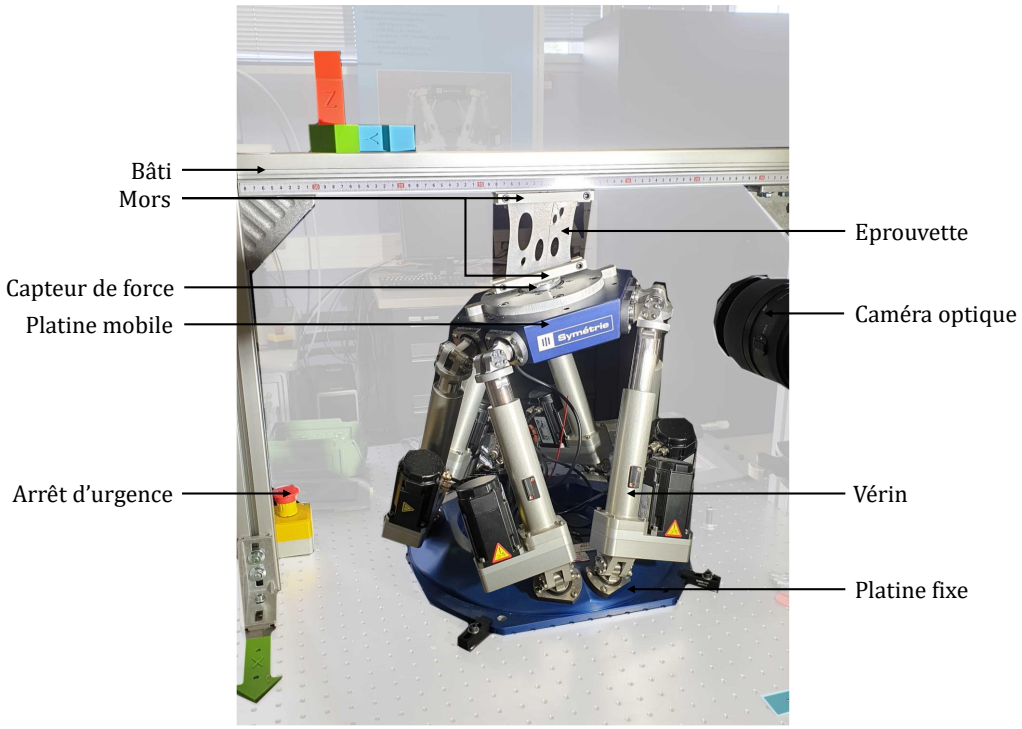

FIGURE A.5 : Banc d'essai expérimental autour de l'hexapode.

A.3.2 Une carte pour explorer la réponse cinématique des matériaux

Les essais multiaxiaux peuvent être utilisés à des fins d'identification. Le principal avantage des essais expérimentaux complexes est la capacité de caractériser la réponse mécanique d'un matériau pour une grande diversité de modes de déformation et de chargements imposés. Pour évaluer la diversité des modes de déformation rencontrés au cours de l'essai, la cinématique doit être observée et décrite. L'observation de la cinématique est réalisée à l'aide d'un outil graphique construit avec les invariants du tenseur de déformation logarithmique de Hencky : la **« carte cinématique »**.

La carte cinématique est une « heatmap » des couples (K_2, K_3), K_2 indiquant l'amplitude de la déformation et K_3 le mode de déformation. Cet outil vise à fournir une représentation visuelle des différentes déformations subies par le matériau tout au long de l'essai, ainsi que leur répartition entre les modes et les amplitudes. La carte cinématique est construite pour des données synthétiques et expérimentales. La Figure A.6 présente la carte de réponse cinématique de l'essai synthétique de traction sur une éprouvette percée. Ces données présentent une majorité de points présentant un mode de déformation de traction uniaxiale ($K_3 = 1$). Cependant, les tests expérimentaux effectués avec un dispositif hexapode sous déplacements imposés variables présentent une carte cinématique plus distribuée, ce qui renforce leur intérêt à des fins d'identification.

En illustrant graphiquement le comportement cinématique complexe, les chercheurs et les industriels peuvent mieux comprendre la réponse du matériau aux chargements appliqués et les modes de déformation qui en résultent. Cet outil graphique peut faciliter l'analyse et l'interprétation des données d'essai, ce qui permet d'améliorer les techniques d'identification et de mieux comprendre le comportement des matériaux dans différentes conditions de chargement.

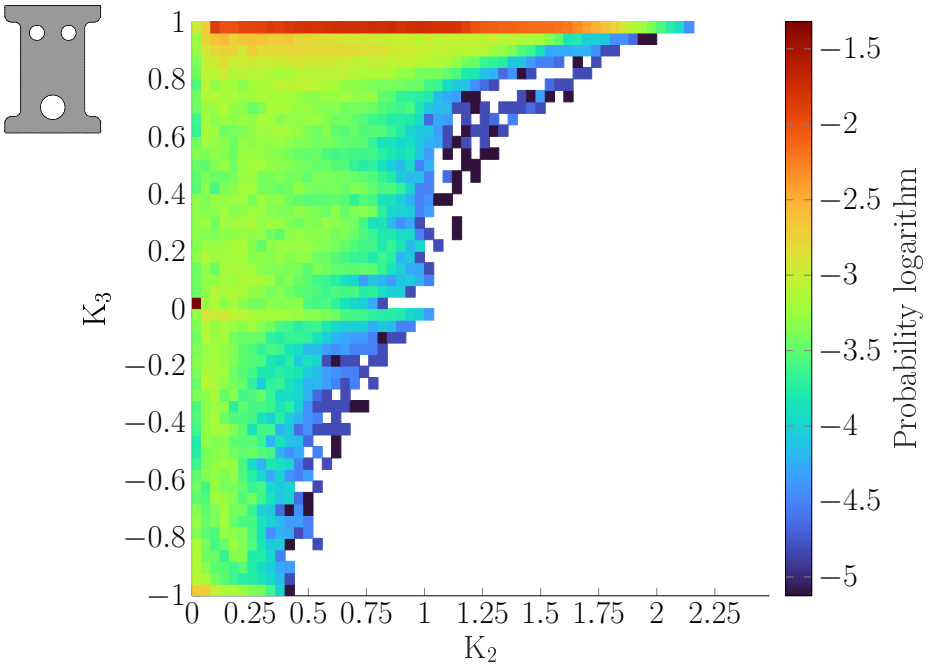

FIGURE A.6 : Carte de réponse cinématique pour un essai numérique. La carte représente la densité de points dans le plan (K_2, K_3) sur lequel sont tracés tous les couples (K_2, K_3) correspondant à chaque élément de maillage à chaque pas de temps.

A.3.3 Explorer les champs de contraintes

L'Identification pilotée par les données (DDI) est une méthode permettant de calculer le champ de contrainte expérimental sans utiliser de modèle de comportement. Elle a été développée par Leygue *et al.* [57]. Cette méthode est basée sur des regroupements successifs (*« clustering »*) et s'appuie sur l'équilibre mécanique de la structure pour fournir un champ de contraintes admissible. La méthode DDI est appliquée à des données synthétiques et expérimentales. Les champs de contrainte résultants sont observés à l'aide d'une représentation par histogramme. Cependant, la volonté est de résumer les contraintes avec une variable scalaire et de l'ajouter à la carte cinématique construite dans le chapitre 4.

La densité d'énergie de déformation représente le champ de contraintes pondéré par le champ cinématique. Il s'agit d'une grandeur qui englobe les déformations et les contraintes dans une valeur scalaire. La densité d'énergie de déformation est choisie pour représenter la réponse en contraintes des matériaux dans la **carte de réponse mécanique des matériaux**.

La nouvelle carte, présentée sur la Figure A.7 pour les données synthétiques, englobe à la fois cinématique et contraintes, dans un seul graphique caractéristique. En incorporant les informations sur les contraintes aux données cinématiques, cet outil graphique enrichi peut fournir une vue d'ensemble du comportement du matériau dans différentes conditions de chargement, ce qui permet de mieux comprendre sa réponse mécanique. Cette approche facilite l'exploration des schémas de réponse en contraintes et de leurs relations avec les caractéristiques cinématiques, contribuant ainsi à l'avancement des techniques de modélisation, de caractérisation et d'identification des matériaux pilotées par les données.

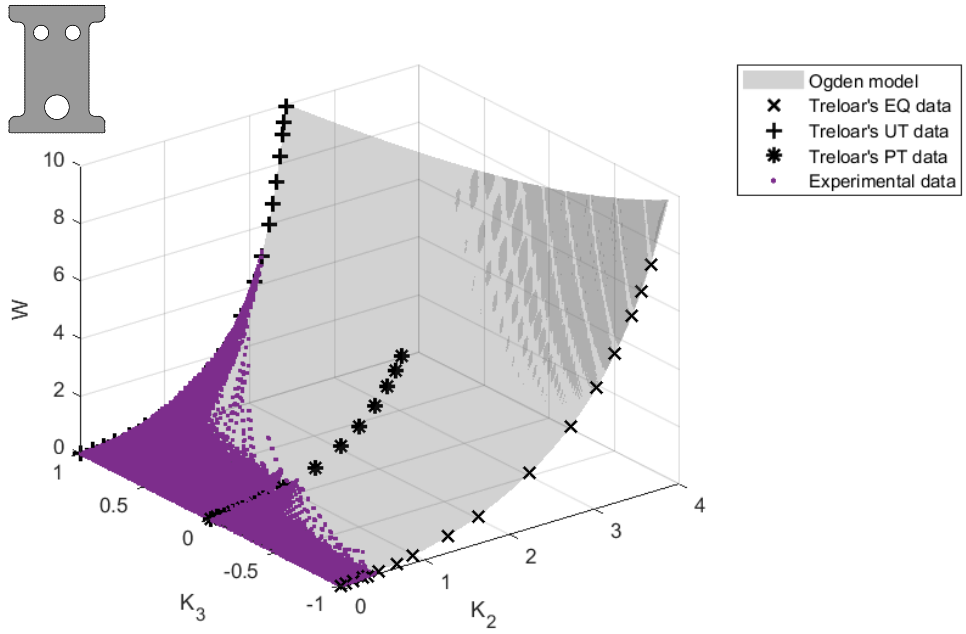

FIGURE A.7 : Carte de réponse mécanique pour les données synthétiques. Les points expérimentaux sont présentés en violet. La surface grise représente le modèle d'Ogden utilisé pour construire le dataset numérique. Les données de Treloar sont représentées en noir.

A.4 Applications expérimentales

Cette section présente le cœur du travail de ces travaux de thèse. Tout d'abord, une méthode d'identification basée sur les approches Data-Driven (pilotées par les données) est présentée et appliquée à des données synthétiques puis expérimentales. Ensuite, plusieurs géométries d'éprouvettes sont comparées pour augmenter la multiaxialité de nos essais expérimentaux.

A.4.1 Identification de modèle pilotée par les données

L'**identification de modèle pilotée par les données** (DDMI) est une méthode d'identification qui vise à combiner les avantages de la méthode d'identification classique et des méthodes d'identification basées sur des mesures de champ. Elle consiste à réaliser une expérience multiaxiale et à mesurer ses champs cinématiques, puis à exécuter la DDI pour estimer les contraintes et le champ de densité d'énergie de déformation associé. Une fois les grandeurs physiques recueillies, un modèle peut être choisi et ajusté sur les données expérimentales. Les étapes de la méthode sont présentées sur la Figure A.8.

La procédure d'identification peut être appliquée au champ de contraintes DDI ou au champ de densité d'énergie de déformation DDI. Différentes fonctions objectives ont été testées et comparées sur des données synthétiques. La meilleure méthode est appliquée aux données expérimentales. Dans l'ensemble, la méthode d'ajustement la meilleure et la plus pratique repose sur une fonction objective basée sur l'erreur absolue, écrite avec un changement de variable, et minimisant la distance entre les champs de densité d'énergie de déformation.

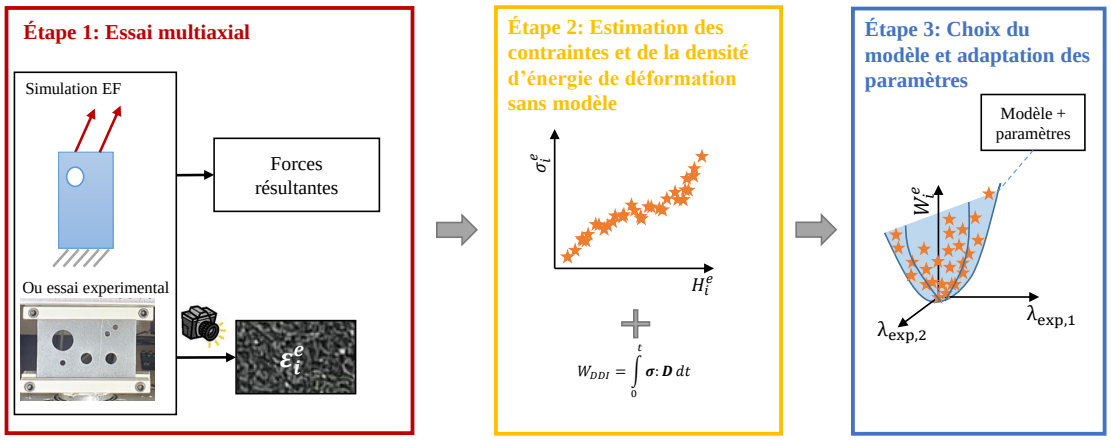

FIGURE A.8 : Présentation schématique de la méthode d'identification de modèle pilotée par les données (DDMI). La méthode peut être adaptée aussi bien à des données synthétiques qu'à des données expérimentales. Deux méthodes peuvent être appliquées au moment de l'adaptation des paramètres du modèle : identifier les paramètres sur le champ de contraintes ou bien sur le champ de densité d'énergie de déformation. Sur ce schéma, seule l'adaptation des paramètres sur le champ de densité d'énergie de déformation est représentée.

L'identification de modèles pilotée par les données est appliquée aux données expérimentales. Deux modèles sont ajustés sur le champ de densité d'énergie de déformation calculé par DDI : un modèle d'Ogden à trois termes et un modèle de Yeoh. Les champs de densité d'énergie de déformation des deux modèles sont comparés au champ de densité d'énergie de déformation DDI et montrent des niveaux d'erreur similaires à ceux observés avec les données synthétiques. La comparaison avec les données de traction uniaxiale prouve que les deux modèles ajustés par DDMI peuvent représenter le comportement du matériau dans les plages de déformation des données expérimentales.

A.4.2 Conception d'éprouvettes pour les méthodes d'identification basées sur les essais multiaxiaux

Après avoir exploré les méthodes d'identification, la carte cinématique construite dans le chapitre 4 est utilisée pour concevoir des éprouvettes qui maximisent « la multiaxialité » d'un essai hétérogène. Deux métriques sont définies :

- une mesure de la surface couverte par les points de la carte cinématique,
- une mesure de l'entropie, décrivant la dispersion des points sur la carte.

Les métriques sont explicitées sur la Figure A.9.

Douze modèles d'éprouvettes sont proposés. Ils sont basés sur une membrane SBR chargé au noir de carbone de 100×65 mm^2 percée de trous circulaires de différentes tailles. Des simulations par éléments finis sont effectuées, les cartes cinématiques sont tracées et les métriques sont calculées. Les deux modèles maximisant les métriques sont choisis pour être testés expérimentalement. Les essais expérimentaux sont effectués et les champs cinématiques sont mesurés à l'aide d'une méthode de corrélation d'images numériques. Les cartes cinématiques expérimentales sont tracées et comparées à celles issues des simulations par éléments finis.

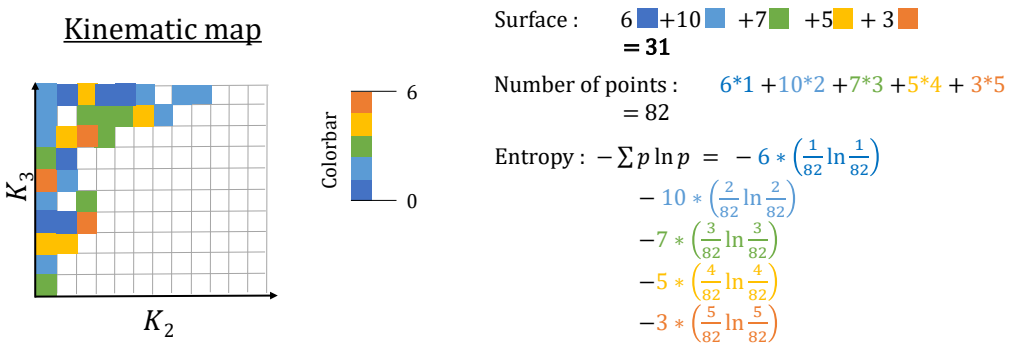

FIGURE A.9 : Définition des métriques à partir d'une carte cinématique.

Les cartes expérimentales présentent des mesures de surface plus petites à cause de la difficulté de faire correspondre le maillage DIC aux limites de l'échantillon. Leur mesure d'entropie est meilleure que les simulations par éléments finis, ce qui signifie qu'il y a moins de zones avec une forte densité de points sur la carte cinématique expérimentale.

Remarque : Cette application a été réalisée avec des étudiants en troisième année d'école d'ingénieurs. L'accent a été mis sur la reproductibilité des expériences et la simplicité des modèles proposés. Des recherches plus approfondies sur la conception de l'échantillon pourraient être effectuées à l'aide de techniques d'optimisation topologique, mais nécessiteraient des techniques de découpe plus avancées pour former les éprouvettes.

A.5 Conclusion

L'exploration du comportement mécanique des élastomères nous a permis d'en approcher la complexité. Identifier le comportement mécanique de ces matériaux reste un défi de taille. La diversité des matériaux, méthodes et modèles sont en cause.

Après avoir décrit l'état de l'art des méthodes d'identification et des modèles hyperélastiques, les objectifs de l'étude ont été définis. La réalisation d'essais et leur exploitation pour construire des cartes de réponse cinématique puis une carte de réponse mécanique du matériau ont constitué les premiers objectifs de l'étude. Ensuite, les méthodes pilotées par les données ont été associées aux méthodes d'identification pour créer la DDMI (Data-Driven Model Identification), ou Identification de Modèles pilotée par les données. Enfin, la géométrie des éprouvettes et son influence sur la multiaxialité des essais a été testée en utilisant une carte de réponse cinématique.

La contribution majeure de ce travail est le développement de la DDMI sur des données synthétiques et expérimentales, permettant l'adaptation de modèles de comportement sur un champ de densité d'énergie de déformation expérimental.

Les perspectives de ce travail sont nombreuses, mais on peut en citer une qui se réfère à notre contribution majeure : la DDMI pourrait être adaptée à d'autres matériaux et d'autres comportements, parmi le spectre déjà traité par la méthode DDI.

Appendix B

Lode invariants to describe stress field

B.1 Definition

In plasticity, some mechanical stress invariants are defined to describe the stress state of a material. Three invariants are recalled and well-described by Brannon [12]:

$$\begin{cases} J_1 = \mathrm{tr}(\boldsymbol{\sigma}) \\ J_2 = \frac{1}{2}\mathrm{tr}\left(\mathrm{dev}(\boldsymbol{\sigma})\right)^2 \\ J_3 = \frac{1}{3}\mathrm{tr}\left(\mathrm{dev}(\boldsymbol{\sigma})\right)^3 \end{cases} \text{, with } \mathrm{dev}(\bullet) = \bullet - \mathrm{tr}(\frac{(\bullet)}{3})\boldsymbol{I}, \tag{B.1}$$

$\boldsymbol{\sigma}$ being Cauchy's stress tensor. From these three invariants, the Lode invariants (r, θ, z) can be written:

$$\begin{cases} r = \sqrt{2J_2}, \\ \sin, 3\theta = \frac{J_3}{2}\left(\frac{3}{J_2}\right)^{3/2}, \\ z = \frac{J_1}{\sqrt{3}} \end{cases} \text{,with } \mathrm{dev}(\bullet) = \bullet - \mathrm{tr}(\frac{(\bullet)}{3})\boldsymbol{I}. \tag{B.2}$$

These invariants represent a polar coordinate system. Each region of the circular plan defines the stress state of the material, as shown in Figure B.1: the plane region corresponding to a Lode angle of $\theta = 30° \pm 120°$ represents triaxial extension or biaxial compression stress states, whereas Lode angles of $\theta = 0° \pm 60°$ represent shear stress state, and $\theta = -30° \pm 120°$ represent triaxial compression or biaxial extension stress states. Each $60°$ wide region, from $\theta = 30° \pm 60°$ to $\theta = 90° \pm 60°$ corresponds to a specific value order of the principal stresses. For example, the region which boundaries are $\theta \in [-30°, 30°]$ corresponds to principal stresses as $\sigma_3 > \sigma_2 > \sigma_1$.

It can be seen as Hencky's strain tensor invariants counterparts for stresses.

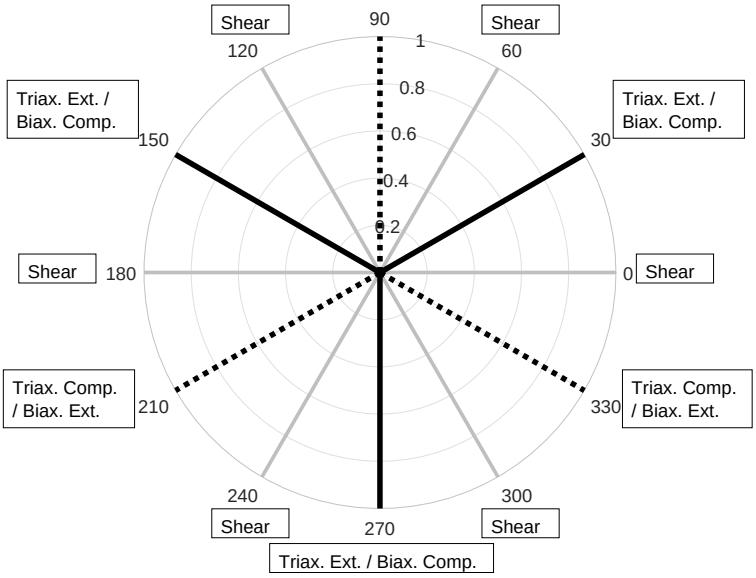

Figure B.1: Description of the periodicity of the Lode angle. From [12], Figure 6.2.

B.2 Application to synthetic data

Figure B.2 presents the Lode invariants for synthetic data. The majority of points are located along the $\theta = 30°$ straight line, corresponding to triaxial extension / biaxial compression. It is consistent with the uniaxial tension strain state observed on the kinematics map.

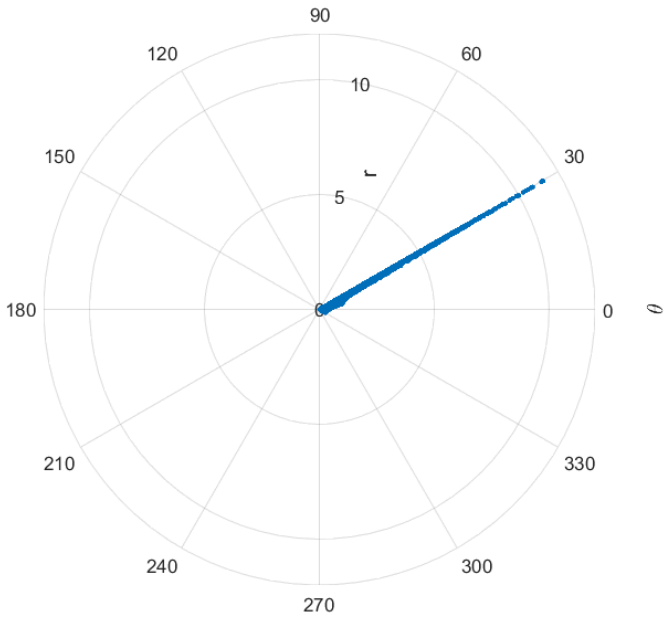

Figure B.2: Lode invariants representation for synthetic data.

B.3 Application to experimental data

Figure B.3 presents the Lode invariants for experimental data. The points are concentrated in the $[-30°, 30°]$ area. They are mostly following the triaxial extension / biaxial compression straight line. This is consistent with the kinematics map presented previously.

This representation gives overall clues of the diversity of the stress field but misses a link with the kinematic fields. The choice was made not to incorporate it into the kinematic map.

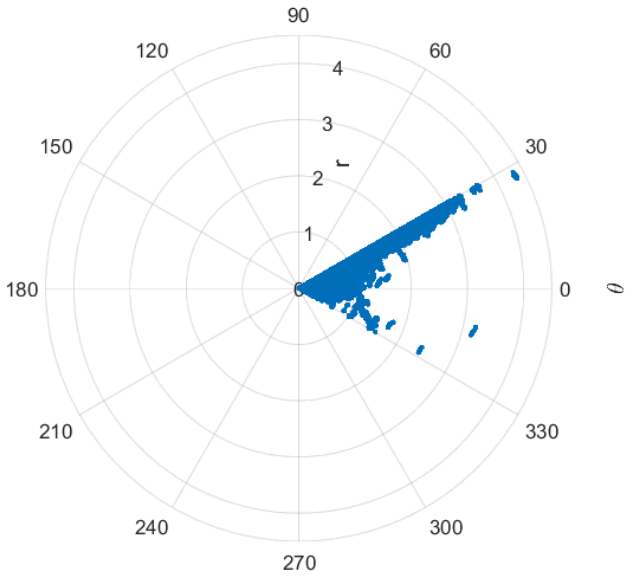

Figure B.3: Lode invariants representation for experimental data.

Appendix C

Convergence issues with Finite Strain DIC on Ufreckles

The DIC parameters presented in Chapter 3 were not the first parameter set that has been applied to the experimental data. Smoothing was applied on the FE-DIC model and the results were not satisfactory. Smoothing is often recommanded to reduce DIC displacement fields noise, particularly for High Gradient Strain fields [58]. Strain smoothing, median smoothing were tested, along with varying mesh element sizes. The results are presented below.

C.1 Results with strain smoothing

Figure C.1 presents the results of DIC on experimental images. FE-DIC was run with 80 px unstructured T3 elements, and a 40" px strain smoothing. The figure shows the strain magnitude, presented with a colourmap, plotted on the calculated deformed configuration. This deformed configuration is plotted on top of the corresponding frame. The deformed configuration does not match with the sample boundaries on the picture frame. This means that the DIC process did not succeed in calculating the displacement field.

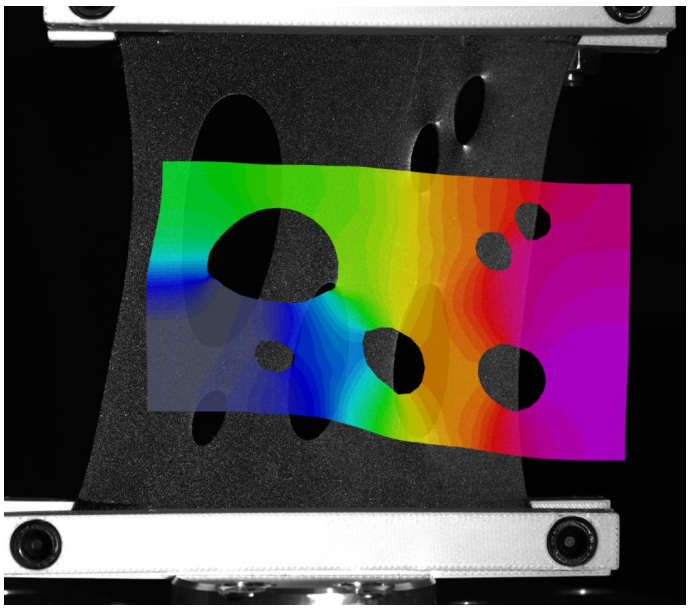

Figure C.1: Results of DIC applied with strain regularisation (40) on Sample ANR 2.1.

When observing the calculated deformed configuration plotted on corresponding frames, frame by frame, it seems that the calculated displacement field begin to diverge from the observed one around the frame 200 over 500. It seems that once the sample reaches a given global strain, the smoothed algorithm considers that it cannot be stretched more and the calculated displacement field diverges from the observed one. The calculated deformed sample tend to regain its undeformed dimensions, exhibiting only small strains in the last frames.

Figure C.2 presents the results for a FE-DIC run with 50 px unstructured T3 elements and strain smoothing of 40 px. The same observations as the previous case can be made: at some point, around frame 175, the calculated deformed configuration begin to diverge from the observed one. The final frame presents a deformed configuration with small strains and which does not match with the picture frame at all.

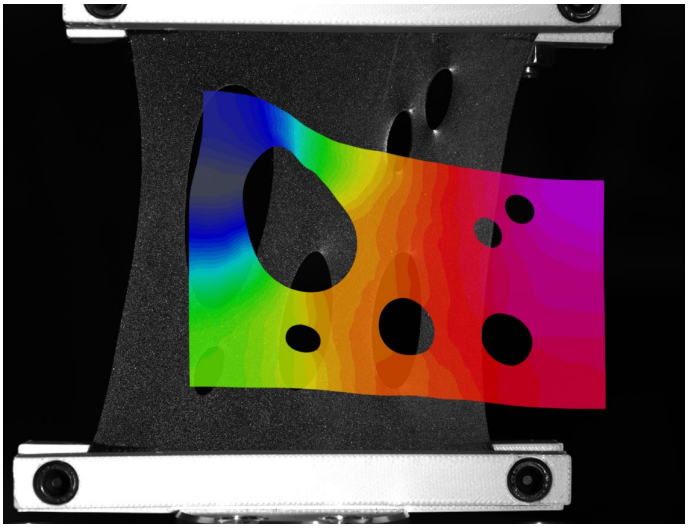

Figure C.2: Results of DIC applied with strain regularisation (40) and a refined mesh with elements of 50 px size on Sample ANR 2.1.

C.2 Results with median smoothing

Median smoothing was applied on a 80 px unstructured T3 elements FE-DIC solver. The results are presented in Figure C.3. The deformed configuration does not match with the sample boundaries as seen in the corresponding frame. Additionnaly, it seems that contrarily to the previous examples, the calculated deformed mesh appears “folded”: some parts seem to be superimposed to others. It is visible on the left area of the sample: different colours seem superimposed with red mesh elements on light blue.

The same median smoothing was applied on a larger mesh with 100 px unstructured T3 elements. The results are presented in Figure C.4. This figure presents the same characteristics as the previous one: the deformed configuration does not match with the corresponding frame, and some parts of the mesh seem superimposed.

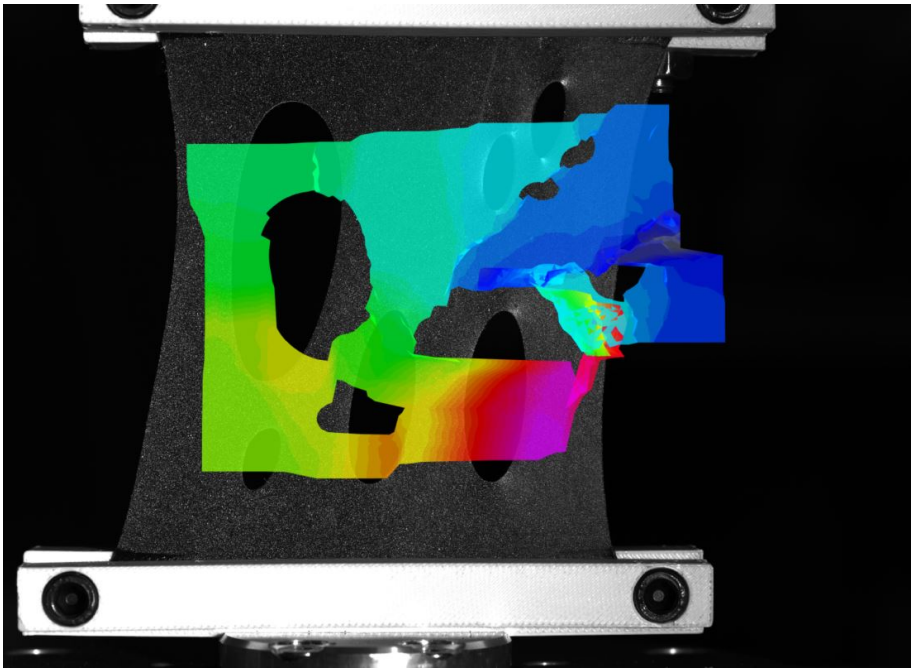

Figure C.3: Results of DIC applied with Median regularisation (1) on Sample ANR 2.1.

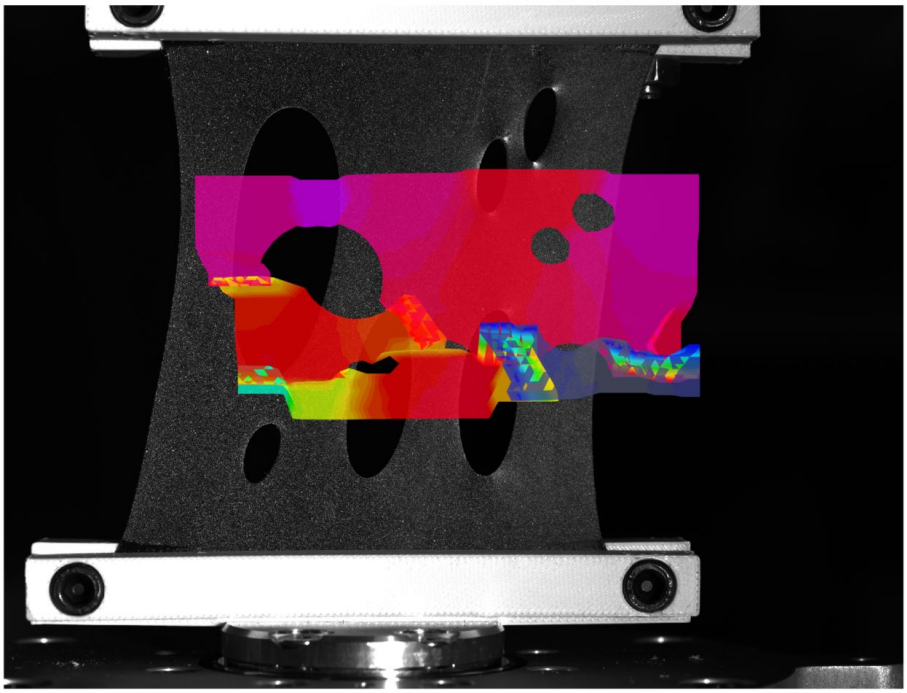

Figure C.4: Results of DIC applied with Median regularisation (1) and a larger mesh with elements of 100 px size on Sample ANR 2.1.

Bibliography

[1] D. Al Akhrass, J. Bruchon, S. Drapier, and S. Fayolle. "Integrating a logarithmic-strain based hyperelastic formulation into a three-field mixed finite element formulation to deal with incompressibility in finite-strain elastoplasticity". In: *Finite Elements in Analysis and Design* 86 (2014), pp. 61–70.
Cited on page 62.

[2] S. Andrieux, A. B. Abda, and H. D. Bui. "Reciprocity principle and crack identification". In: *Inverse problems* 15.1 (1999), p. 59.
Cited on page 22.

[3] E. Archbold, J. Burch, and A. Ennos. "Recording of in-plane surface displacement by double-exposure speckle photography". In: *Optica Acta: International Journal of Optics* 17.12 (1970), pp. 883–898.
Cited on page 22.

[4] E. M. Arruda and M. C. Boyce. "A three-dimensional constitutive model for the large stretch behavior of rubber elastic materials". In: *Journal of the Mechanics and Physics of Solids* 41.2 (1993), pp. 389–412.
Cited on page 14.

[5] S. Avril, M. Bonnet, A.-S. Bretelle, M. Grédiac, F. Hild, P. Ienny, F. Latourte, D. Lemosse, S. Pagano, E. Pagnacco, et al. "Overview of identification methods of mechanical parameters based on full-field measurements". In: *Experimental Mechanics* 48 (2008), pp. 381–402.
Cited on page 20.

[6] J. M. Ball. "Convexity conditions and existence theorems in nonlinear elasticity". In: *Archive for rational mechanics and Analysis* 63 (1976), pp. 337–403.
Cited on page 16.

[7] B. Barroqueiro, A. Andrade-Campos, J. Dias-de-Oliveira, and R. Valente. "Design of mechanical heterogeneous specimens using topology optimization". In: *International Journal of Mechanical Sciences* 181 (2020), p. 105764.
Cited on page 121.

[8] T. Beda. "An approach for hyperelastic model-building and parameters estimation a review of constitutive models". In: *European Polymer Journal* 50 (2014), pp. 97–108.
Cited on page 14.

[9] G. Besnard, F. Hild, and S. Roux. ""Finite-element" displacement fields analysis from digital images: application to Portevin–Le Châtelier bands". In: *Experimental mechanics* 46 (2006), pp. 789–803.
Cited on page 21.

[10] K.-U. Bletzinger. "Shape Optimization". In: *Encyclopedia of Computational Mechanics Second Edition*. Ed. by E. Stein, R. de Borst, and T. J. R. Hughes. Chichester, UK: John Wiley & Sons, Ltd, 2017, pp. 1–42. DOI: 10.1002/9781119176817.ecm2109.
Cited on page 121.

[11] J. Bonet and R. D. Wood. *Nonlinear Continuum Mechanics for Finite Element Analysis*. Seconde édition. Cambridge University Press, 2008. 340 pp.
Cited on page 14.

[12] R. M. Brannon. "Elements of phenomenological plasticity: geometrical insight, computational algorithms, and topics in shock physics". In: *Shockwave science and technology reference library* (2007), pp. 225–274.
Cited on pages 65, 147, 148.

[13] O. Bruhns, H. Xiao, and A. Meyers. "Constitutive inequalities for an isotropic elastic strain-energy function based on Hencky's logarithmic strain tensor". In: *Proceedings of the Royal Society of London. Series A: Mathematical, Physical and Engineering Sciences* 457.2013 (2001), pp. 2207–2226.
Cited on page 62.

[14] B. C. Cameron and C. C. Tasan. "Full-field stress computation from measured deformation fields: A hyperbolic formulation". In: *Journal of the Mechanics and Physics of Solids* 147 (2021), p. 104186. DOI: 10.1016/j.jmps.2020.104186.
Cited on pages 75, 82.

[15] P. Carrara, L. De Lorenzis, L. Stainier, and M. Ortiz. "Data-driven fracture mechanics". In: *Computer Methods in Applied Mechanics and Engineering* 372 (2020), p. 113390.
Cited on page 82.

[16] G. Chagnon, E. Verron, G. Marckmann, and L. Gornet. "Development of new constitutive equations for the Mullins effect in rubber using the network alteration theory". In: *International Journal of Solids and Structures* 43.22 (2006), pp. 6817–6831. DOI: 10.1016/j.ijsolstr.2006.02.011.
Cited on page 41.

[17] T. Chu, W. Ranson, and M. A. Sutton. "Applications of digital-image-correlation techniques to experimental mechanics". In: *Experimental mechanics* 25 (1985), pp. 232–244.
Cited on page 21.

[18] K. Ciftci and K. Hackl. "Data-Driven simulation of inelastic materials using structured data sets, tangent space information and transition rules". In: *Proceedings in Applied Mathematics & Mechanics* (2021). arXiv: 2101.10730.
Cited on page 82.

[19] D. Claire, F. Hild, and S. Roux. "Identification of damage fields using kinematic measurements". In: *Comptes Rendus Mécanique* 330.11 (2002), pp. 729–734.
Cited on page 22.

[20] C. Cofaru, W. Philips, and W. Van Paepegem. "Improved Newton–Raphson digital image correlation method for full-field displacement and strain calculation". In: *Applied optics* 49.33 (2010), pp. 6472–6484.
Cited on page 22.

[21] M. Conde, A. Andrade-Campos, M. G. Oliveira, and J. M. P. Martins. *Design of heterogeneous interior notched specimens for material mechanical characterization*. 2021.
Cited on page 121.

[22] L. Costecalde. *Zenodo Open Source Data Repository*. 2023. URL: https://doi.org/10.5281/zenodo.10033038.
Cited on pages 47, 56, 140.

[23] L. Costecalde, M. Coret, A. Leygue, and E. Verron. "Characterization of the mechanical response of elastomers using complex experiments: Simple ways to describe multiaxiality". In: *Constitutive Models for Rubber XII: Proceedings of the 12th European Conference on Constitutive Models for Rubber (ECCMR 2022), September 7–9, 2022, Milano, Italy*. CRC Press. 2022, p. 164.
Cited on page 62.

[24] L. Costecalde, A. Leygue, M. Coret, and E. Verron. "Data-Driven Identification of hyperelastic models by measuring the strain energy density field". In: *Rubber Chemistry and Technology* 96.4 (2023), pp. 443–454.
Cited on page 93.

[25] J. Crespo, M. Latorre, and F. J. Montáns. "WYPIWYG hyperelasticity for isotropic, compressible materials". In: *Computational Mechanics* 59 (2017), pp. 73–92.
Cited on page 75.

[26] J. C. Criscione, J. D. Humphrey, A. S. Douglas, and W. C. Hunter. "An invariant basis for natural strain which yields orthogonal stress response terms in isotropic hyperelasticity". In: *Journal of the Mechanics and Physics of Solids* 48.12 (2000), pp. 2445–2465.
Cited on page 64.

[27] H. Dal, K. Açıkgöz, and Y. Badienia. "On the performance of isotropic hyperelastic constitutive models for rubber-like materials: A state of the art review". In: *Applied Mechanics Reviews* 73.2 (2021).
Cited on page 18.

[28] M. Dalémat. "Une expérimentation réussie pour l'identification de la réponse mécanique sans loi de comportement: Approche data-driven appliquée aux membranes élastomères". PhD thesis.
Cited on pages 49, 62, 79, 93.

[29] M. Dalémat, M. Coret, A. Leygue, and E. Verron. "Measuring stress field without constitutive equation". In: *Mechanics of Materials* 136 (2019), p. 103087.
Cited on pages 75, 78, 82.

[30] Dassault Systemes Simulia Corp. *Abaqus CAE*. Version 2019. 2019.
Cited on pages 41, 42, 49, 120.

[31] J. Diani, B. Fayolle, and P. Gilormini. "A review on the Mullins effect". In: *European Polymer Journal* 45.3 (2009), pp. 601–612.
Cited on page 41.

[32] R. Diaz, J. Diani, and P. Gilormini. "Physical interpretation of the Mullins softening in a carbon-black filled SBR". In: *Polymer* 55.19 (2014), pp. 4942–4947.
Cited on page 39.

[33] S. Edwards and T. Vilgis. "The effect of entanglements in rubber elasticity". In: *Polymer* 27.4 (1986), pp. 483–492.
Cited on page 15.

[34] R. Eggersmann, T. Kirchdoerfer, S. Reese, L. Stainier, and M. Ortiz. "Model-free data-driven inelasticity". In: *Computer Methods in Applied Mechanics and Engineering* 350 (2019), pp. 81–99.
Cited on page 82.

[35] M. Elshorbagy. *Step by Step towards Structural Simulation Using ABAQUS Part 1*. 2020.
Cited on page 42.

[36] A. L. Eterovic and K.-J. Bathe. "A hyperelastic-based large strain elasto-plastic constitutive formulation with combined isotropic-kinematic hardening using the logarithmic stress and strain measures". In: *International Journal for Numerical Methods in Engineering* 30.6 (1990), pp. 1099–1114.
Cited on page 62.

[37] M. Flaschel, S. Kumar, and L. De Lorenzis. "Unsupervised discovery of interpretable hyperelastic constitutive laws". In: *Computer Methods in Applied Mechanics and Engineering* 381 (2021), p. 113852.
Cited on pages 22, 93.

[38] A. Freed. *Soft Solids: A Primer to the Theoritical Mechanics of Materials, Modelind and Simulation in Science, Engineering and Technology - Chapter 4 - Viscoelasticity*. Switzerland: Springer International Publishing, 2014.
Cited on page 36.

[39] Geuzaine, Christophe and Remacle, Jean-François. *GMSH*. Version 4.6.0. 2020.
Cited on pages 42, 122.

[40] M. Grediac, F. Pierron, S. Avril, and E. Toussaint. "The virtual fields method for extracting constitutive parameters from full-field measurements: a review". In: *Strain* 42.4 (2006), pp. 233–253.
Cited on page 22.

[41] A. Guery, F. Hild, F. Latourte, and S. Roux. "Identification of crystal plasticity parameters using DIC measurements and weighted FEMU". In: *Mechanics of Materials* 100 (2016), pp. 55–71.
Cited on page 20.

[42] S. Hartmann and P. Neff. "Polyconvexity of generalized polynomial-type hyperelastic strain energy functions for near-incompressibility". In: *International journal of solids and structures* 40.11 (2003), pp. 2767–2791.
Cited on page 16.

[43] H. He, Q. Zhang, Y. Zhang, J. Chen, L. Zhang, and F. Li. "A comparative study of 85 hyperelastic constitutive models for both unfilled rubber and highly filled rubber nanocomposite material". In: *Nano Materials Science* 4.2 (2022), pp. 64–82.
Cited on page 15.

[44] F. Hild and S. Roux. "Digital image correlation". In: *Optical methods for solid mechanics. A full-field approach* 367 (2012), pp. 183–228.
Cited on page 22.

[45] G. A. Holzapfel. *Nonlinear Solid Mechanics: a Continuum Approach for Engineering*. John Wiley & Sons, LTD., 2000. 467 pp.
Cited on pages 13, 50, 84, 95.

[46] P. Ienny, A.-S. Caro-Bretelle, and E. Pagnacco. "Identification from measurements of mechanical fields by finite element model updating strategies: a review". In: *European Journal of Computational Mechanics/Revue Européenne de Mécanique Numérique* 18.3-4 (2009), pp. 353–376.
Cited on pages 23, 24.

[47] E. M. International Digital Image Correlation Society Jones, M. A. Iadicola, et al. *A Good Practices Guide for Digital Image Correlation.* International Digital Image Correlation Society, 2018.
Cited on pages 22, 53.

[48] K. T. Kavanagh and R. W. Clough. "Finite element applications in the characterization of elastic solids". In: *International Journal of Solids and Structures* 7.1 (1971), pp. 11–23.
Cited on page 23.

[49] S. Kawabata, M. Matsuda, K. Tei, and H. Kawai. "Experimental survey of the strain energy density function of isoprene rubber vulcanizate". In: *Macromolecules* 14.1 (1981), pp. 154–162.
Cited on page 19.

[50] T. Kirchdoerfer and M. Ortiz. "Data-driven computational mechanics". In: *Computer Methods in Applied Mechanics and Engineering* 304 (2016), pp. 81–101. DOI: 10.1016/j.cma.2016.02.001.
Cited on pages 4, 30, 75.

[51] Kitware, Los Alamos National Laboratory. *Paraview.* Version 5.8.1. 2020.
Cited on page 42.

[52] O. Kunc and F. Fritzen. "Finite strain homogenization using a reduced basis and efficient sampling". In: *Mathematical and Computational Applications* 24.2 (2019), p. 56.
Cited on page 65.

[53] R. Langlois, M. Coret, and J. Réthoré. "Non-parametric stress field estimation for history-dependent materials: Application to ductile material exhibiting Piobert–Lüders localization bands". In: *Strain* (2022), e12410.
Cited on pages 78, 82.

[54] M. Latorre and F. J. Montáns. "What-you-prescribe-is-what-you-get orthotropic hyperelasticity". In: *Computational Mechanics* 53 (2014), pp. 1279–1298.
Cited on page 75.

[55] E. Le Mire. "Contributions expérimentales et théoriques à la fatigue multiaxiale des élastomères: Vers un critère cinématique". PhD thesis. École centrale de Nantes, 2022.
Cited on page 65.

[56] E. Le Mire, E. Verron, B. Huneau, and N. Selles. "Multiaxial fatigue experiments for elastomers based on true strain invariants". In: *Journal of Rubber Research* 24.2 (2021), pp. 227–236.
Cited on page 65.

[57] A. Leygue, M. Coret, J. Réthoré, L. Stainier, and E. Verron. "Data-based derivation of material response". In: *Computer Methods in Applied Mechanics and Engineering* 331 (2018), pp. 184–196. DOI: 10.1016/j.cma.2017.11.013.
Cited on pages 4, 30, 75, 82, 93, 131, 142.

[58] X. Li, G. Fang, J. Zhao, Z. Zhang, L. Sun, H. Wang, and X. Wu. "A practical and effective regularized polynomial smoothing (RPS) method for high-gradient strain field measurement in digital image correlation". In: *Optics and Lasers in Engineering* 121 (2019), pp. 215–226.
Cited on page 151.

[59] G. Lubineau. “A goal-oriented field measurement filtering technique for the identification of material model parameters”. In: *Computational mechanics* 44.5 (2009), pp. 591–603.
Cited on page 22.

[60] H. Luo, Y. Zhu, H. Zhao, L. Ma, and J. Zhang. “Simulation Analysis of Equibiaxial Tension Tests for Rubber-like Materials”. In: *Polymers* 15.17 (2023), p. 3561.
Cited on page 123.

[61] R. Mahnken. “Identification of material parameters for constitutive equations”. In: *Encyclopedia of computational mechanics* (2004).
Cited on page 16.

[62] MathWorks. *Matlab*. Version R2020b. 2020.
Cited on page 42.

[63] G. A. Maugin. “Continuum mechanics through the twentieth century”. In: *Springer, Berlin. doi* 10 (2013), pp. 978–94.
Cited on page 11.

[64] N. McCormick and J. Lord. “Digital image correlation”. In: *Materials today* 13.12 (2010), pp. 52–54.
Cited on page 22.

[65] S. K. Melly, L. Liu, Y. Liu, and J. Leng. “A review on material models for isotropic hyperelasticity”. In: *International Journal of Mechanical System Dynamics* 1.1 (2021), pp. 71–88.
Cited on page 14.

[66] K. P. Menard and N. Menard. “Dynamic Mechanical Analysis”. In: *Encyclopedia of Analytical Chemistry*. Ed. by R. A. Meyers. Chichester, UK: John Wiley & Sons, Ltd, 2017, pp. 1–25. DOI: 10.1002/9780470027318.a2007.pub3.
Cited on page 39.

[67] J. Mendes Ferrão. *Le voyage des plantes et les Grandes Découvertes*. Chandeigne, 2020.
Cited on page 11.

[68] L. Meunier, G. Chagnon, D. Favier, L. Orgéas, and P. Vacher. “Mechanical experimental characterisation and numerical modelling of an unfilled silicone rubber”. In: *Polymer testing* 27.6 (2008), pp. 765–777.
Cited on page 19.

[69] F. J. Montáns, F. Chinesta, R. Gómez-Bombarelli, and J. N. Kutz. “Data-driven modeling and learning in science and engineering”. In: *Comptes Rendus Mécanique* 347.11 (2019), pp. 845–855.
Cited on pages 30, 75.

[70] L. Mullins. “Softening of rubber by deformation”. In: *Rubber Chemestry and Technology* (1969), pp. 339–362.
Cited on pages 11, 39.

[71] R. W. Ogden. “Large deformation isotropic elasticity–on the correlation of theory and experiment for incompressible rubberlike solids”. In: *Proceedings of the Royal Society of London. A. Mathematical and Physical Sciences* 326.1567 (1972), pp. 565–584.
Cited on pages 14, 16, 49, 110.

[72] S. Pagano and M. Bonnet. *Constitutive equation gap*. 2012.
Cited on page 22.

[73] B. Pan. “Recent progress in digital image correlation”. In: *Experimental mechanics* 51 (2011), pp. 1223–1235.
Cited on page 22.

[74] B. Pan, H. Xie, Z. Wang, K. Qian, and Z. Wang. “Study on subset size selection in digital image correlation for speckle patterns”. In: *Optics express* 16.10 (2008), pp. 7037–7048.
Cited on page 22.

[75] A. R. Payne. “The dynamic properties of carbon black-loaded natural rubber vulcanizates. Part I”. In: *Journal of applied polymer science* 6.19 (1962), pp. 57–63.
Cited on pages 11, 39.

[76] W. Peters and W. Ranson. “Digital imaging techniques in experimental stress analysis”. In: *Optical engineering* 21.3 (1982), pp. 427–431.
Cited on page 21.

[77] J.-L. Piel-Desruisseaux. *L’outil de pierre préhistorique*. FeniXX, 1983.
Cited on page 11.

[78] F. Pierron and M. Grédiac. “Identification of the through-thickness moduli of thick composites from whole-field measurements using the Iosipescu fixture: theory and simulations”. In: *Composites Part A: Applied Science and Manufacturing* 31.4 (2000), pp. 309–318.
Cited on page 20.

[79] F. Pierron and M. Grédiac. “Towards Material Testing 2.0. A review of test design for identification of constitutive parameters from full-field measurements”. In: *Strain* 57.1 (2021), e12370.
Cited on page 21.

[80] A. Platzer. “Mécanique numérique en grandes transformations pilotée par les données: De la génération de données sur mesure à une stratégie adaptative de calcul multiéchelle”. PhD thesis. Ecole centrale de Nantes, 2020.
Cited on page 65.

[81] J. Réthoré, A. Leygue, M. Coret, L. Stainier, and E. Verron. “Computational measurements of stress fields from digital images”. In: *International Journal for Numerical Methods in Engineering* 113.12 (2018), pp. 1810–1826.
Cited on page 82.

[82] Réthoré, Julien. *Ufreckles*. Version 2.0. 2018.
Cited on pages 42, 52.

[83] P. L. Reu, E. Toussaint, E. Jones, H. A. Bruck, M. Iadicola, R. Balcaen, D. Z. Turner, T. Siebert, P. Lava, and M. Simonsen. “DIC challenge: developing images and guidelines for evaluating accuracy and resolution of 2D analyses”. In: *Experimental Mechanics* 58 (2018), pp. 1067–1099.
Cited on page 22.

[84] S. Roux and F. Hild. “Optimal procedure for the identification of constitutive parameters from experimentally measured displacement fields”. In: *International Journal of Solids and Structures* 184 (2020), pp. 14–23.
Cited on page 22.

[85] H. Schreier, J.-J. Orteu, M. A. Sutton, et al. *Image correlation for shape, motion and deformation measurements: Basic concepts, theory and applications*. Vol. 1. Springer, 2009.
Cited on page 22.

[86] M. A. Sutton, W. Wolters, W. Peters, W. Ranson, and S. McNeill. "Determination of displacements using an improved digital correlation method". In: *Image and vision computing* 1.3 (1983), pp. 133–139.
Cited on pages 20, 21.

[87] Symetrie. *Symétrie website*. URL: `https://symetrie.fr/hexapodes-fr/logiciel/simulateur-hexasym/`.
Cited on page 32.

[88] K. P. Tarnavsky Eitan, Alex Smolyansky, Eddie. *Connected Papers*.
Cited on page 15.

[89] A. Tayeb, N. Di Cesare, Y. Lu, L. Sales, G. Bastos, and J.-B. Le Cam. "Identifying simultaneously hyper-viscoelastic parameters from a unique heterogenous relaxation test: application to engineering elastomeric materials". In: *Meccanica* (2023), pp. 1–20.
Cited on page 24.

[90] L. R. Treloar. "Stress-strain data for vulcanized rubber under various types of deformation". In: *Rubber Chemistry and Technology* 17.4 (1944), pp. 813–825.
Cited on pages 17, 49, 67, 68, 107, 140.

[91] L. R. Treloar. "Stress-strain data for vulcanized rubber under various types of deformation". In: *Rubber Chemistry and Technology* 17.4 (1944), pp. 813–825.
Cited on pages 19, 85.

[92] G. Valdés Alonzo. "Identification of material properties and phase distribution of heterogeneous materials through data-driven computational methods: towards an enhanced constitutive space". In: (2022).
Cited on page 82.

[93] G. Valdés-Alonzo, C. Binetruy, B. Eck, A. García-González, and A. Leygue. "Phase distribution and properties identification of heterogeneous materials: A data-driven approach". In: *Computer Methods in Applied Mechanics and Engineering* 390 (2022), p. 114354.
Cited on pages 78, 82.

[94] E. Verron. "Modèles hyperélastiques pour le comportement mécanique des élastomères". In: *Techniques de l'Ingénieur* AM 8 210 (2018).
Cited on page 16.

[95] A. Vinel. "Characterization of the thermomechanical behaviour of metals for high strain-rates, using ultra-high speed imaging cameras". PhD thesis. Ecole Centrale de Nantes, 2022.
Cited on page 82.

[96] J. Wang, T. Li, F. Cui, C.-Y. Hui, J. Yeo, and A. T. Zehnder. "Metamodeling of constitutive model using Gaussian process machine learning". In: *Journal of the Mechanics and Physics of Solids* 154 (2021), p. 104532.
Cited on page 75.

[97] S. Wiesheier, J. Mergheim, and P. Steinmann. "Discrete data-adaptive approximation of hyperelastic energy functions". In: *Computer Methods in Applied Mechanics and Engineering* 416 (2023), p. 116366.
Cited on pages 22, 75.

[98] Y. Wu, H. Wang, and A. Li. "Parameter identification methods for hyperelastic and hyper-viscoelastic models". In: *Applied Sciences* 6.12 (2016), p. 386.
Cited on page 16.

[99] Y. Xiang, D. Zhong, S. Rudykh, H. Zhou, S. Qu, and W. Yang. “A review of physically based and thermodynamically based constitutive models for soft materials”. In: *Journal of Applied Mechanics* 87.11 (2020), p. 110801.
Cited on page 14.

[100] H. Xiao and L.-S. Chen. “Hencky’s logarithmic strain and dual stress–strain and strain–stress relations in isotropic finite hyperelasticity”. In: *International journal of solids and structures* 40.6 (2003), pp. 1455–1463.
Cited on page 62.

[101] C. Yao, X. Ma, R. Ma, D. Zhao, and J. Zhao. “Data-driven optical method for full-field stress measurements”. In: *Optics Letters* 48.11 (2023), pp. 3091–3094.
Cited on page 78.

[102] O. Yeoh. “Hyperelastic material models for finite element analysis of rubber”. In: *Journal of Natural Rubber Research* 12.1997 (1997), pp. 142–153.
Cited on pages 16, 42, 111, 120.

[103] S. Zschocke, W. Graf, and M. Kaliske. “Incorporating uncertainty in stress-strain data acquisition: extended model-free data-driven identification”. In: *PAMM* (2023), e202300008.
Cited on page 79.

Titre : Identification de modèles pilotée par les données appliquée à l'hyperélasticité : acquisition et représentation de la densité d'énergie de déformation au cours d'essais multiaxiaux.

Mots clés : Identification, piloté par mes données, densité d'énergie de déformation, multiaxial.

Résumé : Modéliser la réponse mécanique des matériaux consiste à établir une relation (un modèle) entre contraintes et déformations, dépendant de paramètres identifiés à partir de données expérimentales issues d'essais mécaniques. D'une part, l'identification basée sur des essais homogènes n'apporte pas d'information sur la réponse du matériau soumis à des sollicitations complexes. D'autre part, l'identification basée sur des essais multiaxiaux est plus coûteuse numériquement et impose le choix du modèle a priori. Récemment, a émergé la possibilité de représenter le comportement mécanique des matériaux par une base de données plutôt que via une loi de comportement au travers de la « Data Driven Computational Mechanics ». Dans ce cadre, l'algorithme Data-Driven Identification (DDI) développé par Leygue *et al*. (2018) permet d'estimer le champ de contrainte lors d'un essai multiaxial.
Cette thèse propose d'explorer la réponse cinématique puis mécanique complète de membranes élastomères sollicitées en grandes déformations multiaxiales grâce à un montage expérimental original mettant en jeu un hexapode. La méthode DDI est ensuite utilisée pour déterminer la réponse en contraintes du matériau lors de ces essais. Deux développements sont finalement proposés : une méthode d'identification alliant DDI (sans modèle) et modèles de comportement, et une proposition d'amélioration des géométries d'éprouvettes pour les essais multiaxiaux.

Title : Data-Driven Model Identification for hyperelasticity: mapping the strain energy throughout multiaxial experiments.

Keywords : Identification, Data-Driven, strain energy density, multiaxial.

Abstract : Modeling the mechanical response of materials involves the derivation of a relationship (a model) between stresses and strains, depending on parameters. These parameters are identified from experimental data obtained from mechanical tests. On the one hand, identification based on simple tests (uniaxial tension, for example) provides no information on the response of materials subjected to complex loading conditions. On the other hand, identification based on multiaxial tests is more costly numerically and requires the model to be chosen at the outset of the procedure.
Recently, the possibility of representing the mechanical behaviour of materials by a database rather than via a behaviour law has emerged through "Data-Driven Computational Mechanics". On this basis, the Data-Driven Identification (DDI) algorithm developed by Leygue et al. (Computer Methods in Applied Mechanics and Engineering, 331, 184-196 (2018)) can be used to estimate the stress field during a multiaxial test. The present thesis explores the complete kinematic and mechanical response of elastomer membranes subjected to multiaxial large strain, using an original experimental set-up involving a hexapod. The DDI method is then used to determine the stress response of the material during these multiaxial tests. Two developments are finally presented: an identification method combining DDI (model-free) and standard constitutive models, and a proposal for improving sample geometries for multiaxial tests.